Analysis of a Frequency Converter Equipped with Diode Rectifier and Small DC Link Capacitor

AALBORG UNIVERSITET

Institute of Energy Technology

Master Thesis

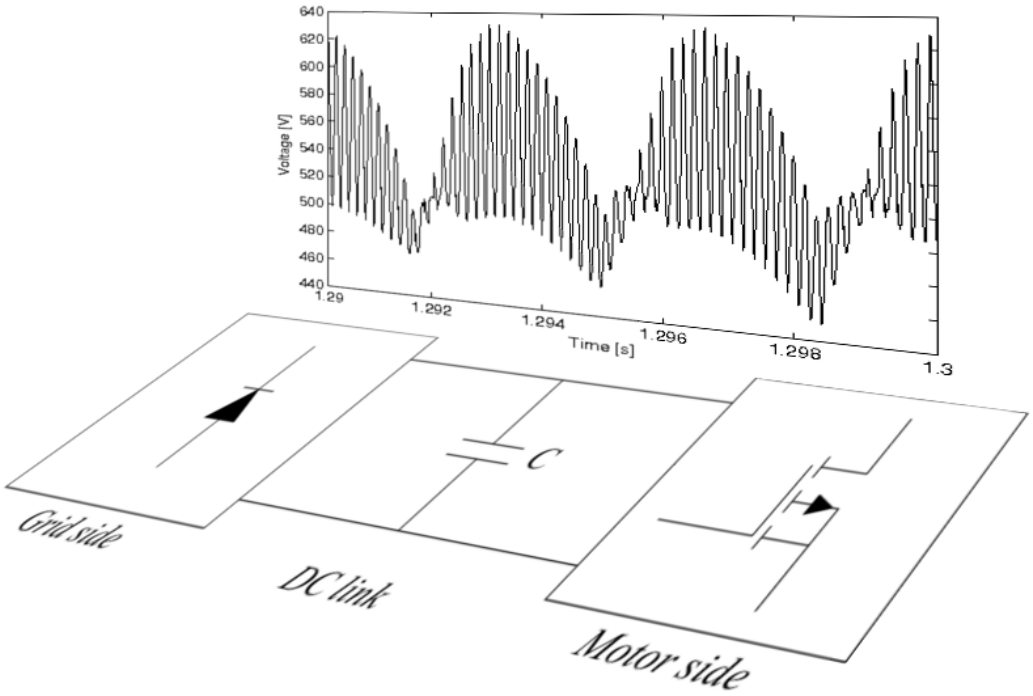

Conducted by Thordur Ofeigsson, spring 2008

AALBORG UNIVERSITET

Institute of Energy Technology
Pontoppidanstræde 101
Telephone 96 35 92 40
Fax 98 15 14 11
http://www.iet.aau.dk

Title:

Analysis of a frequency converter equipped with diode rectifier and small DC link capacitor

Project period:
4. February - 4. June 2008

Project group number:
PED10-1015a

Conducted by:
Thordur Ofeigsson

Supervisor:
Stig Munk-Nielsen

Number of copies: 6

Number of pages: 69

Finished: 4. June 2008

Abstract:

This project is focused on a low cost frequency converter equipped with diode rectifier and small DC link capacitor. The problems associated with this configuration are the high fluctuations introduced in the DC link voltage. Due to the small capacitor the diode rectifier harmonics are not rejected as the natural frequency of the DC link is above six times the grid side frequency. When this type of frequency converter is used to drive a squirrel cage induction motor the system is very sensitive to changes in speed. Quick changes in speed cause large overvoltages in the DC link voltage which in turn could trigger the overvoltage protection of the frequency converter. Therefore the dynamics of the system are very poor.
The projects main goal is to analyse stability margins of the frequency converter and examine the influence of different parameters on the stability of the system. In order to analyse stability a mathematical model of the system has to be obtained. The model is then linearized to derive transfer functions that describe the influence of different inputs on the DC link voltage. The stability analysis can then be carried out using conventional control theory. The obtained stability margins are then evaluated with simulations in Matlab/Simulink.
To fit with the topic of a low cost drive, a sensorless V/f control strategy is also designed and verified with simulations. The open loop V/f control and space vector modulation are then implemented on a DSP to examine the system behavior in practice. Experimental results were acquired and documented.

Preface

This project report entitled *Analysis of a frequency converter equipped with diode rectifier and small DC link capacitor* is documented by group PED10-1015a on 10^{th} semester at Institute of Energy Technology, Aalborg University.

Literature references are mentioned in square brackets by numbers which have their corresponding equivalent in the Bibliography with more detailed information about the literature. Appendices are assigned with letters and are arranged in alphabetical order in the back of the report. Equations are numbered in format *(X.Y)* and figures are numbered in format *fig. X.Y*, where X is the chapter number and Y is the number of the item. The contents of the enclosed CD-ROM are explained in appendix D.

The author would like to thank Stig Munk-Nielsen for his supervision on the project and also the people at Danfoss, Radu Dan Lazar and Johnny Wahl Jensen, for their help and hardware support.

The report is conducted by:

Thordur Ofeigsson

Contents

Chapter 1

Introduction

This chapter gives description of the project and provides some relevant background information. Project goals and limitations are outlined as well.

1.1 Background

The frequency converter used within this project is shown in fig. 1.1. It is equipped with a diode rectifier on the grid side, DC link capacitor and an inverter on the motor side. Many other varieties of the frequency converter exist but the focus is kept on the previously mentioned arrangement where it is the arrangement involved in this project.

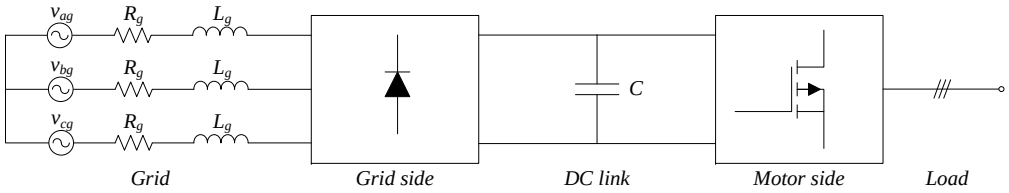

Figure 1.1: *Frequency converter.*

Rectifier-inverter topology

To begin with, the circuit in fig. 1.1 will be studied with no inductance involved, $L_g = 0$. If the motor side inverter is neglected, the DC link voltage is rather constant for large capacitance where the capacitor filters the diode rectifier harmonics effectively. Therefore, almost no current will flow through the capacitor due to the relationship:

$$i_C = C\frac{dv_C}{dt} \tag{1.1}$$

where i_C is the current through the capacitor, C is the capacitance and v_C is the voltage over the capacitor.

But if the capacitance is lowered, fluctuations in the DC link voltage, with 6 times the grid side frequency, increase. This is because the natural frequency of the DC link is increased and does therefore not reject the rectifier harmonics as effectively. This can also be viewed from energy laws, where the energy injected through the diode rectifier is still the same. This can be seen from the following relationship:

$$W_C(t) = \int_{t_0}^{t_1} p(t)dt = \frac{C}{2}\left(v_C^2(t_1) - v_C^2(t_0)\right) \tag{1.2}$$

where $W_C(t)$ is the total energy injected to the capacitor and $p(t)$ is the instant power through the capacitor. Fig. 1.2 shows $v_C(t)$ as the capacitor charges or discharges, it is shown that $W_C(t)$ is the area under the voltage curve as the capacitor is being charged.

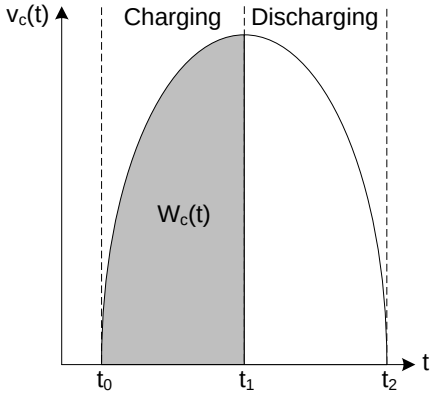

Figure 1.2: *Voltage over the capacitor when it charges and dishcarges.*

As C is lowered the difference between the maximum and minimum value of v_C has to increase if the same energy is injected to the capacitor. And as the voltage fluctuations increase, the current through the capacitor increases in order to fulfill (1.1).

But this arrangement introduces some problems with inrush currents and overvoltages at the instance of grid connection. For a worst case situation when the DC link capacitor is fully discharged and the grid side voltage is at its peak value the maximum theoretical voltage over the DC link capacitor would be $2\sqrt{2}V_{LL}$, V_{LL} being the line-to-line grid voltage, which could possibly destroy the capacitor. Together with the overvoltage, a large inrush current would also occur. With no inductance involved the inrush current would rise very quickly to a high value. The inrush current could possibly destroy the diodes, the DC link capacitor or the load, [1].

Effects of inductance

In practice, a grid inductance L_g is always present on the grid side, as shown in fig. 1.3. The size of L_g can vary depending on whether the grid is stiff or weak.

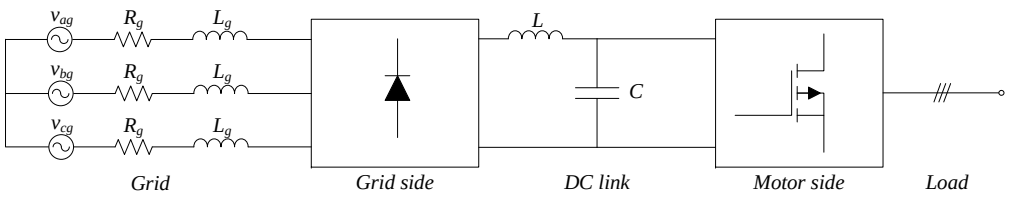

Figure 1.3: *Frequency converter with DC choke.*

Normally the DC link capacitor is large to provide a stable DC voltage, a small L_g then introduces a very high harmonic distortion and a low power factor. An optional inductance can be added, either as a DC choke or an AC choke, depending if the optional inductance is located on

the DC or the AC side of the diode rectifier. The total inductance can then be increased which will decrease the harmonic distortion and give larger power factor, [2].

Three phase inverter

The motor side converter is a three phase inverter, as shown in fig. 1.4.

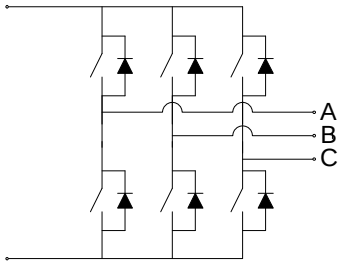

Figure 1.4: *Three phase inverter.*

The three phase inverter consists of six switches parallely connected to diodes, to provide a return path for the load current. The inverter utilizes the DC link voltage to the load in a controlled fashion using pulse width modulated gate signals. The preferred pulse width modulation methods are the carrier-based methods because they provide low harmonic distortion and well defined harmonic spectrum. The carrier-based methods can mainly be implemented in two ways, using the triangle intersection technique or the direct digital technique. The former technique compares a sinusoidal control signal to a high frequency triangular wave to create the gate singals. The latter technique constructs the gate signals by precalculating the required time duration of each gate signal pulse using space vector theory. Many methods exist for producing pulse width modulated gate signals, the difference for carrier-based methods lies in the decision of the zero sequence signal for the triangle intersection technique and in partioning of the zero states in the direct digital technique, [3].

In practice, the switches do not switch states instantly, therefore the inverter is usually equipped with deadtime that delays the turn-on and turn-off of every switch to prevent a short-circuit through each inverter leg. The deadtime has several negative effects on the output voltage, like reducing the fundamental component and adding lower order harmonics, [4].

As the progress continues in power semiconductor devices, higher power ratings and switching frequencies become available for inverters. Many switching devices exist and the choice depends mainly on current and voltage ratings and switching frequency. But other characteristics are also important, these are [1]:

- Small leakage current.
- Small on-state resistance.
- Small on-state voltage.
- Short turn-on and turn-off times.
- Large forward- and reverse-voltage blocking.
- High on-state current rating.
- Positive temperature coefficient of on-state resistance.

- Gate drive complexity.
- Tolerance of rated voltage and current during switching.
- Large dv/dt and di/dt ratings.

DC link capacitor

Because of its high capacitance per volume ratio, the electrolytic capacitor has been the preferred capacitor for the DC link for years, where high capacitance gives smoother DC link voltage. But the electrolytic capacitor is expensive and heavy, and introduces considerable explosive risks and is usually the component that fails in the frequency converter, reducing the lifetime of the system, [5] [6]. Therefore researchers have been looking for a replacement for the electrolytic capacitor. But replacing the electrolytic capacitor would result in a DC link with lower capacitance which does not provide as effective filtering of the rectifier harmonics. But, lower capacitance would also allow higher AC current to travel through the capacitor, reducing the line current harmonics, but also increasing the stress on the capacitor and increasing the risk of capacitor breakdown. Due to these reasons, the most promising substitude has been the metallized polypropylene film (MPPF) capacitor. Because of its very low losses, it permits a relatively higher AC current compared to other capacitor types, decreasing the risk of breakdown, [7]. Also, the MPPF capacitor is lightweight, with much longer lifetime and no explosion risk compared to the electrolytic capacitor, [5] [7] [8] [9].

On the downside, the MPPF capacitor has much lower capacitance per volume ratio, the capacitance being about 1% of the electrolytic capacitor for the same volume [6]. With lower DC link capacitance voltage fluctuations are increased. In normal induction motor drives, the motor control attempts to keep the average power constant at constant speed, but with large voltage fluctuations the motor control causes the stator current to fluctuate. This can cause the drive to become unstable [10].

1.2 Problem description

The project proposal was given by Danfoss and deals with frequency converter consisting of a diode rectifier on the grid side, small DC link capacitor and full bridge inverter on the motor side. As the system layout shows in fig. 1.5 there is no DC choke present. Furthermore, there is no speed measurement from the squirrel cage induction motor (SCIM) which consequently requires a sensorless motor control. The SCIM is loaded with a DC motor which gives the ability to test the control strategy for different loads. The controller will interact with the motor side inverter using feedback of measured currents and voltages from DC link and stator to calculate the duty cycles for the inverter.

The problem arises from the small DC link capacitor which causes large variations in the DC link voltage. The system has to be linearized to find stability margins in order to build a controller to compensate for the undesired voltage fluctuations. But as project period is limited the main project goal will be to come up with a linearized model of the frequency converter and analyse stability margins for different parameters.

This problem is treated in several papers for different types of frequency converters. [5] uses simplified model of the diode rectifier for the controller design and states that no additional choke over the mains inductance is necessary if the natural frequency of the DC link is chosen to be considerably higher than six times the mains frequency but lower than the switching frequency. [6] introduces new modulation method to deal with the heavily fluctuating DC link voltage. [7]

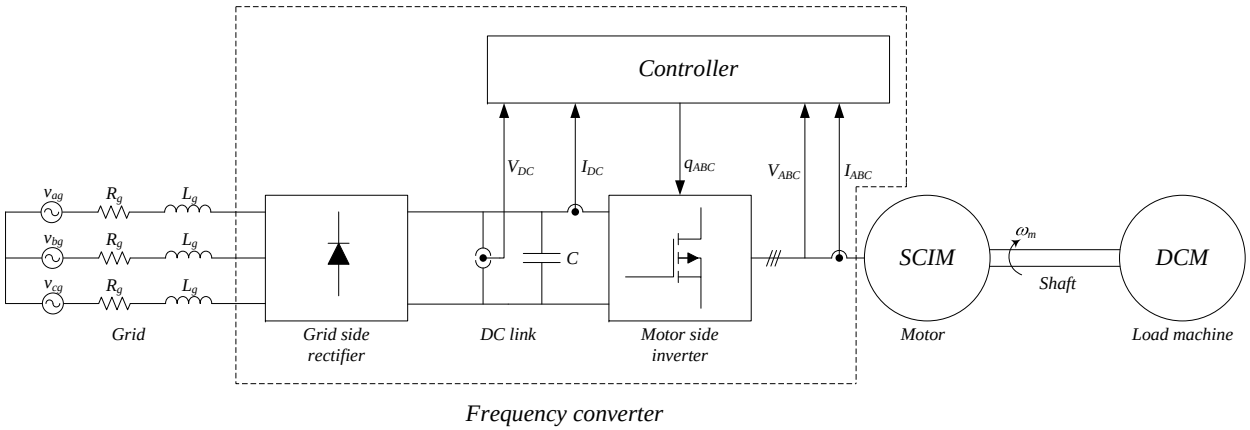

Figure 1.5: *System layout.*

investigates frequency converter with small DC link feeding a synchronous permanent magnet motor. [8] works with overmodulation method for frequency converters where small DC link tends to draw the inverter into overmodulation. [9] deals with a small DC link frequency converter with a single phase grid side. [10] stabilizes the drive using a resonant filter.

1.3 Project goals

Project goals are inspired by project proposal from Danfoss. The main goal of this project is to analyse stability in the frequency converter and see how different parameters effect the stability of the system. The complete list of goals is as follows:

- Modeling of nonlinear system.
- Design of sensorless motor control strategy.
- Construction of a linearized model of the frequency converter.
- Locate stability margins.
- Verify stability margins with nonlinear model.
- Implement motor control strategy on a DSP.

1.4 Limitations

- Saturation effects in motor are not considered.
- Grid side parameters are only considered within narrow range.
- Instability in the SCIM is not considered.
- Effects caused by deadtime are not considered in stability analysis.

Chapter 2

Models and sensorless V/f control

Relevant models to simulate the frequency converter and squirrel cage induction motor are derived in this chapter. Then a sensorless V/f control is designed and evaluated with simulations.

2.1 Space Vector Modulation

The inverter is controlled with pulsating signals which are modulated using pulse width modulation methods. Many methods exist but within the carrier-based methods they differ mainly in implementation, linear range, waveform quality and switching losses. The chosen modulation method is the space vector modulation, where it is possibly the most popular method because of its simplicity and great linear range, [3].

Model of the modulator

Normally the space vector modulation is implemented using space vectors, [11] [12]. But the implementation used in this project is based on [3] and does not require space vector theory. Instead it uses the fact that space vector modulation moves the reference voltages to the middle of the triangular carrier wave. Centralizing the reference voltages in this way gives the duty cycles for the space vector modulation.

The reference voltages have to be normalized with half the DC link voltage.

$$v_{x_{norm}} = v_{x_{ref}} \cdot \frac{2}{v_{dc}} \qquad x = \{a, b, c\} \tag{2.1}$$

Then the smallest $v_{x_{norm}}$ in magnitude of the three phases is added to all the normalized reference voltages. This gives the duty cycles for space vector modulation.

$$D_x = v_{x_{norm}} \cdot \frac{v_{min}}{2} \tag{2.2}$$

where v_{min} is defined as:

$$v_{min} \leq |v_{x_{norm}}| \tag{2.3}$$

Fig. 2.1 shows the normalized reference voltages together with the triangular carrier wave. The triangular carrier wave having values between 1 and -1, it can be seen that the distances from the top reference voltage to 1 is not the same as the distance from the bottom reference voltage to -1, this describes the case where the reference voltages are not centralized. Now the waveforms are moved, using (2.2), so they become centralized within the triangular carrier wave as fig. 2.2 depicts.

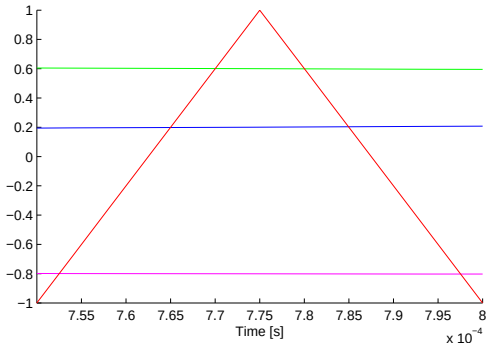

Figure 2.1: *Uncentralized reference voltages.*

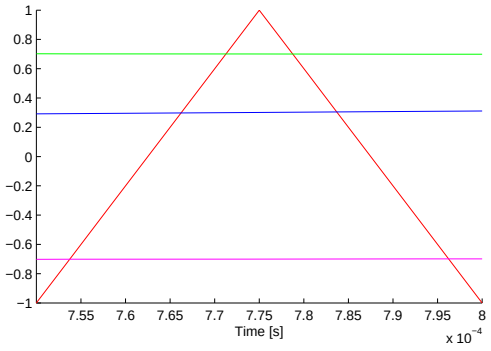

Figure 2.2: *Centralized reference voltages.*

Looking at the centralized waveforms from a larger timeframe, the duty cycles for the space vector modulation method are revealed as shown in fig. 2.3.

The model for the modulator was implemented in Matlab/Simulink using S-function builder. The code can be found in appendix A.

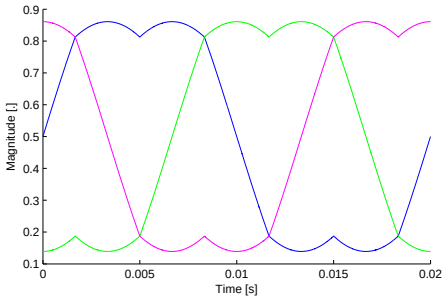

Figure 2.3: *Duty cycles of space vector modulation.*

2.2 Time delay

Time delays are undesired in control systems where they always reduce the stability of the system. But time delays always occur for example in sensing, sampling and in the control process itself. Due to the increased instability caused by time delays, they are necessary to take into account in the system model, [13].

Model of time delay

The exact model of time delay is an exponential function, $e^{T_d s}$, where T_d is the time delay. This can not be used to derive the root-locus diagram where it is not a rational function.

But it is possible to replace the exponential function with a rational function using the Padé approximant of $e^{T_d s}$. The accuracy of the Padé approximant depends on the order of the rational function and is denoted by p and q, a (p,q) Padé approximant being a rational function containing p-th order polynomial in the numerator and q-th order polynomical in the denumerator. In [13], two Padé approximants of $e^{T_d s}$ are presented, (1,1) Padé approximant shown in (2.4) and (2,2)

Padé approximant shown in (2.5).

$$e^{T_d s} \cong \frac{1 - (T_d s/2)}{1 + (T_d s/2)} \tag{2.4}$$

$$e^{T_d s} \cong \frac{1 - (T_d s/2) + (T_d s)^2/12}{1 + (T_d s/2) + (T_d s)^2/12} \tag{2.5}$$

The Padé approximant corresponding to (2.5) is chosen for modeling the time delay where it is more accurate with little increased complexity.

Block diagram of the model is shown in fig. 2.4.

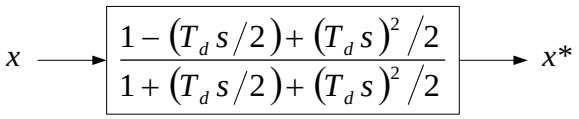

Figure 2.4: *Block diagram of sample delay.*

According to the project description there is a 2 samples delay within the system for a sampling frequency of $f_s = 4\ kHz$. The sampling delay is therefore:

$$T_d = 5 \cdot 10^{-4}\ sec. \tag{2.6}$$

2.3 Voltage source inverter

A model of the voltage source inverter (VSI) is necessary to transform the DC link voltage to the phase voltages applied to the load for given duty cycles.

Average model

Circuit diagram of the VSI is shown in fig. 2.5, its outputs are connected to the stator windings of the motor. The stator windings are star-connected with the neutral point denoted as n. The negative DC bus is denoted by 0 and the outputs of each leg of the inverter are denoted by a, b and c.

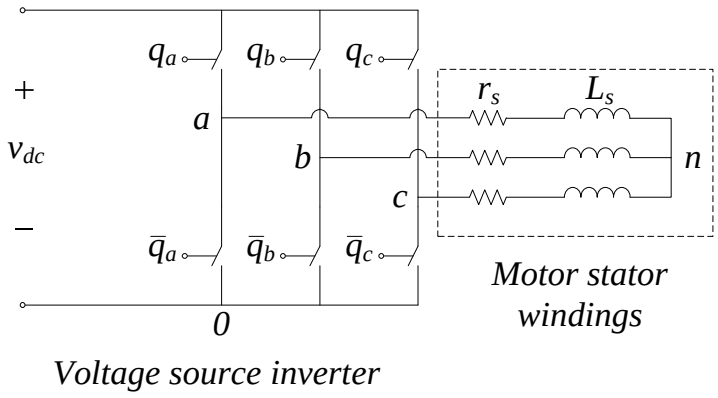

Figure 2.5: *Circuit diagram of VSI conneted to stator windings.*

From fig. 2.5 it is apparant that in a switching operation, v_{a0}, v_{b0} and v_{c0} are either v_{dc} or 0:

$$v_{x0} = q_x \cdot v_{dc} \qquad x = \{a, b, c\} \tag{2.7}$$

where q_x is the switching state of the leg, $q_x = 1$ meaning that the upper switch is conductiong while the lower is blocking and $q_x = 0$ meaning the opposite.

For an average model the switching states are replaced with the duty cycles d_x of each leg:

$$v_{x0} = d_x \cdot v_{dc} \qquad x = \{a, b, c\} \tag{2.8}$$

Then each phase voltage can be described by:

$$v_{xn} = v_{x0} - v_{n0} \qquad x = \{a, b, c\} \tag{2.9}$$

where v_{n0} is [1]:

$$v_{n0} = \frac{v_{a0} + v_{b0} + v_{c0}}{3} \tag{2.10}$$

Putting (2.8) and (2.10) in (2.9) gives the average model of the VSI:

$$\begin{aligned} v_{an} &= (2d_a - d_b - d_c)\frac{v_{dc}}{3} \\ v_{bn} &= (2d_b - d_a - d_c)\frac{v_{dc}}{3} \\ v_{cn} &= (2d_c - d_b - d_a)\frac{v_{dc}}{3} \end{aligned} \tag{2.11}$$

The DC link current can be derived using Kirchoffs current law. The DC link current is the total current from all branches:

$$i_{dc} = d_a i_a + d_b i_b + d_c i_c \tag{2.12}$$

To fit with the motor model the phase voltages have to be transformed to the stationary reference frame using (2.13).

$$\begin{aligned} v_\alpha &= \frac{2}{3}\left(v_{an} - \frac{1}{2}v_{bn} - \frac{1}{2}v_{cn}\right) \\ v_\beta &= \frac{2}{3}\frac{\sqrt{3}}{2}\left(v_{bn} - v_{cn}\right) \end{aligned} \tag{2.13}$$

Block diagram of the VSI model is shown in fig. 2.6.

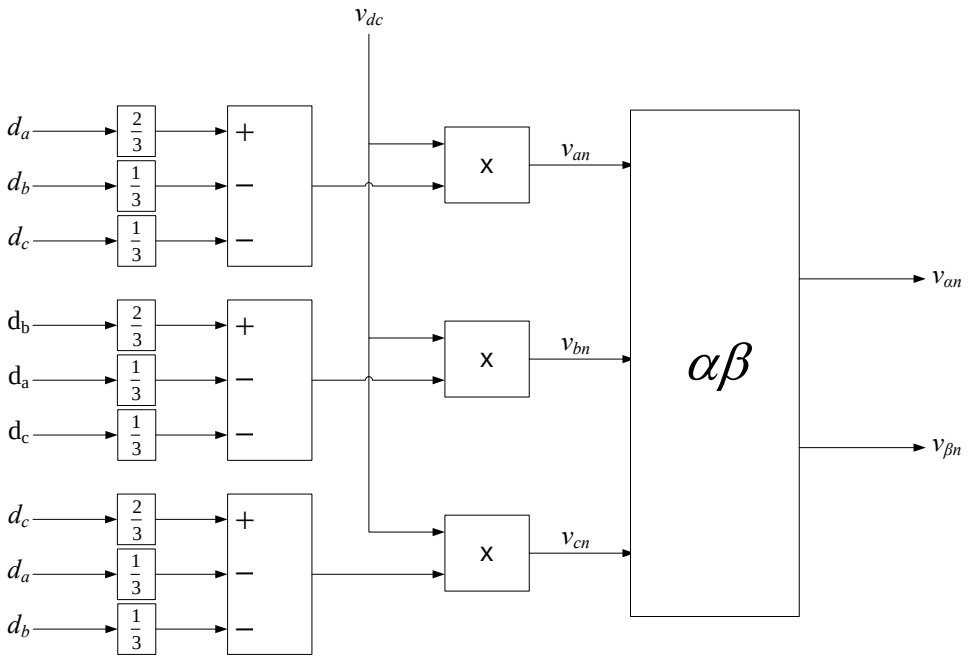

Figure 2.6: *Block diagram of VSI.*

2.4 Induction motor

A model of the squirrel cage induction motor (SCIM) is necessary to see the influence of different inverter output voltages on the motor for different load torques. The selected model of the IM is the Γ model where it is well suited for analysis of drives using the V/f control strategy [14].

IM equations in dq0 reference frame

Equations that describe the dynamic behavior of the IM are shown in (2.14) and (2.15), [15].

$$\vec{v}_{abcs} = r_s\vec{i}_{abcs} + L_s p\vec{i}_{abcs} + \gamma L'_m p(\frac{\vec{i'}_{abcr}e^{j\theta_r}}{\gamma}) \tag{2.14}$$

$$\gamma\vec{v'}_{abcr} = \gamma^2 r'_r\frac{\vec{i'}_{abcr}}{\gamma} + \gamma^2 L'_r p\frac{\vec{i'}_{abcr}}{\gamma} + \gamma L'_m p(\vec{i}_{abcs}e^{-j\theta_r}) \tag{2.15}$$

where $L_s = L_{ls} + L'_m$ and $L'_r = L'_{lr} + L'_m$. L_{ls} and L'_{lr} being the leakage inductances of the stator and rotor, respectively, and L'_m the mutual inductance between stator and rotor windings.

The parameter γ is the turns-ratio between the stator and rotor. It arises from the transformer action of the IM and can be chosen completely arbitarily for a squirrel cage IM, [15]. But it will remain undefined for now. (2.14) and (2.15) can be simplified by using the notation:

$$\vec{v}_{abcr} = \gamma\vec{v'}_{abcr} \tag{2.16}$$

$$\vec{i}_{abcr} = \frac{\vec{i'}_{abcr}}{\gamma} \tag{2.17}$$

$$L_m = \gamma L'_m \tag{2.18}$$

$$L_r = \gamma^2 L'_r \tag{2.19}$$

$$r_r = \gamma^2 r'_r \tag{2.20}$$

The problem using (2.14) and (2.15) for modeling is that they contain position dependent mutual inductances L_m. If the motor is rotating, these inductances become time-varying, resulting in nonlinear relationships. By transforming both the stator and rotor variables of (2.14) and (2.15) to another reference frame, the time-varying inductances can be eliminated [16].

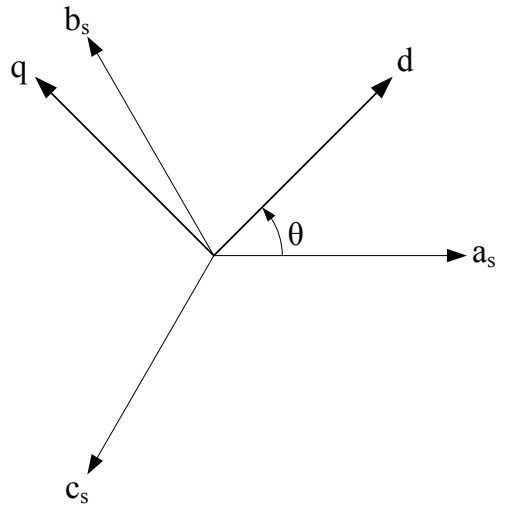

Figure 2.7: *The dq reference frame relative to the stator abc reference frame.*

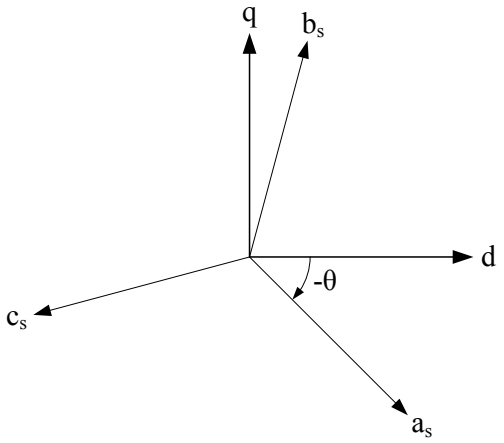

Figure 2.8: *The stator abc reference frame relative to the dq reference frame.*

Fig. 2.7 shows how rotating dq0 reference frame is located relatively to the magnetic axes of the stator phases. Someone standing on the stator a-axis would see the d-axis rotating with angle θ, alternatively if someone would stand on the d-axis he would see the stator a-axis rotate with angle $-\theta$ as shown in fig. 2.8. It follows then:

$$\vec{f}_{dq0} = \vec{f}_{abcs} e^{-j\theta} \tag{2.21}$$

where f can be any of the stator circuit variables.

Knowing that $e^{-j\theta} = cos\theta - jsin\theta$, the generalized $dq0$ transformation matrix can now be derived:

$$\begin{bmatrix} f_d \\ f_q \\ f_0 \end{bmatrix} = \frac{2}{3} \begin{bmatrix} cos(\theta) & cos\left(\theta - \frac{2\pi}{3}\right) & cos\left(\theta + \frac{2\pi}{3}\right) \\ -sin(\theta) & -sin\left(\theta - \frac{2\pi}{3}\right) & -sin\left(\theta + \frac{2\pi}{3}\right) \\ \frac{1}{2} & \frac{1}{2} & \frac{1}{2} \end{bmatrix} \begin{bmatrix} f_a \\ f_b \\ f_c \end{bmatrix} \tag{2.22}$$

where f_0 is the zero-sequence component and is necessary to obtain a unique transformation.

Putting (2.14) into (2.21) results in [15]:

$$\vec{v}_{dqs} = r_s \vec{i}_{dqs} + L_s p\vec{i}_{dqs} + L'_m p\vec{i}_{dqr} + j\omega(L_s i_{dqs} + L_m i_{dqr}) \tag{2.23}$$

where ω is the speed of the $dq0$ reference frame.

Now, for the rotor variables, fig. 2.9 shows how rotating dq0 reference frame is located relatively to the magnetic axes of the rotor phases. Similiar analysis as before give:

$$\vec{f}_{dq0} = \vec{f}_{abcr} e^{-j(\theta - \theta_r)} \tag{2.24}$$

Putting (2.15) into (2.24) gives:

$$\vec{v}_{dqr} = r_r \vec{i}_{dqr} + L_r p\vec{i}_{dqr} + L_m p\vec{i}_{dqs} + j(\omega - \omega_r)(L_r \vec{i}_{dqr} + L_m \vec{i}_{dqs}) \tag{2.25}$$

(2.23) and (2.25) are the general $dq0$ reference frame representation of the IM model. The speed of the reference frame can be chosen by specifing the variable ω.

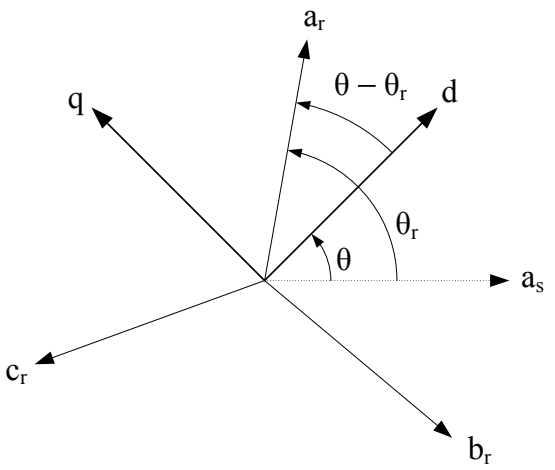

Figure 2.9: *The dq reference frame relative to the rotor abc reference frame.*

Γ model

In (2.14) and (2.15) the turns-ratio parameter γ was left undefined. The most common definition of γ is the real turns-ratio:

$$\gamma = \frac{N_s}{N_r} \tag{2.26}$$

where N_s is the number of windings on the stator and N_r is the number of windings on the rotor.

This results in real leakage inductance model based on the datasheet from the designer, [15]. The equivalent circuit representation for this arrangement can be seen in fig. 2.10.

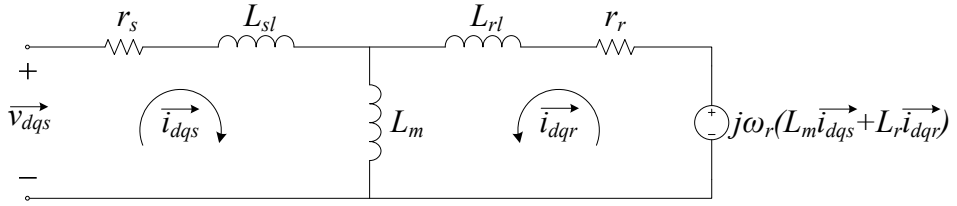

Figure 2.10: *T-model of equivalent circuit.*

But defining γ as:

$$\gamma = \frac{L_s}{L'_m} \tag{2.27}$$

puts all the leakage inductance on the rotor and is convenient for drives using the V/f control, [14]. It is therefore used for the IM model.

The new parameters of the motor can be calculated using (2.20) and (2.27).

$$L_m = L_s \tag{2.28}$$
$$L_r = \gamma^2 L'_{lr} + \gamma L_{ls} + L_s \tag{2.29}$$
$$r_r = \gamma^2 r'_r \tag{2.30}$$

The IM model then looks like:

$$\vec{v}_{dqs} = r_s\vec{i}_{dqs} + L_s p\vec{i}_{dqs} + L_s p\vec{i}_{dqr} + j\omega L_s(\vec{i}_{dqs} + \vec{i}_{dqr}) \tag{2.31}$$

$$\vec{v}_{dqr} = r_r\vec{i}_{dqr} + L_r p\vec{i}_{dqr} + L_s p\vec{i}_{dqs} + j(\omega - \omega_r)(L_r\vec{i}_{dqr} + L_s\vec{i}_{dqs}) \tag{2.32}$$

This changes the equivalent circuits representation as seen in fig. 2.11. To fit with the equations, another inductance, $L_L = \gamma^2 L'_{lr} + \gamma L_{ls}$, is defined as the rotor inductance.

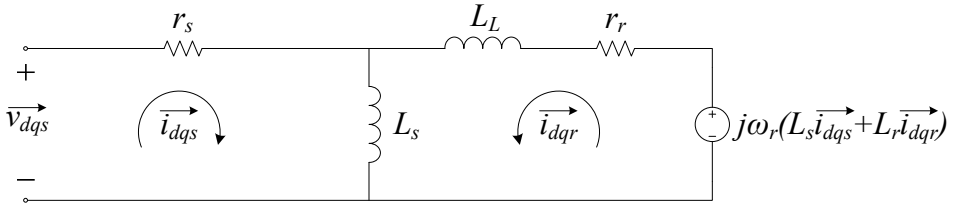

Figure 2.11: Γ*-model of equivalent circuit.*

Constructing the model

To build the model in Matlab/Simulink (2.31) and (2.32) have to be split to their d and q components and put in the s-domain.

$$v_{ds} = r_s i_{ds} + L_s s i_{ds} + L_s s i_{dr} - \omega L_s(i_{qs} + i_{qr}) \tag{2.33}$$
$$v_{qs} = r_s i_{qs} + L_s s i_{qs} + L_s s i_{qr} + \omega L_s(i_{ds} + i_{dr}) \tag{2.34}$$
$$v_{dr} = r_r i_{dr} + L_r s i_{dr} + L_s s i_{ds} - (\omega - \omega_r)(L_r i_{qr} + L_s i_{qs}) \tag{2.35}$$
$$v_{qr} = r_r i_{qr} + L_r s i_{qr} + L_s s i_{qs} + (\omega - \omega_r)(L_r i_{dr} + L_s i_{ds}) \tag{2.36}$$

The model is build using the stationary reference frame, therefore $\omega = 0$. The stator currents are derived by isolating i_{ds} in (2.33) and i_{qs} in (2.34):

$$i_{ds} = \frac{1}{sL_s + r_s}(v_{ds} - sL_s i_{dr}) \tag{2.37}$$
$$i_{qs} = \frac{1}{sL_s + r_s}(v_{qs} - sL_s i_{qr}) \tag{2.38}$$

Block diagram of the model for obtaining stator currents is show in fig. 2.12.

The rotor currents can be derived from (2.35) and (2.36) by isolating i_{dr} and i_{qr} and knowing that $v_{dr} = v_{qr} = 0$ for SCIM:

$$i_{dr} = \frac{1}{sL_r + r_r}(-\omega_r(L_s i_{qs} + L_r i_{qr}) - sL_s i_{ds}) \tag{2.39}$$
$$i_{qr} = \frac{1}{sL_r + r_r}(\omega_r(L_s i_{ds} + L_r i_{dr}) - sL_s i_{qs}) \tag{2.40}$$

(2.37)-(2.40) define the IM electrical system model. The block diagram for the rotor current model is shown in fig. 2.13.

For the mechanical system the electromechanical power P_{em} produced by the IM is defined as, [15]:

$$P_{em} = \frac{3}{2}P\omega_m L'_m(i_{qs}i_{dr} - i_{ds}i_{qr}) = \frac{3}{2}P\omega_m L_s(i_{qs}i_{dr} - i_{ds}i_{qr}) \tag{2.41}$$

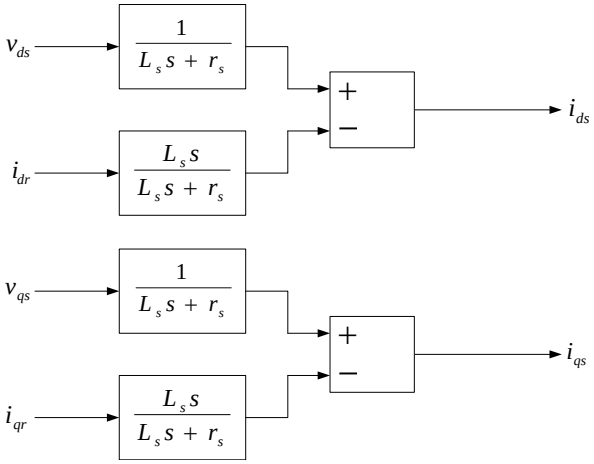

Figure 2.12: *Electrical system - Stator currents.*

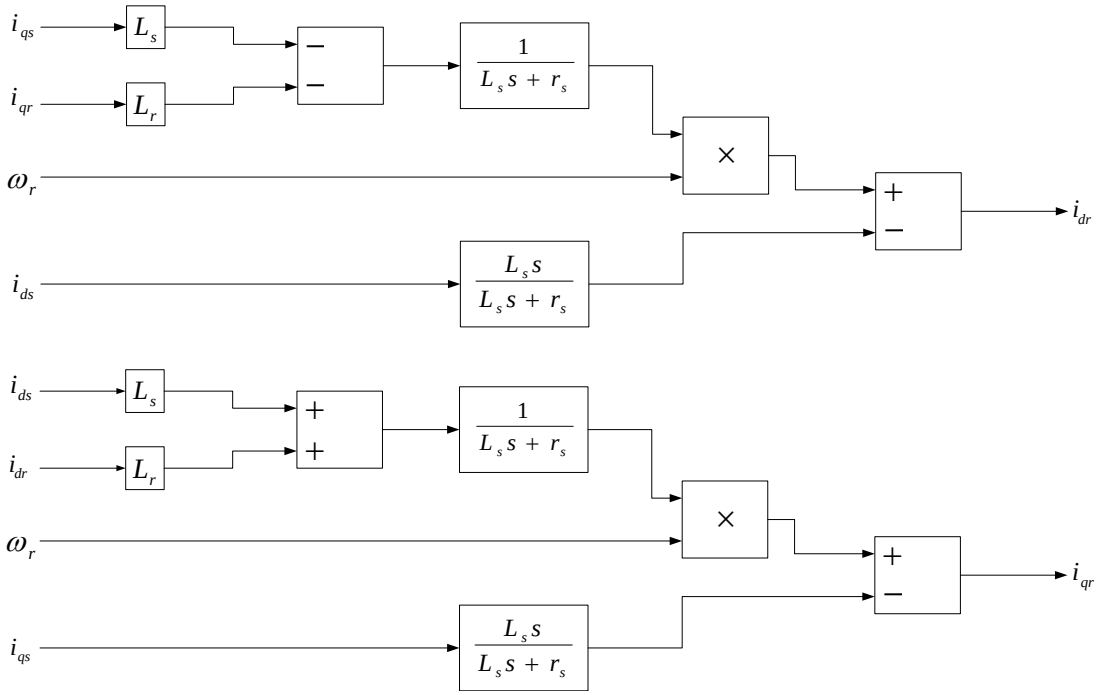

Figure 2.13: *Electrical system - Rotor currents.*

where P is the number of pole-pairs of the IM, $L'_m = L_s$ because of the previously defined γ and ω_m is the mechanical speed of the rotor which is related to the electrical speed by:

$$\omega_r = P \cdot \omega_m \tag{2.42}$$

The produced electromechanical torque T_{em} is then:

$$T_{em} = \frac{P_{em}}{\omega_m} = \frac{3}{2} P L_s \left(i_{qs} i_{dr} - i_{ds} i_{qr} \right) \tag{2.43}$$

To describe the electromechanical behaviour of the IM the simplest form is used [15]:

$$T_{em} = J \frac{d\omega_m}{dt} + T_L \tag{2.44}$$

where J is the inertia of the shaft and T_L is the applied load torque.

Rearranging (2.44) and transforming to s-domain gives the rotor speed in mechanical degrees:

$$\omega_m = \frac{1}{Js} \left(T_{em} - T_L \right) \tag{2.45}$$

Block diagram of the mechanical system is shown in fig. 2.14.

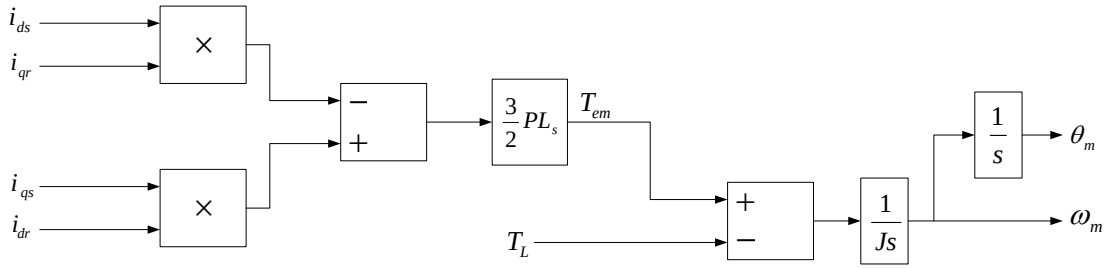

Figure 2.14: *Mechanical system of IM model.*

2.5 Sensorless V/f control

To be consistent with project purpose of a low-cost design, a sensorless speed controller has to be implemented. Because of its simplicity, V/f control is widely used despite its inferior performance compared to the vector control methods. To increase accuracy, the open loop V/f control requires compensation for stator resistance voltage drop and slip frequency. Stator resistance voltage drop can be easily compensated by the knowledge of stator resistance but slip compensation requires knowledge of the rotor speed which can be available through an encoder or speed tachometer. But the slip frequency can also be obtained without the sensor using stator voltages and currents. This preserves the mechanical robustness of the SCIM and decreases the cost of the drive, [17].

The method used is explained in [18] and estimates the slip speed by estimating the electromagnetic torque and the flux component of the stator current in the rotor flux oriented reference frame. The stator voltage drop is partially estimated using the torque component of the stator current in the rotor flux oriented reference frame. This is announced to be more efficient than full compensation in keeping the flux from saturating.

Open loop V/f control

To explain the theory behind the open loop V/f control the dynamic model of the SCIM in synchronous reference frame has to be observed, [17]:

$$s\lambda_{sd}^{e} = v_{sd}^{e} - r_s i_{sd}^{e} + \omega_e \lambda_{sq}^{e} \tag{2.46}$$
$$s\lambda_{sq}^{e} = v_{sq}^{e} - r_s i_{sq}^{e} + \omega_e \lambda_{sd}^{e} \tag{2.47}$$

where the superscript e denotes a variable in the synchronous reference frame.

In the synchronous reference frame all stator variables become constant during steady state. Also, if the flux vector is assigned to the d-axis the flux component on the q-axis is zero. (2.46) and (2.47) then reduce to:

$$v_{sd}^{e} = r_s i_{sd}^{e} \tag{2.48}$$
$$v_{sq}^{e} = r_s i_{sq}^{e} + \omega_e \lambda_s \tag{2.49}$$

If the stator resistance is neglected the stator voltage vector becomes:

$$|\vec{v}_s| \approx \omega_e \lambda_s \tag{2.50}$$

(2.50) shows that constant flux can be obtained by keeping the ratio between frequency and stator voltage constant. It is desired to hold the flux at its rated value, thus for a given reference frequency f_{ref} the peak value of the stator voltage should be:

$$|V_s| = \frac{V_n}{f_n} f_{ref} \tag{2.51}$$

where V_n and f_n are the nominal voltage and frequency of the motor, respectively.

Rotor flux observer

The dynamic model of the SCIM can be described by the following equations in the $\alpha\beta$ reference frame using the Γ-model:

$$v_{s\alpha} = r_s i_{s\alpha} + s\lambda_{s\alpha} \tag{2.52}$$
$$v_{s\beta} = r_s i_{s\beta} + s\lambda_{s\beta} \tag{2.53}$$
$$0 = r_r i_{r\alpha} + s\lambda_{r\alpha} + \omega_r \lambda_{r\beta} \tag{2.54}$$
$$0 = r_r i_{r\beta} + s\lambda_{r\beta} - \omega_r \lambda_{r\alpha} \tag{2.55}$$

Where the flux linkages are expressed as:

$$\lambda_{s\alpha} = L_s \left(i_{s\alpha} + i_{r\alpha}\right) \tag{2.56}$$
$$\lambda_{s\beta} = L_s \left(i_{s\beta} + i_{r\beta}\right) \tag{2.57}$$
$$\lambda_{r\alpha} = L_s i_{s\alpha} + L_r i_{r\alpha} \tag{2.58}$$
$$\lambda_{r\beta} = L_s i_{s\beta} + L_r i_{r\beta} \tag{2.59}$$

The stator flux can be estimated by isolating the stator flux component in (2.52) and (2.53):

$$\lambda_{s\alpha} = \int (v_{s\alpha} - r_s i_{s\alpha})\, dt \tag{2.60}$$

$$\lambda_{s\beta} = \int (v_{s\beta} - r_s i_{s\beta})\, dt \tag{2.61}$$

To prevent the DC drift and initial value problem of the pure integrator it is replaced by a modified integrator explained in [19]. Block diagram of the modified integrator is shown in fig. 2.15, where L is the nominal stator flux.

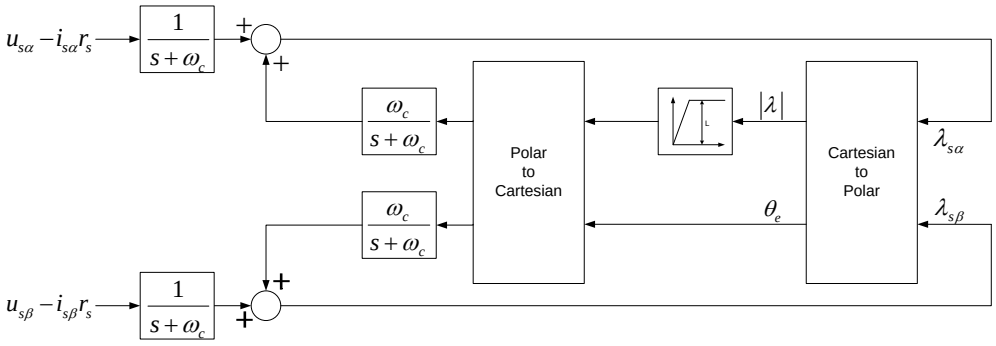

Figure 2.15: *Modified integrator.*

From (2.56) and (2.57) the rotor currents can be expressed as:

$$i_{r\alpha} = \frac{\lambda_{s\alpha}}{L_s} - i_{s\alpha} \tag{2.62}$$

$$i_{r\beta} = \frac{\lambda_{s\beta}}{L_s} - i_{s\beta} \tag{2.63}$$

Inserting into (2.58) and (2.59) gives the rotor flux:

$$\lambda_{r\alpha} = \frac{L_r}{L_s}\lambda_{s\alpha} - (L_r - L_s)\, i_{s\alpha} \tag{2.64}$$

$$\lambda_{r\beta} = \frac{L_r}{L_s}\lambda_{s\beta} - (L_r - L_s)\, i_{s\beta} \tag{2.65}$$

The rotor position can now be obtained as the angle between the rotor flux components, $\lambda_{r\alpha}$ and $\lambda_{r\beta}$:

$$\theta_r = \arctan\left(\frac{\lambda_{r\beta}}{\lambda_{r\alpha}}\right) \tag{2.66}$$

Thus all variables can be transformed to the rotor flux oriented reference frame. The implementation of the r_s and slip compensator requires the stator currents in the rotor flux oriented reference frame:

$$i_{sd}^r = i_{s\alpha}\cos\theta_r + i_{s\beta}\sin\theta_r \tag{2.67}$$

$$i_{sq}^r = -i_{s\alpha}\sin\theta_r + i_{s\beta}\cos\theta_r \tag{2.68}$$

where the superscript r denotes variables represented in the rotor flux oriented reference frame.

Stator resistance compensation

The stator resistance voltage drop can be fully compensated using the triangular relationship [20]:

$$V_s = I_s r_s \cos\phi + \sqrt{E_s^2 - (I_s r_s \sin\phi)^2} \tag{2.69}$$

But this method tends to overcompensate the voltage resulting in saturation of the stator flux especially when the load torque decreases, [18]. This method is especially useful in low frequency situations like starting the SCIM with large load. For low stator frequency the rotor leakage is small enough to be omitted. The T-model equivalent circuit of the induction motor then becomes as shown in fig. 2.16. Drawing the vector diagram of this circuit, fig. 2.17, shows that the i_{sq} current is now directly proportional to the airgap emf vector E_m. Therefore, to maintain constant airgap flux, only the stator resistance voltage drop related to the i_{sq} component needs to be compensated.

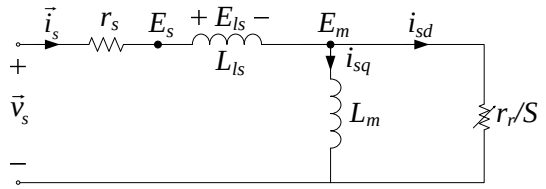

Figure 2.16: *Simplified T-model of SCIM at low frequency.*

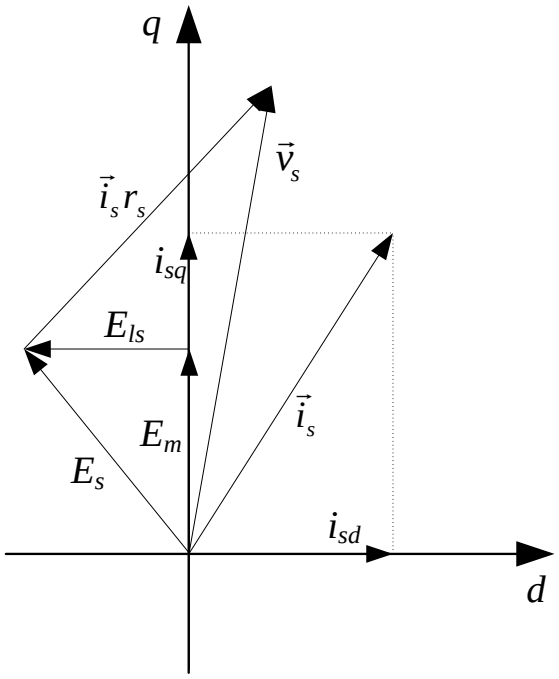

Figure 2.17: *Vector diagram of SCIM at low frequency.*

The stator voltage with added compensation then becomes:

$$V_s^* = V_s + E_m i_{sq}^r \tag{2.70}$$

While this approximation is only valid at a low stator frequency it is applicable where project is limited to low speed performance.

Slip compensation

In the rotor flux oriented reference frame the slip speed ω_{sl} can be denoted as, [18]:

$$\omega_{sl} = \frac{T_{em} r_r'}{P\left(L_m'\right)^2 i_{sd}^2} \tag{2.71}$$

In the Γ-model, (2.71) becomes:

$$\omega_{sl} = \frac{T_{em} r_r'}{P L_s^2 i_{sd}^2} \tag{2.72}$$

Knowing that the electromagnetic torqe can be described by:

$$T_{em} = \frac{3}{2} P \left(\lambda_{s\alpha} i_{s\beta} - \lambda_{s\beta} i_{s\alpha} \right) \tag{2.73}$$

and the d-component of the stator current can be obtained from (2.67), the slip speed can easily be calculated and added to the reference speed. Block diagram of the whole sensorless control scheme is shown in fig. 2.18 and block diagram of the open loop V/f control is shown in fig. 2.19. Lowpass filters are necessary to minimize ripple in frequency reference due to ripple in feedback signals, $v_{s\alpha}$, $v_{s\beta}$, $i_{s\alpha}$ and $i_{s\beta}$.

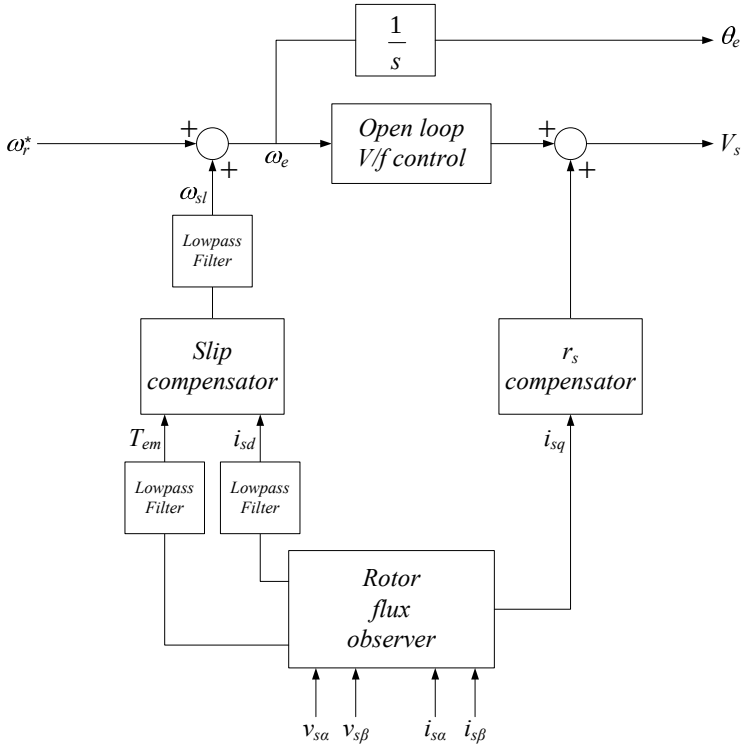

Figure 2.18: *Block diagram of sensorless V/f control.*

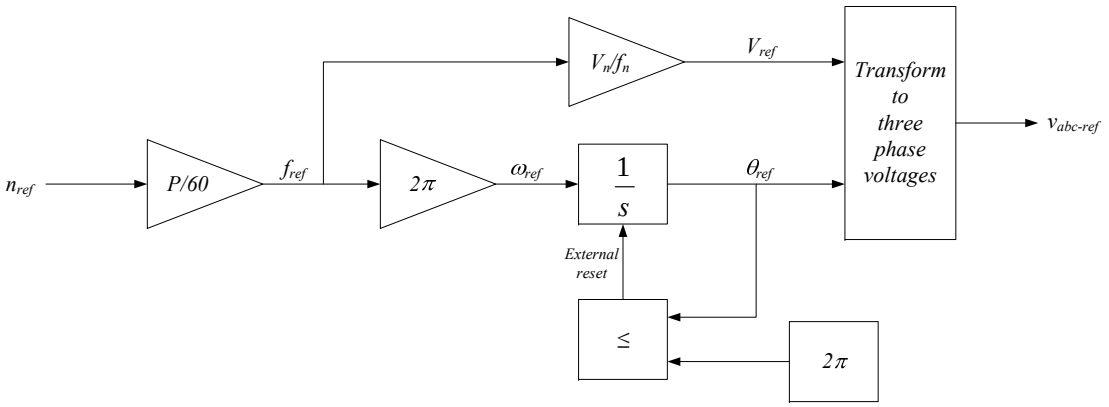

Figure 2.19: *Block diagram of open loop V/f control.*

2.6 Simulations

The system is simulated in Matlab/Simulink 7.4.0 (R2007a) to verify the sensorless V/f control and compare it to the open loop V/f control.

Block diagram of the simulation setup is shown in fig. 2.20. All components, except for the diode rectifier and DC link models which were obtained from supervisor, have been studied in this chapter. The average model is used where the focus is on steady state behavior and to speed up simulation times. For increased accuracy, the model for sampling delay is replaced by the transfer delay block which is part of the Simulink library. The parameters used are shown in table 2.1.

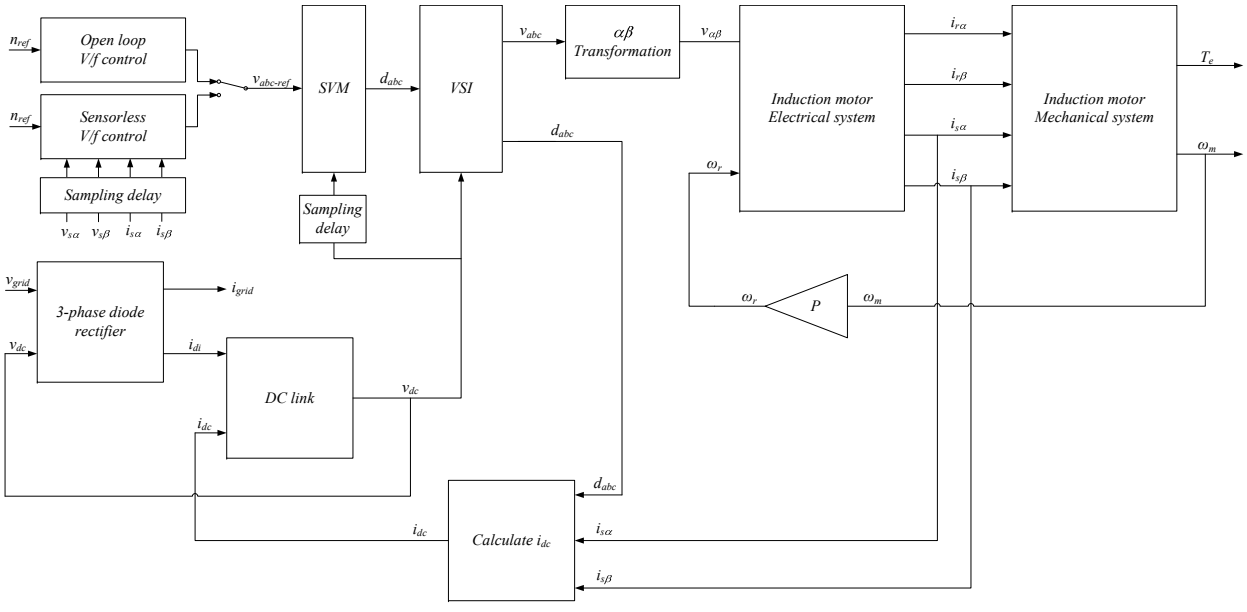

Figure 2.20: *Block diagram of simulated system.*

Each motor control method is simulated for two conditions, step in speed and step in load torque. The step in speed is from $n_n/2 = 715\ rpm$ to $n_n = 1430\ rpm$ while the torque is at $T_n/2 = 10\ Nm$. The step in load torque is from $T_n/2 = 10\ Nm$ to $T_n = 20\ Nm$ while the speed is at $n_n = 1430\ rpm$.

Parameters		
Mains input voltage	V_{in}	$230\sqrt{2}\ V_{peak}$
Mains resistance	R_g	$0.5\ \Omega$
Mains inductance	L_g	$0.1\ mH$
DC link capacitance	C	$500\ \mu F$
Stator resistance	r_s	$1.79\ \Omega$
Stator leakage inductance	L_{ls}	$7\ mH$
Mutual inductance	L_m	$0.158\ H$
Rotor resistance	r_r	$1.8\ \Omega$
Rotor leakage inductance	L_{lr}	$0.0144\ H$
Pole pairs	P	2
Motor shaft inertia	J	$9.57\ mNm^2$
Sample delay	T_d	$0.5\ ms$
Switching frequency	f_{sw}	$6\ kHz$
Lowpass filter cutoff frequency	ω_c	$2\pi\ rad/s$
Motor nameplate		
Nominal power	P_n	$3.0\ kW$
Nominal phase voltage	V_n	$380/\sqrt{3}\ V_{rms}$
Nominal current	I_n	$6.9\ A_{rms}$
Nominal frequency	f_n	$50\ Hz$
Nominal power factor	PF	0.77
Nominal speed	n_n	$1430\ rpm$
Nominal torque	T_n	$20\ Nm$

Table 2.1: *Model parameters.*

Case 1a: Open loop V/f control - Speed step

Fig.s 2.21 and 2.23 show the DC link voltage and the DC link current, that is the current going into the inverter. Due to the speed step, the DC link current increases as the stator voltage has been increased over the stator resistance. It can be observed that the average value of the DC link voltage decreases which should not occur if compared to simulations using PLECS in section 3.4. It is also observed that the ripples are increased in the DC link voltage which is also unusual where the diode rectifier always soft-switches. Looking closer at the DC link voltage shows that it only contains harmonics of 300 Hz from the diode rectifier and no switching harmonics. This was expected as the average model was being used. The ripple in the DC link voltage should therefore not increase. This could be caused by poor accuracy of the model that was used in the simulation but this is not of so much concern in this section where the focus is on comparing the open loop V/f control to the sensorless V/f control.

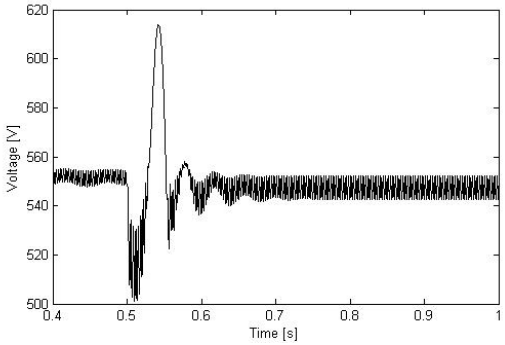

Figure 2.21: *V/f control. DC link voltage at speed step.*

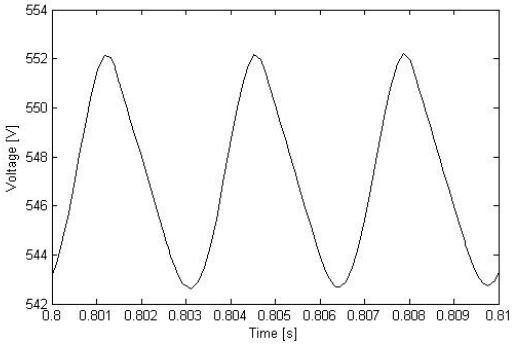

Figure 2.22: *V/f control. Zoom on DC link voltage.*

Due to doubling in speed reference, the V/f control doubles the voltage which is in correspondance with the V/f control, fig. 2.24.

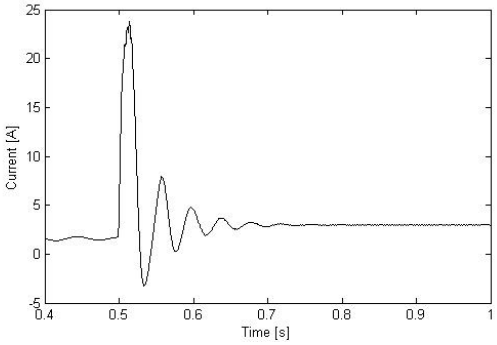

Figure 2.23: *V/f control. DC link current at speed step.*

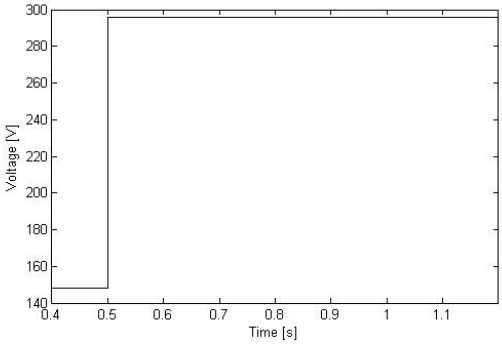

Figure 2.24: *V/f control. Peak value of reference voltage.*

The rotor speed and electromagnetic torque are affected by the fluctuations in the DC link voltage and contain rippled content. The torque is then the same before and after the speed step where no change in load occured. The rotor speed is changed but is lower than the reference due to stator resistance and slip, where applied load is $T_n/2 = 10\ Nm$. These factors are not taken into account in the open loop V/f control and therefore a large error in rotor speed is encountered.

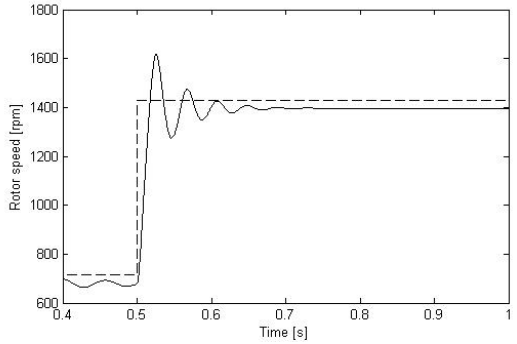

Figure 2.25: *V/f control. Rotor speed at speed step.*

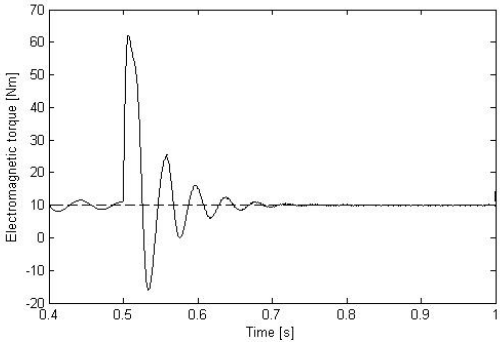

Figure 2.26: *V/f control. Electromagnetic torque at speed step.*

Case 1b: Open loop V/f control - Torque step

At the time of torque step, the DC link current is increased as the torque is only proportional to the current when the flux is held constant, fig. 2.28. The DC link voltage should not be affected but actually get affected due to inaccurate modeling, 2.27.

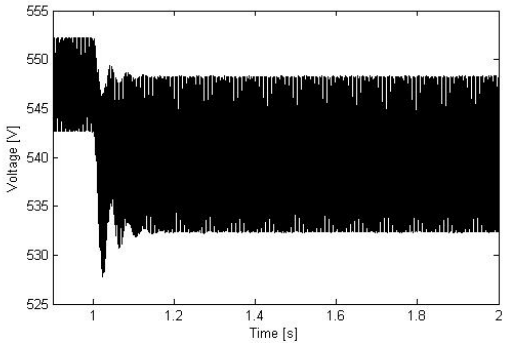

Figure 2.27: *V/f control. DC link voltage at torque step.*

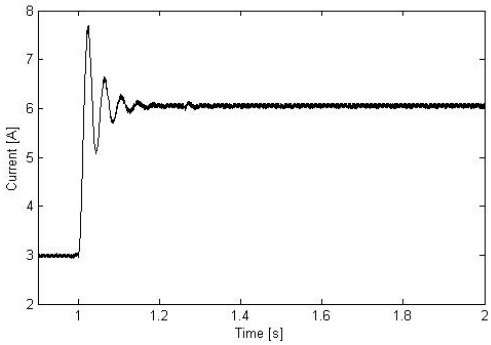

Figure 2.28: *V/f control. DC link current at torque step.*

As seen from fig. 2.29, the rotor speed is even further from the reference both due to the increase in slip and increase in stator current. It can be observed in fig. 2.24 that no change occurs in the reference stator voltage at the instance of torque step, at time $t = 1$ *sec.*

The torque step increases the electromagnetic torque of the motor which needs to match the load torque to maintain speed, fig. 2.30.

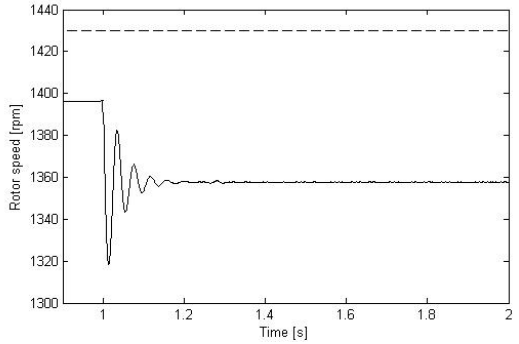

Figure 2.29: *V/f control. Rotor speed at torque step.*

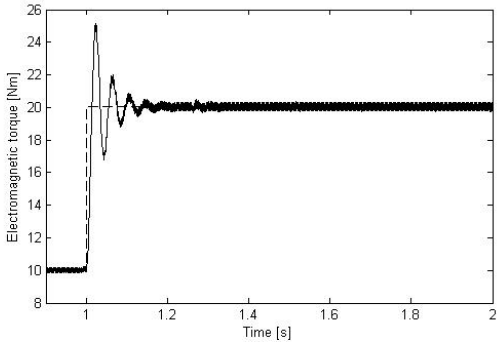

Figure 2.30: *V/f control. Electromagnetic torque at torque step.*

Case 2a: Sensorless V/f control - Speed step

Now, the stator voltages and currents are fed back to the V/f controller to allow compensation for stator resistance and slip. But due to ripples in current and voltage and sample delays, the sensed signals also contain ripples which induces more ripples. This is seen from the DC link current and voltage which fluctuate more erratically than before, fig.s 2.31 and 2.32.

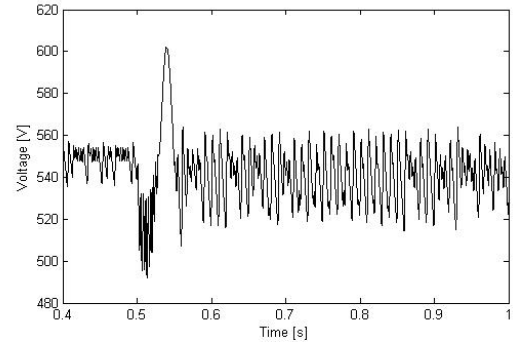

Figure 2.31: *Sensorless V/f control. DC link voltage at speed step.*

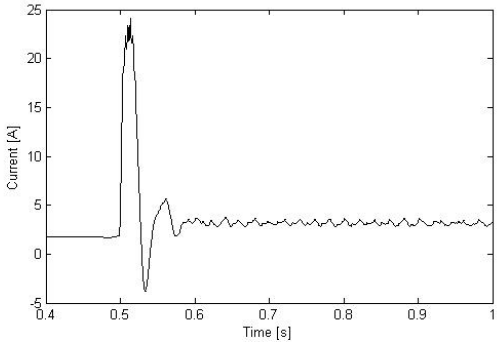

Figure 2.32: *Sensorless V/f control. DC link current at speed step.*

It can be seen from fig. 2.33 that the reference voltage saturates at the instance of the speed step. This is because the current is limited in the sensorless V/f controller. But the reference voltage is now higher than in Case 1a because the voltage drop over the stator resistance is taken into account. The slip speed is seen in fig. 2.34 and its response is bounded by the lowpass filters in the controller. The lowpass filters are 1st order and are all put to rather low cutoff frequency ($\omega_c = 2\pi$) which introduces slow response with low harmonic content. If examined closely, it can be seen that the sensed slip speed reaches steady state little before $t = 2$ *sec* in fig. 2.34, the load step discussed in next subsection is applied at time $t = 1$ *sec*.

Because of the sensorless control the rotor speed is now closer to the reference than in Case 1a but the speed is a little bit over estimated. The torque is similiar as in Case 1a but it is seen that the ripples in the reference voltage propagate to the torque, fig. 2.36.

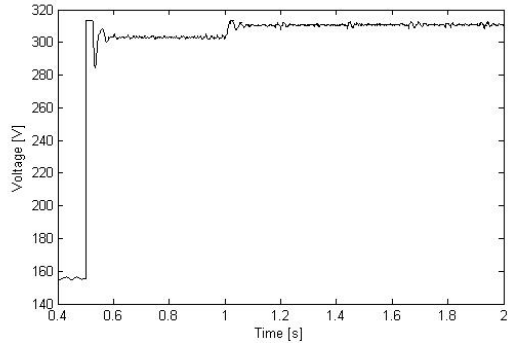

Figure 2.33: *Sensorless V/f control. Peak value of reference voltage.*

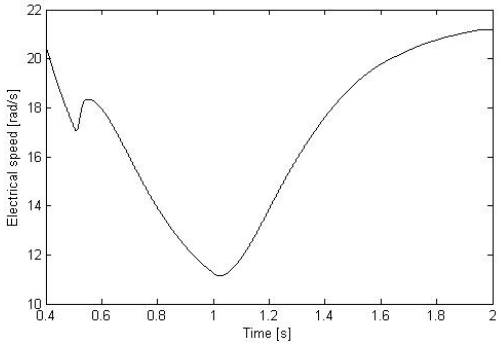

Figure 2.34: *Sensorless V/f control. Sensed slip speed.*

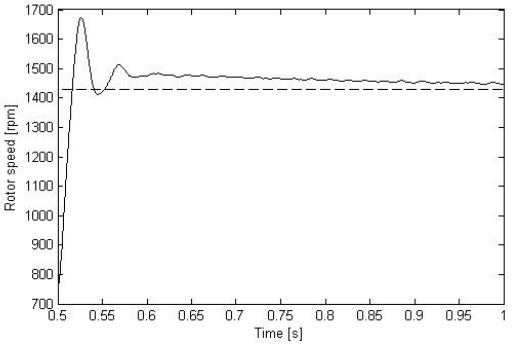

Figure 2.35: *Sensorless V/f control. Rotor speed at speed step.*

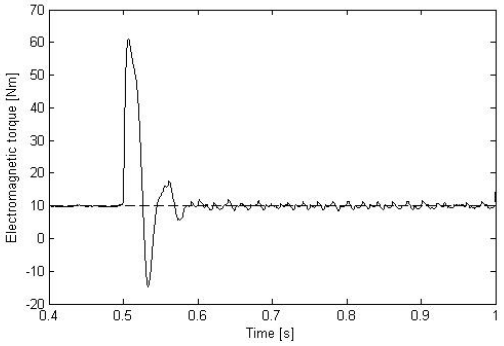

Figure 2.36: *Sensorless V/f control. Electromagnetic torque at speed step.*

Case 2b: Sensorless V/f control - Torque step

As in case 1b the torque step increases the DC link current resulting in lower DC link voltage. The DC link voltage and current fluctuate more erratically because of the ripples in the reference voltage.

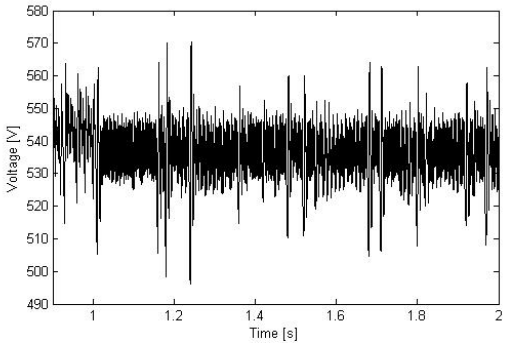

Figure 2.37: *Sensorless V/f control. DC link voltage at torque step.*

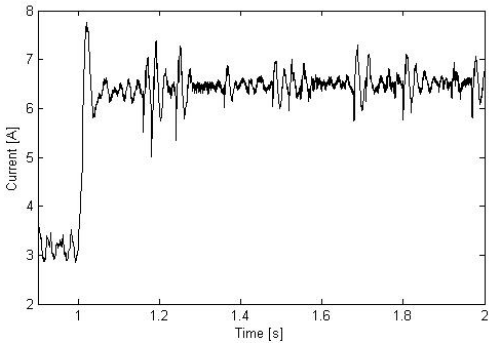

Figure 2.38: *Sensorless V/f control. DC link current at torque step.*

The rotor speed decreases due to the load step but the speed controller increases the speed to almost the same value as before the load step. The electromagnetic torque follows the load torque and fluctuates due to the DC link current and reference voltage ripples.

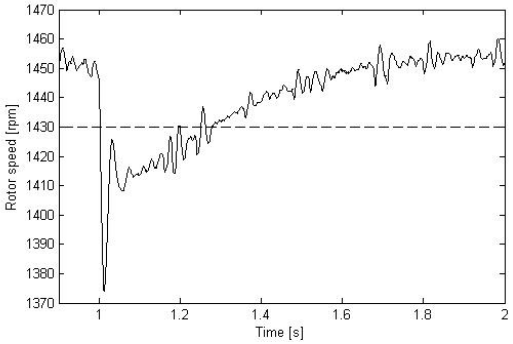

Figure 2.39: *Sensorless V/f control. Rotor speed at torque step.*

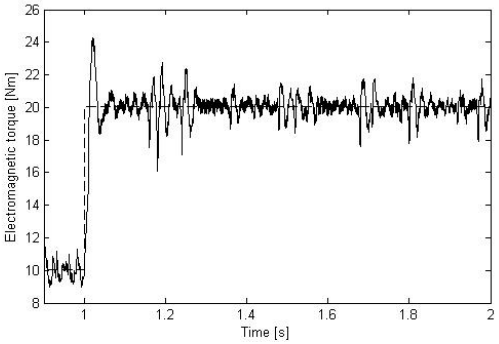

Figure 2.40: *Sensorless V/f control. Electromagnetic torque at torque step.*

2.7 Summary

Components of the system, delay, modulation and a control strategy have all been modeled and studied in this chapter except for the diode rectifier and DC link models which were obtained from supervisor. Although the model for time delay was not used in simulations it was necessary to derive where it will be used in next chapter.

Simulations showed that better speed accuracy is acquired with the sensorless V/f control but more ripples are introduced in rotor speed and electromagnetic torque. These ripples are caused by ripples in stator currents and voltages which causes ripples in the calculated slip speed and voltage references. Due to this, the ripples basically propagate through the system and become more severe because of sampling delay. As fast dynamics are not of concern in the system, a solution could be to put a filter on all feedback signals. This would give slower response but ripples would be reduced. In practice, the stator voltages would at least have to be filtered because of the PWM controlled inverter. But because an average model was used in the simulation, filtering of stator voltages was not necessary.

Chapter 3

Stability analysis and DC link dimensioning

In this chapter a small signal model of the system is obtained and the corresponding transfer functions are used for stability analysis and to evaluate the effect of different parameters on stability. Then the converter considered in the project and the converter used in implementation from Danfoss are compared with simulations. Finally, the stability analysis is evaluated by attempts to create an unstable condition with simulations based on the stability analysis.

3.1 Deriving the transfer functions

With a small DC link capacitor the DC link voltage fluctuates heavily. To examine if this can cause the system to become unstable the frequency converter has to be linearized in order to find a transfer function describing the system. The system has two inputs, grid side voltage and frequency reference for the SCIM. To investigate the stability behavior on the DC link voltage caused by these inputs, a linear relationship between these terms is needed. In this section these relationships are derived.

Simplified model of frequency converter

Circuit diagram of the frequency converter without the inverter is shown in fig. 3.1. To obtain the linearized model of the frequency converter, a simplified model will be used, shown in fig. 3.2, [5]. The simplified model assumes that the diode rectifier is always working in discontinuous conduction mode. Therefore only two diodes conduct at once, [1]. This assumption can be made where the only inductance involved is the mains inductance which is low in practice and causes a discontinuous grid side current, [2]. In the simplified model the mains impedances have been moved to the DC link and the diode rectifier has been replaced with a voltage source which has the output of an ideal diode rectifier.

From the simplified circuit the following system model can be derived:

$$v_{dc} = \frac{1}{s^2 C L'_g + sCR'_g + 1} v_g + \frac{sL'_g + R'_g}{s^2 C L'_g + sCR'_g + 1} i_{dc} \tag{3.1}$$

where L'_g and R'_g are defined as:

$$L'_g = 2L_g \qquad R'_g = 2R_g + 3\omega_g L_g/\pi \tag{3.2}$$

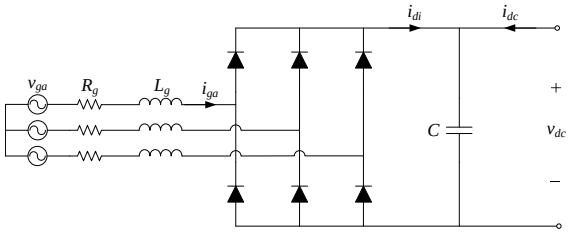

Figure 3.1: *Circuit diagram of frequency converter.*

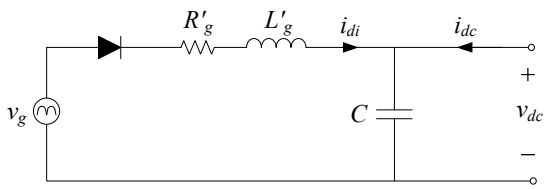

Figure 3.2: *Simplified circuit diagram of frequency converter.*

where ω_g is the angular frequency of the grid side voltage and the term $3\omega_g L_g/\pi$ denotes the nonohmic losses due to noninstantaneous commutation of diodes, [1] [5].

Where (3.1) is linear, the small signal model can easily be obtained:

$$\hat{v}_{dc} = \frac{1}{s^2CL'_g + sCR'_g + 1}\hat{v}_g + \frac{sL'_g + R'_g}{s^2CL'_g + sCR'_g + 1}\hat{i}_{dc} \tag{3.3}$$

where the transfer functions that describe the system are:

$$G_{vg}(s) = \left(\frac{\hat{v}_{dc}}{\hat{v}_g}\right)_{\hat{i}_{dc}=0} = \frac{1}{s^2CL'_g + sCR'_g + 1} \tag{3.4}$$

$$G_{vi}(s) = \left(\frac{\hat{v}_{dc}}{\hat{i}_{dc}}\right)_{\hat{v}_g=0} = \frac{sL'_g + R'_g}{s^2CL'_g + sCR'_g + 1} \tag{3.5}$$

But where i_{dc} is not a control variable, G_{vi} is not useful in its present form. i_{dc} has to be replaced by a control variable, which in this case is ω_e.

Relationship between i_{dc} and ω_e

As mentioned before the transfer functions have to give a linear relationship between v_{dc} and the two control inputs of the system, v_g and ω_e. Before being able to derive these transfer functions a linear relationship has to be found between i_{dc} and ω_e resulting in the correpsonding small signal model between these variables.

The sum of all losses in the inverter and motor should equal the DC link power:

$$v_{dc}i_{dc} = P_{inv} + P_{Cu} + P_f + P_{em} \tag{3.6}$$

where P_{inv} denotes the losses in the inverter, P_{Cu} the resistive losses in the SCIM, P_f the core losses and P_{em} the power converted to electromagnetic power. Assuming that the losses are small compared to the produced electrommagnetic power and that the system is operating in steady state, (3.6) can be simplified to:

$$v_{dc}i_{dc} = P_{em} \tag{3.7}$$

The electromagnetic power can be expressed as a function of the electromagnetic torque T_{em} and electrical speed ω_e.

$$P_{em} = T_{em}\frac{\omega_e}{P} \tag{3.8}$$

P being the number of pole-pairs.

Then i_{dc} can be expressed as:

$$i_{dc} = \frac{T_{em}}{v_{dc}} \frac{\omega_e}{P} \tag{3.9}$$

The modulation coefficient is defined as, [21]:

$$m_a = \frac{\pi}{2} \frac{v_s}{v_{dc}} \tag{3.10}$$

Isolating v_{dc} and inserting into (3.9) gives:

$$i_{dc} = \frac{2}{\pi} \frac{T_{em}}{v_s} \frac{m_a}{P} \omega_e \tag{3.11}$$

Now, (3.11) is nonlinear because it contains products of time-varying variables. (3.11) can be linearized by denoting each variable by its quiscent value and small AC variation at a certain operating point, [2]. Quiscent values are denoted by a captial letter or are followed by ^{q} notation. Small AC varying variables are denoted with a $\hat{}$. Linearizing (3.11) gives:

$$I_{dc} + \hat{i}_{dc} = \frac{2}{\pi} \frac{1}{P} \frac{T_{em}^q + \hat{T}_{em}}{V_s + \hat{v}_s} \left(\Omega_e + \hat{\omega}_e\right) \left(M_a + \hat{m}_a\right) \tag{3.12}$$

After few steps (3.12) becomes:

$$I_{dc} + V_s \frac{\hat{i}_{dc}}{\hat{v}_s} = \frac{2}{\pi} \frac{1}{P} \left(T_{em}^q \frac{\hat{\omega}_e}{\hat{v}_s} + \Omega_e \frac{\hat{T}_{em}}{\hat{v}_s} \right) \left(M_a + \hat{m}_a\right) \tag{3.13}$$

Now, $\hat{v}_s$ can be replaced using the V/f ratio from (2.51). This ratio is linear and the small signal model is therefore easily obtained:

$$\hat{v}_s = \frac{V_n}{\omega_n} \hat{\omega}_e \tag{3.14}$$

Putting (3.14) into (3.13) and isolating $\hat{i}_{dc}$ then gives:

$$\hat{i}_{dc} = \frac{2}{\pi} \frac{1}{P} \left(\frac{\Omega_e V_n}{\omega_n V_s} \frac{\hat{T}_{em}}{\hat{v}_s} + \frac{T_{em}^q}{V_s} \right) \left(M_a + \hat{m}_a\right) \hat{\omega}_e - \frac{I_{dc} V_n}{\omega_n V_s} \hat{\omega}_e \tag{3.15}$$

Calculating terms:

$$\hat{i}_{dc} = \frac{2}{\pi} \frac{1}{P} \left(\underbrace{M_a \frac{\Omega_e V_n}{\omega_n V_s} \frac{\hat{T}_{em}}{\hat{v}_s} \hat{\omega}_e}_{1st\ order} + \underbrace{\frac{\Omega_e V_n}{\omega_n V_s} \frac{\hat{T}_{em}}{\hat{v}_s} \hat{m}_a \hat{\omega}_e}_{2nd\ order} + \underbrace{M_a \frac{T_{em}^q}{V_s} \hat{\omega}_e}_{1st\ order} + \underbrace{\frac{T_{em}^q}{V_s} \hat{m}_a \hat{\omega}_e}_{2nd\ order} \right) - \underbrace{\frac{I_{dc} V_n}{\omega_n V_s} \hat{\omega}_e}_{1st\ order} \tag{3.16}$$

Now, (3.16) has been split up into 1st order and 2nd order AC terms. The 1st order AC terms are linear but the 2nd order AC terms contain products of time-varying AC quantities and are thereby nonlinear. Provided that the AC varying quantities are small, the 2nd order AC terms can be neglected, [2]. Then, (3.16) reduces to the desired relationship between $\hat{i}_{dc}$ and $\hat{\omega}_e$::

$$\hat{i}_{dc} = \left(\underbrace{\frac{2}{\pi} \frac{M_a}{P} \frac{\Omega_e V_n}{\omega_n V_s}}_{Constant} \underbrace{\frac{\hat{T}_{em}}{\hat{v}_s}}_{SCIM} + \underbrace{\frac{2}{\pi} \frac{M_a}{P} \frac{T_{em}^q}{V_s} - \frac{I_{dc} V_n}{\omega_n V_s}}_{Constant} \right) \hat{\omega}_e \tag{3.17}$$

But the term $\hat{T}_{em}/\hat{v}_s$ involves the SCIM, which has yet to be evaluated. Inserting (3.17) into (3.3) would give a product of two transfer functions, G_{vi} and $\hat{T}_{em}/\hat{v}_s$. So two systems are involved, the converter and the SCIM. This can be simplified considerably by comparing the poles of the two systems. Knowing that if a system contains poles that are insignificant compared to the more dominant system, the dynamics of the system can be ignored. The insignificant system can consequently be replaced by a gain. A diagram showing position of dominant and insignificant poles in the s-plane are shown in fig. 3.3. As a rule of thumb, in order to disregard the insignificant poles the ratio b/a needs to be 5 or larger, [22].

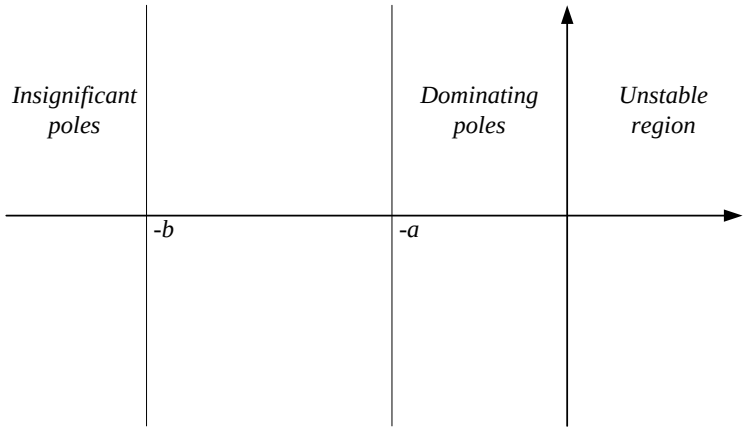

Figure 3.3: *Diagram showing locations of dominating and insignificant poles.*

If the converter is dominant the dynamics of the SCIM can be ignored and $\hat{T}_{em}/\hat{v}_s$ can be replaced by a constant T^q_{em}/V_s in (3.17). But if the SCIM is more dominant, the converter has little effect in this term. It can therefore be omitted where all instability behavior is determined by the SCIM which is beyond the scope of this project where the focus is on instability caused by the converter.

But in order to check which system is more dominant the SCIM needs to be linearized to see the pole locations.

Linearized model of SCIM

A linearized small signal model of the SCIM using the Γ-model in the $dq0$-synchronous reference frame is shown in (3.18), [16].

$$\begin{bmatrix} \hat{v}_{ds} \\ \hat{v}_{qs} \\ \hat{v}_{dr} \\ \hat{v}_{qr} \\ \hat{T}_L \end{bmatrix} = \begin{bmatrix} r_s + sL_s & -\omega_e L_s & sL_s & -\omega_e L_s & 0 \\ \omega_e L_s & r_s + sL_s & \omega_e L_s & sL_s & 0 \\ sL_s & -\omega_{sl} L_s & r_r + sL_r & -\omega_{sl} L_r & L_s I_{qs} + L_r I_{qr} \\ \omega_{sl} L_s & sL_s & \omega_{sl} L_r & r_r + sL_r & -L_s I_{ds} - L_r I_{dr} \\ -L_s I_{qr} & L_s I_{dr} & L_s I_{qs} & -L_s I_{ds} & sJ \end{bmatrix} \begin{bmatrix} \hat{i}_{ds} \\ \hat{i}_{qs} \\ \hat{i}_{dr} \\ \hat{i}_{qr} \\ \hat{\omega}_r \end{bmatrix} \tag{3.18}$$

where $\omega_{sl} = \omega_e - \omega_r$ is the slip speed and I_{ds}, I_{qs}, I_{dr}, I_{qr} are the desired operating point and are found by simulation.

As described in [16], it is convenient to divide the derivative and non-derivative terms into two matrices:

$$\mathbf{E} = \begin{bmatrix} L_s & 0 & L_s & 0 & 0 \\ 0 & L_s & 0 & L_s & 0 \\ L_s & 0 & L_r & 0 & 0 \\ 0 & L_s & 0 & L_r & 0 \\ 0 & 0 & 0 & 0 & -J \end{bmatrix} \tag{3.19}$$

$$\mathbf{F} = -\begin{bmatrix} r_s & -\omega_e L_s & 0 & -\omega_e L_s & 0 \\ \omega_e L_s & r_s & \omega_e L_s & 0 & 0 \\ 0 & -\omega_{sl} L_s & r_r & -\omega_{sl} L_r & L_s I_{qs} + L_r I_{qr} \\ \omega_{sl} L_s & 0 & \omega_{sl} L_r & r_r & -L_s I_{ds} - L_r I_{dr} \\ -L_s I_{qr} & L_s I_{dr} & L_s I_{qs} & -L_s I_{ds} & 0 \end{bmatrix} \tag{3.20}$$

So the the matrix equation takes the form:

$$\mathbf{u} = (s\mathbf{E} - \mathbf{F})\,\mathbf{x} \tag{3.21}$$

where

$$\mathbf{u} = \begin{bmatrix} \hat{v}_{ds} & \hat{v}_{qs} & \hat{v}_{dr} & \hat{v}_{qr} & \hat{T}_L \end{bmatrix}^T \qquad \mathbf{x} = \begin{bmatrix} \hat{i}_{ds} & \hat{i}_{qs} & \hat{i}_{dr} & \hat{i}_{qr} & \hat{\omega}_r \end{bmatrix}^T \tag{3.22}$$

and a linear differential equation of the SCIM can be directly obtained from (3.21), [16]:

$$s\mathbf{x} = \mathbf{E}^{-1}\mathbf{F}\mathbf{x} + \mathbf{E}^{-1}\mathbf{u} \tag{3.23}$$

For the SCIM it is desired to obtaine a linear relationship between the peak value of the stator voltage v_s and the produced electromagnetic torque T_{em}. This gives the variation in T_{em} for a disturbance in v_s.

In general control theory while examining one disturbance all other disturbances can be put to zero. Therefore all inputs except for v_{ds} and v_{qs} are put to zero in the input vector $\mathbf{u}$:

$$\mathbf{u} = [v_{ds}\ v_{qs}\ 0\ 0\ 0\ 0]^T \tag{3.24}$$

Now, the stator voltage in the synchronous dq-reference frame has to be transformed to the peak value of the stator voltage in the abc-reference frame using (3.25) and (3.26), [16]:

$$v_{ds} = v_s \cos(\theta - \theta_e) \tag{3.25}$$

$$v_{qs} = -v_s \sin(\theta - \theta_e) \tag{3.26}$$

where θ is the angle of the $dq0$-reference frame and θ_e is the angle of the input voltage.

In the synchronous reference frame, θ is rotating at synchronous speed which is determined by the input voltage with angle θ_e. θ and θ_e are therefore travelling at the same speed which makes the difference between them a constant. This constant depends only on the initial position of the reference frame which can be chosen arbitarily. Here, the d-axis is chosen to be aligned with the a-axis, therefore $\theta - \theta_e = 0$:

$$v_{ds} = v_s \cos 0 \tag{3.27}$$

$$v_{qs} = -v_s \sin 0 \tag{3.28}$$

Assuming that the voltage changes only in magnitude but not in phase, ensuring $\theta_e - \theta = constant$, (3.27) and (3.28) are linear and the small signal model can be obtained directly:

$$\hat{v}_{ds} = \hat{v}_s \cos 0 \tag{3.29}$$

$$\hat{v}_{qs} = -\hat{v}_s \sin 0 \tag{3.30}$$

The voltage vector $\mathbf{u}$ can then be expressed as:

$$\mathbf{u} = \mathbf{G}\hat{v}_s \tag{3.31}$$

where

$$\mathbf{G} = [\cos 0 \ \ -\sin 0 \ 0 \ 0 \ 0]^T = [1 \ 0 \ 0 \ 0 \ 0]^T \tag{3.32}$$

Now, an expression similiar to (3.23) has to be found for T_{em}. The electromagnetic torque is commonly expressed using the Γ-model as shown in (2.43), rewritten here for convenience:

$$T_{em} = \frac{3}{2} P L_s \left(i_{qs} i_{dr} - i_{ds} i_{qr} \right) \tag{3.33}$$

Linearizing (3.33) gives:

$$\hat{T}_{em} = \frac{3}{2} P L_s \left(I_{qs} \hat{i}_{dr} + I_{dr} \hat{i}_{qs} - I_{ds} \hat{i}_{qr} - I_{qr} \hat{i}_{ds} \right) \tag{3.34}$$

which can be expressed in matrix form as:

$$\mathbf{y} = \mathbf{C}\mathbf{x} \tag{3.35}$$

where $\mathbf{y} = [\hat{T}_{em}]$ and $\mathbf{C} = [-I_{qr} \ I_{dr} \ I_{qs} \ \ -I_{ds} \ 0]$.

Now, two sets of linear equations with two input vectors have been obtained:

$$s\mathbf{x} = \mathbf{E}^{-1}\mathbf{F}\mathbf{x} + \mathbf{E}^{-1}\mathbf{u} \tag{3.36}$$

$$\mathbf{y} = \mathbf{C}\mathbf{x} \tag{3.37}$$

Solving for $\mathbf{x}$ gives:

$$\mathbf{y} = \mathbf{C} \left(s\mathbf{I} - \mathbf{E}^{-1}\mathbf{F} \right)^{-1} \mathbf{E}^{-1}\mathbf{u} \tag{3.38}$$

Thus a linear relationship is obtained between $\mathbf{y}$ and $\mathbf{u}$. The desired transfer function is then:

$$\frac{\hat{T}_{em}}{\hat{v}_s} = \mathbf{C} \left(s\mathbf{I} - \mathbf{E}^{-1}\mathbf{F} \right)^{-1} \mathbf{E}^{-1} \tag{3.39}$$

where the poles of $\hat{T}_{em}/\hat{v}_s$ are the eigenvalues of $\mathbf{E}^{-1}\mathbf{F}$, [16].

Finalizing the transfer functions

Fig.s 3.4 and 3.5 show the poles of the two systems, $\hat{T}_{em}/\hat{v}_s$ and G_{vi}, for two different grid inductances, $L_g = 0.1\ mH$ and $L_g = 1\ mH$. Pole values are shown in table 3.1. As expected, where the SCIM contains also mechanical dynamics, the converter is a much faster system. The dynamics of the converter can therefore be ignored when the SCIM is involved and the term involving both $\hat{T}_{em}/\hat{v}_s$ and G_{vi} is omitted in the stability analysis of the converter.

The small signal model from (3.3) can then be written in the form:

$$\hat{v}_{dc} = \frac{1}{s^2 C L'_g + sCR'_g + 1} \hat{v}_g + \left(\frac{2}{\pi} \frac{M_a}{P} \frac{T^q_{em}}{V_s} - \frac{I_{dc} V_n}{\omega_n V_s} \right) \frac{sL'_g + R'_g}{s^2 C L'_g + sCR'_g + 1} \hat{\omega}_e \tag{3.40}$$

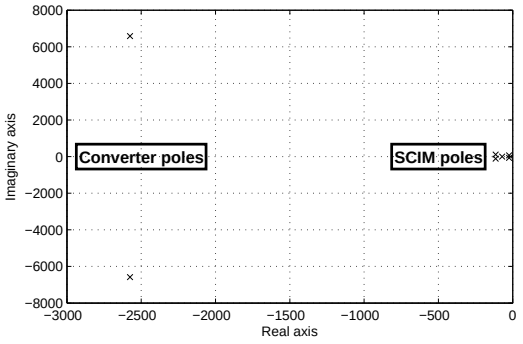

Figure 3.4: *Poles of converter and SCIM with* $L_g = 0.1\ mH$.

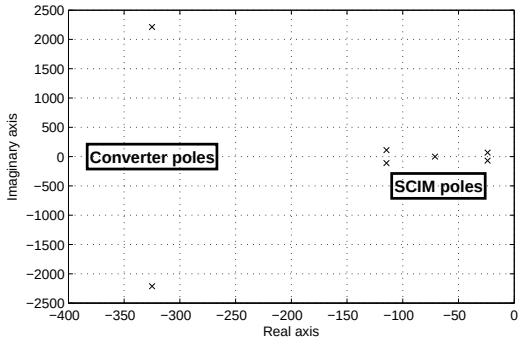

Figure 3.5: *Poles of converter and SCIM with* $L_g = 1\ mH$.

Pole locations			
$L_g = 0.1\ mH$		$L_g = 1\ mH$	
Converter	**SCIM**	**Converter**	**SCIM**
$-2575 \pm j6585.5$	$-114.66 \pm j110.87$ $-23.85 \pm j67.84$ -71.014	$-325 \pm j2212.3$	$-114.66 \pm j110.87$ $-23.85 \pm j67.84$ -71.01

Table 3.1: *Converter and SCIM poles.*

where the term involving the SCIM has been omitted.

The input-to-output and control-to-output transfer functions, $G_{vg}(s)$ and $G_{vd}(s)$, can now be obtained:

$$G_{vg}(s) = \left(\frac{\hat{v}_{dc}}{\hat{v}_g}\right)_{\hat{\omega}_e=0} = \frac{1}{s^2 CL'_g + sCR'_g + 1} \tag{3.41}$$

$$G_{vd}(s) = \left(\frac{\hat{v}_{dc}}{\hat{\omega}_e}\right)_{\hat{v}_g=0} = \underbrace{\left(\frac{2}{\pi}\frac{M_a}{P}\frac{T^q_{em}}{V_s} - \frac{I_{dc}V_n}{\omega_n V_s}\right)}_{K_{vd}} \frac{sL'_g + R'_g}{s^2 CL'_g + sCR'_g + 1} \tag{3.42}$$

where K_{vd} denotes a gain related to the operating point of the system.

3.2 Stability analysis

In previous section a linear system model was derived and two transfer functions were obtained. In this section, the obtained transfer functions are used to analyse stability margins of the system for different DC link capacitances with and without sampling delay. It will be shown that delay affects the system considerably, but to understand the influence of a delay the ideal system without a delay is considered first. Finally, the stability is examined for larger grid side inductance. The variables used for the analysis are shown in table 3.2.

Parameters		
Mains resistance	R_g	0.5 Ω
Mains inductance	L_g	0.1 mH and 1 mH
DC link capacitance	C	500 μF and 5 μF

Table 3.2: *Model parameters.*

System without delay

In general, the closed loop system is determined by a plant $G(s)$ and a feedback loop $H(s)$ using the following relationship, [22]:

$$T(s) = \frac{G(s)}{1 + G(s)H(s)} \tag{3.43}$$

The ideal system has a unity feedback loop, $H = 1$. Plotting the poles of G_{vg} from (3.41) for different values of C shows that the converter never becomes unstable for different values of C, fig. 3.6. C only affects the damping of the system which increases as C increases.

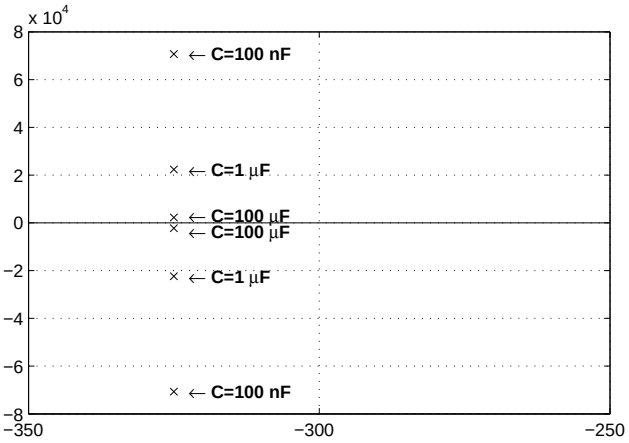

Figure 3.6: *Converter poles for different values of C.*

When analysing G_{vd} from (3.42), K_{vd} has to be evaluated as well:

$$K_{vd} = \frac{1}{V_s}\left(\frac{2}{\pi}\frac{M_a}{P}T_{em}^q - \frac{I_{dc}V_n}{\omega_n}\right) \tag{3.44}$$

The relationship between K_{vd} and T_{em} is plotted for the desired operating range, $T_{em} = [0, 20]\ Nm$ and $n = [0, 1430]\ rpm$, using results from simulation, fig. 3.7.

The relationship is linear and always positive except when T_{em} is very close to zero. It is assumed that the load is at least large enough for K_{vd} to be always positive. The stability of $G_{vd}(s)$ is therefore only evaluated for positive K_{vd}.

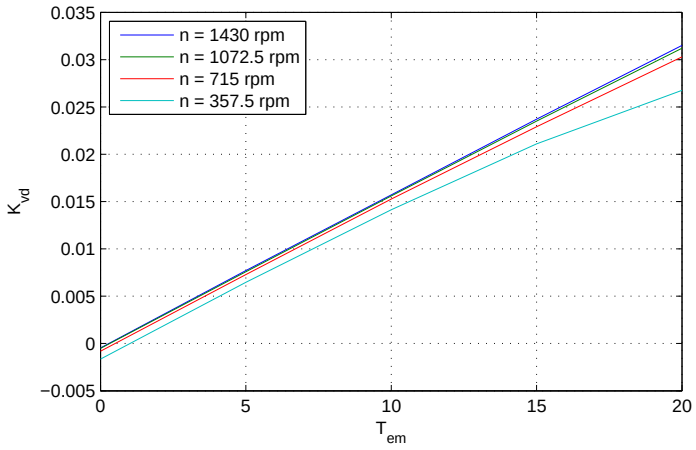

Figure 3.7: *K_{vd} as a function T_{em}.*

Two root locus diagrams are plotted to show the effect of C on K_{vd}, fig.s 3.8 and 3.9. The value of C has large influence on the damping of the system but the real parts of the poles are unchanged and therefore the stability of the system is not affected. It can be concluded that the DC link capacitor does not affect stability in the ideal system.

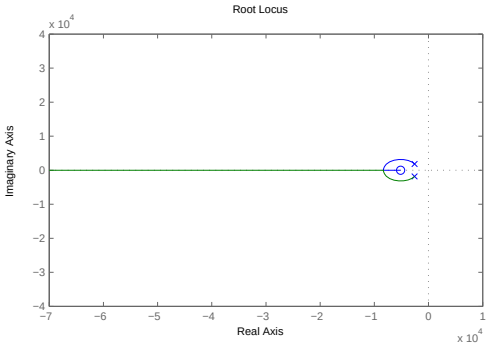

Figure 3.8: *Root locus of G_{vd} with $C = 500\ \mu F$ and $L_g = 0.1\ mH$.*

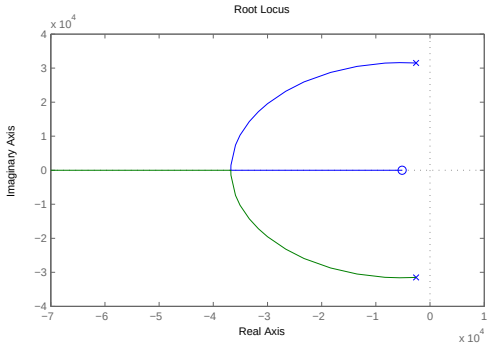

Figure 3.9: *Root locus of G_{vd} with $C = 5\ \mu F$ and $L_g = 0.1\ mH$.*

System with delay

But now a sampling delay is included in the feedback loop. The transfer function for a sampling delay and the value of T_d were explained in section 2.2.

$$H(s) = \frac{1 - (T_d s/2) + (T_d s)^2/12}{1 + (T_d s/2) + (T_d s)^2/12} \tag{3.45}$$

The sampling delay was found to be $T_d = 5 \cdot 10^{-4}\ sec$.

The system transfer functions are then:

$$H(s)G_{vg}(s) = \frac{\frac{T_d^2}{48}s^2 - \frac{T_d}{2}s + 1}{CL'_g\frac{T_d^2}{48}s^4 + \left(CL'_g\frac{T_d}{2} + CR'_g\frac{T_d^2}{48}\right)s^3 + \left(CL'_g + CR'_g\frac{T_d}{2} + \frac{T_d^2}{48}\right)s^2 + \left(CR'_g + \frac{T_d}{2}\right)s + 1} \tag{3.46}$$

$$H(s)G_{vd}(s) = \frac{L'_g\frac{T_d^2}{48}s^3 + \left(R'_g\frac{T_d^2}{48} - L'_g\frac{T_d}{2}\right)s^2 + \left(L'_g - R'_g\frac{T_d}{2}\right)s + R'_g}{CL'_g\frac{T_d^2}{48}s^4 + \left(CL'_g\frac{T_d}{2} + CR'_g\frac{T_d^2}{48}\right)s^3 + \left(CL'_g + CR'_g\frac{T_d}{2} + \frac{T_d^2}{48}\right)s^2 + \left(CR'_g + \frac{T_d}{2}\right)s + 1} \tag{3.47}$$

Fig.s 3.10 and 3.11 show the pole-zero plots of HG_{vg}. As before C has influence on the damping of the system but does not affect stability.

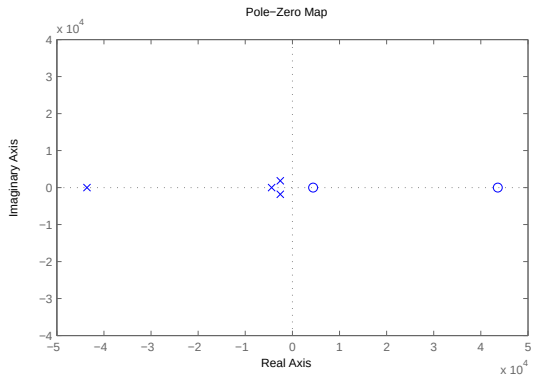

Figure 3.10: *Pole-zero plot of HG_{vg} with $C = 500\ \mu F$ and $L_g = 0.1\ mH$.*

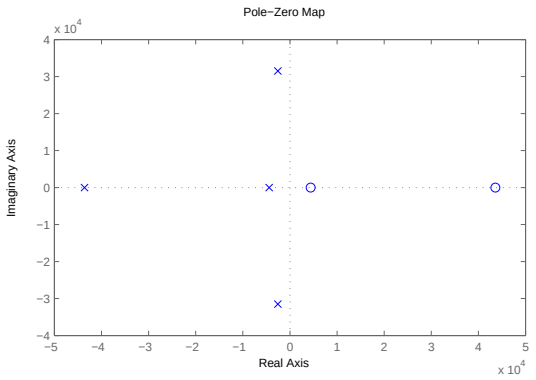

Figure 3.11: *Pole-zero plot of HG_{vg} with $C = 5\ \mu F$ and $L_g = 0.1\ mH$.*

The root-locus diagrams of HG_{vd} in fig.s 3.12 and 3.13 show that both systems become unstable when K_{vd} reaches certain value.

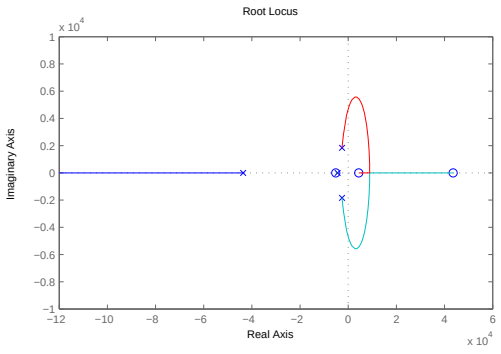

Figure 3.12: *Root locus of HG_{vd} with $C = 500\ \mu F$ and $L_g = 0.1\ mH$.*

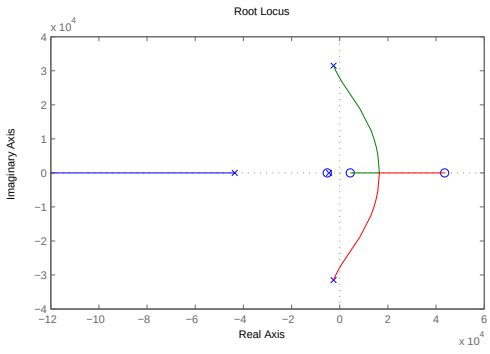

Figure 3.13: *Root locus of HG_{vd} with $C = 5\ \mu F$ and $L_g = 0.1\ mH$.*

But closer look on the root locus diagrams show that the system is marginally stable when $K_{vd} = 1.92$ for $C = 500\ \mu F$ and when $K_{vd} = 0.0468$ for $C = 5\ \mu F$, fig.s 3.14 and 3.15. It is experienced that much higher K_{vd} is needed to drive the system towards instability for a larger C.

But it is also noticed by examining the range of K_{vd} within the operating range from fig. 3.7, that the unstable region is outside the desired operating range for both $C = 500\ \mu F$ and $C = 5\ \mu F$. Therefore no unstable conditions in the converter should be encountered within the operating range for these parameters.

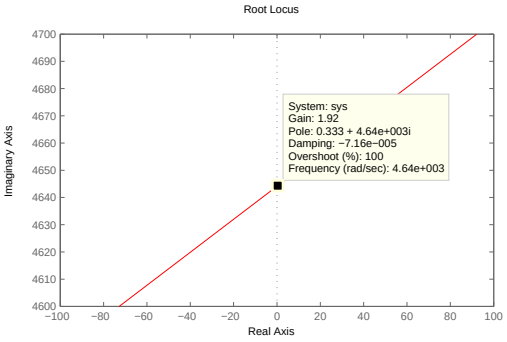

Figure 3.14: *Zoom on root locus of HG_{vd} with $C = 500\ \mu F$ and $L_g = 0.1\ mH$.*

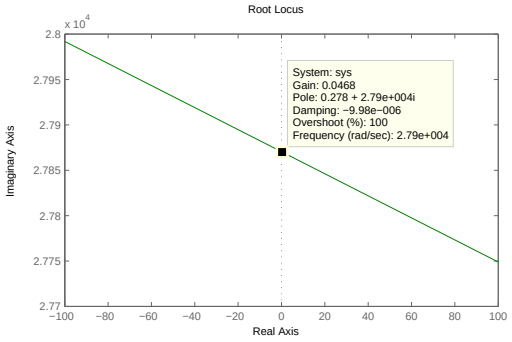

Figure 3.15: *Zoom on root locus of HG_{vd} with $C = 5\ \mu F$ and $L_g = 0.1\ mH$.*

Increasing the grid side inductance

If the grid side inductance is increased to $L_g = 1\ mH$, the poles move closer to the origin, fig.s 3.16 and 3.17.

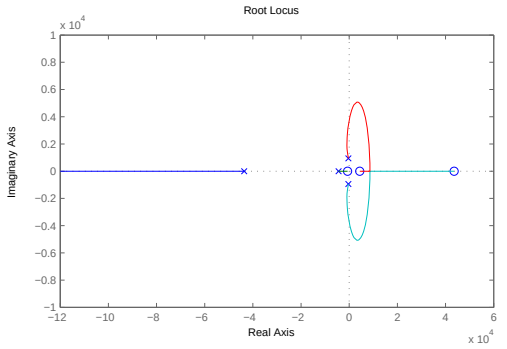

Figure 3.16: *Root locus of HG_{vd} with $C = 500\ \mu F$ and $L_g = 1\ mH$.*

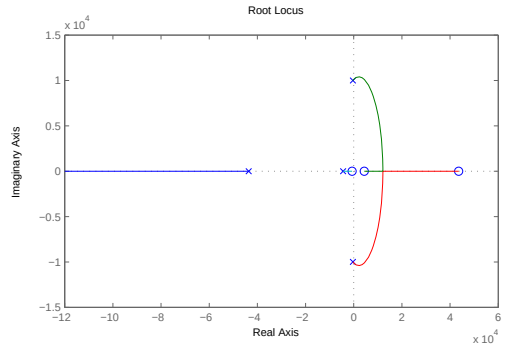

Figure 3.17: *Root locus of HG_{vd} with $C = 5\ \mu F$ and $L_g = 1\ mH$.*

For $C = 500\ \mu F$ the system is still always stable within the operating range where the system is marginally stable for $K_{vd} = 1.74$, fig. 3.18. But for $C = 5\ \mu F$ the system is marginally stable for $K_{vd} = 0.00338$ which is unstable within large area of the operating range, fig. 3.19. In fact, the system always becomes unstable within the operating range even when unloaded. This will be examined with simulation in section 3.4. The unstable condition occurs because whenever the SCIM goes from standstill to some certain speed the electromagnetic torque increases which increases the gain K_{vd} and pushes the poles to the right half plane. Despite the fact that the torque settles rather quickly to value very close to zero it is enough to cause highly unstable fluctuations in the DC link voltage where the converter is a much faster system than the SCIM.

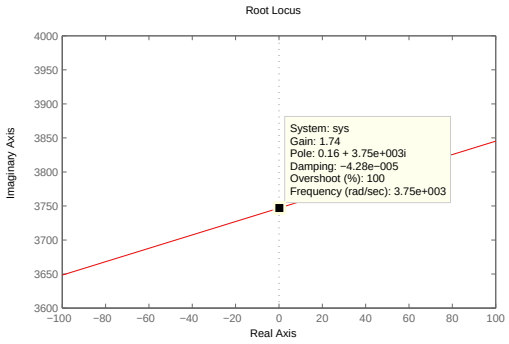

Figure 3.18: *Zoom on root locus of HG_{vd} with $C = 500\ \mu F$ and $L_g = 1\ mH$.*

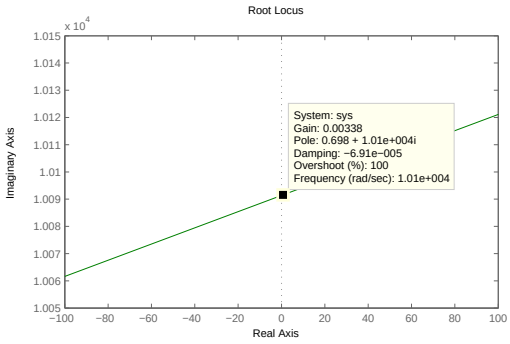

Figure 3.19: *Zoom on root locus of HG_{vd} with $C = 5\ \mu F$ and $L_g = 1\ mH$.*

3.3 Dimensioning the DC link capacitor

As explained in last section the stability of the system is not affected by the DC link capacitor given that the system is operated within the desired operating range, . But still there are requirements for dimensioning the capacitor.

The natural frequency and damping factor of G_{vg} and G_{vd}, from (3.41) and (3.42) are:

$$\omega_n = \frac{1}{\sqrt{L'_g C}} \qquad \xi = \frac{1}{2\omega_n}\frac{R'_g}{L'_g} = \frac{R'_g}{2}\sqrt{\frac{C}{L'_g}} \tag{3.48}$$

where $L'_g = 2L_g$, L_g being the grid side inductance.

The DC link voltage generated by the three phase diode rectifier may contain DC and even triplen harmonics, $6\omega_g$, $12\omega_g$, $18\omega_g$,..., [2]. The capacitor should therefore be selected to not resonate with these harmonics and especially with $6\omega_g$. This defines the upper margin of the DC link capacitor:

$$C < \frac{1}{(6\omega_g)^2 L'_g} \tag{3.49}$$

Here, L'_g is not known exactly and has to be estimated. If the grid side inductance L_g is estimated to be between 1 mH and 0.1 mH, that is $0.2 \cdot 10^{-3} < L'_g < 2 \cdot 10^{-3}$, then the lowest upper margin of the capacitor for a grid side frequency $\omega_g = 2\pi \cdot 50\ rad/s$, is:

$$C_{max} = 140\ \mu F \tag{3.50}$$

For the lower margin, the capacitor should be large enough in order not to resonate with the switching harmonics, which would allow switching harmonics to propagate to the grid side, [5]. This defines the lower margin of the DC link capacitor:

$$C > \frac{1}{(\omega_{sw})^2 L'_g} \tag{3.51}$$

The lower limit depends on the switching frequency and can therefore be chosen to some extent. The frequency converter received from Danfoss included a DC link capacitance of $C = 5\ \mu F$. The highest resonance frequency is then $f_{res} = 5\ kHz$. It is therefore necessary to select the switching

frequency so that it does not create switching harmonics in the vicinity of f_{res}.

According to [1], the switching harmonics are determined by the modulation frequency, defined as:

$$m_f = \frac{f_{sw}}{f_1} \tag{3.52}$$

f_1 being the fundamental frequency of the inverter output voltage.

Theoretically, the voltage harmonics should occur at multiples of m_f or as sidebands of lower amplitude, centered at multiples of m_f:

$$f_h = (lm_f \pm k)f_1 = lf_{sw} \pm kf_1 \tag{3.53}$$

where l defines the multiple of m_f and k the sideband.

So the switching harmonics normally occur at the switching frequency and at sidebands located at frequencies $\pm kf_1$ from the switching frequency.

If the switching frequency is selected as $f_{sw} = 6\ kHz$ then the switching harmonics will occur at frequencies much higher than f_{res} or be of such a low magnitude that they cause negliable effect. For a DC link capacitance of $C = 5\ \mu F$ and a grid side inductance in the range of $0.1 \cdot 10^{-3} < L_g < 1 \cdot 10^{-3}$, the switching frequency is selected to be $f_{sw} = 6\ kHz$.

This will give damping in the range of $0.03 < \xi < 0.1$ so large fluctuations in the DC link voltage are expected.

3.4 Simulations

Having determined the size of the DC link capacitor and the switching frequency, the system is simulated to see the intensity of the fluctuations in the DC link. The system is simulated in Matlab/Simulink 7.4.0 (R2007a) with the frequency converter and SCIM modeled using PLECS v2.0.2.

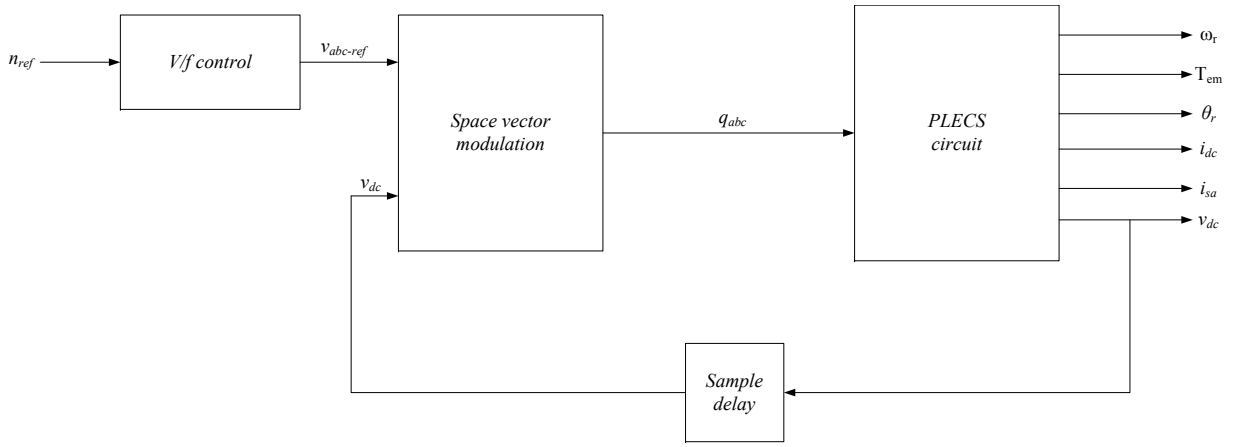

Figure 3.20: *System model.*

A block diagram of the simulation setup is shown in fig. 3.20. The SVM has the DC link voltage as input and therefore one sample delay occurs of $T_d = 0.5\ ms$ as shown in fig. 3.20. The simulation is performed in continuous time.

Description of notations used during the simulations are shown in fig. 3.21.

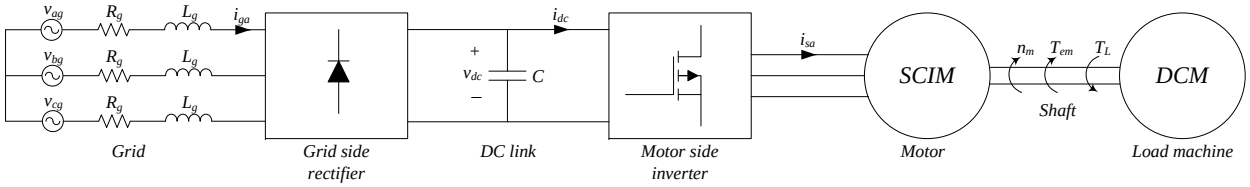

Figure 3.21: *Diagram to explain notation for different measurements.*

Four cases are studied. The first and second cases compare the frequency converter considered in the project and the frequency converter used in the implementation for both impractical and practial conditions. The converter used in the implementation was obtained from Danfoss and is a modified version of one of their drives with small DC link capacitor. The configuration used in the Danfoss VLT drive is shown in fig. 3.22 where the conventional DC link capacitor is in parallel with a diode in series with another capacitor. The conventional DC link capacitor is a series connection of two 10 μF capacitors to withstand higher voltage. The extra capacitors are two 150 μF electrolytic capacitors in series.

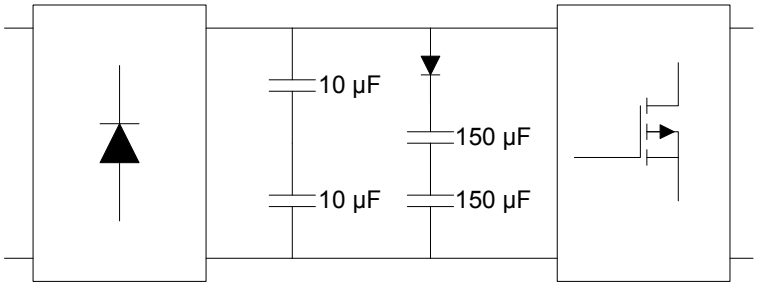

Figure 3.22: *DC link configuration of Danfoss VLT.*

Case 1 will look at instability in the SCIM and compare the results for the converters used in the project and the Danfoss drive. The simulations in Case 1 are performed first for a constant speed $n_n/2$ and no load. Then a load step is applied from no load to $T_n/2$ at speed $n_n/2$.

Case 2 will compare the drive configurations for more practical situation and show how the Danfoss drive allows higher degree of dynamics in the system. The simulations in Case 2 are performed first for a step in speed from $n_n/2$ to n_n at $T_n/2$ load and then for a load step from $T_n/2$ to T_n at n_n speed.

Case 3 attempts to make the system unstable by applying a load step outside the operating range that should give an unstable condition according to the stability analysis.

Case 4 attempts to make the system unstable by increasing L_g which should create an unstable condition according to stability analysis.

The parameters generally used in the simulations are shown in table 3.3.

Parameters		
Mains input voltage	V_{in}	$230\sqrt{2}\ V_{peak}$
Mains resistance	R_g	0.5 Ω
Mains inductance	L_g	0.1 mH
DC link capacitance	C	5 μF
Stator resistance	r_s	1.79 Ω
Stator leakage inductance	L_{ls}	7 mH
Mutual inductance	L_m	0.158 H
Rotor resistance	r_r	1.8 Ω
Rotor leakage inductance	L_{lr}	0.0144 H
Pole pairs	P	2
Motor shaft inertia	J	9.57 mNm^2
Sample delay	T_d	0.5 ms
Switching frequency	f_{sw}	6 kHz
Motor nameplate		
Nominal power	P_n	3.0 kW
Nominal phase voltage	V_n	$380/\sqrt{3}\ V_{rms}$
Nominal current	I_n	6.9 A_{rms}
Nominal frequency	f_n	50 Hz
Nominal power factor	PF	0.77
Nominal speed	n_n	1430 rpm
Nominal torque	T_n	20 Nm

Table 3.3: *Model parameters.*

Case 1a: Frequency converter in project - Impractical condition

At no-load, an instability in the SCIM is encountered. Very high fluctuations are experienced in v_{dc} that reach values up to 2 kV. The high oscillations in v_{dc} are caused by i_{dc} that changes erratically from positive to negative values.

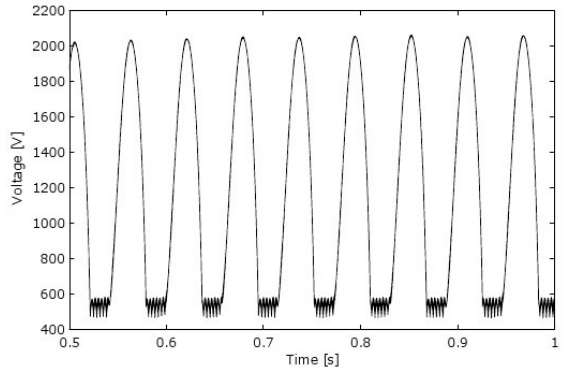

Figure 3.23: *DC link voltage at $n_n/2$ speed and no load.*

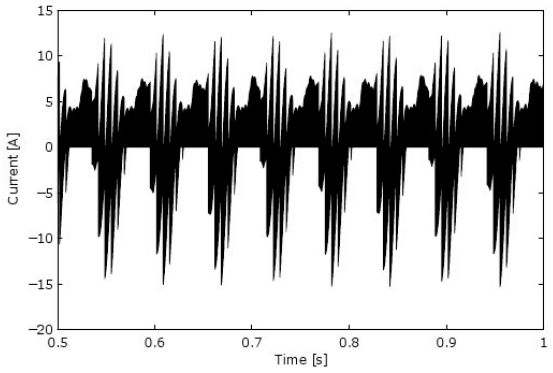

Figure 3.24: *DC link current at $n_n/2$ speed and no load.*

Looking at the stator current i_{sa} in fig. 3.25 it can be seen that the SCIM does not have a fixed amplitude which is referred to as an unstable condition where the system suffers from sustained

oscilliations, [23]. This situation is addressed as being often experienced in a lightly loaded V/Hz PWM controlled induction motors, [23] [24] [25]. This instability was not predicted by the stability analysis and could be related to the term that was omitted in the linearized model where it was dominated by the SCIM. In [24] this unstable behavior is blamed on the stator resistance and is therefore caused by the SCIM which was not part of the stability analysis.

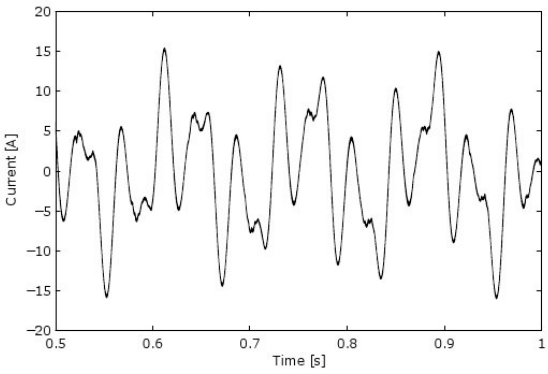

Figure 3.25: *Stator current at $n_n/2$ speed and no load.*

The sustained oscilliations can well be seen in fig.s 3.26 and 3.27 where the rotor speed n_m and the electromagnetic torque T_{em} oscilliate heavily in steady state.

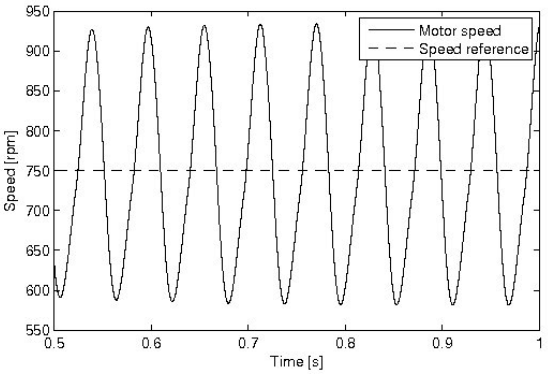

Figure 3.26: *Rotor speed at $n_n/2$ speed and no load.*

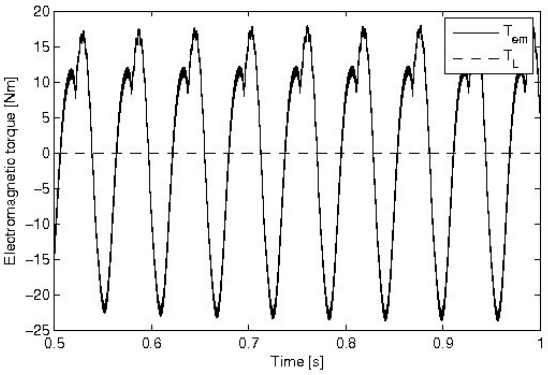

Figure 3.27: *Electromagnetic torque at $n_n/2$ speed and no load.*

But as soon as a load step is applied the oscilliations are damped and the SCIM becomes stable. The oscilliations in v_{dc} decrease to expected variations for a given small DC link capacitor, fig. 3.28. Looking closer at v_{dc}, around 3 periods can be seen during time $\Delta t = 5 \cdot 10^{-4}$ s which shows that v_{dc} contains harmonics caused by the switching frequency, fig. 3.29.

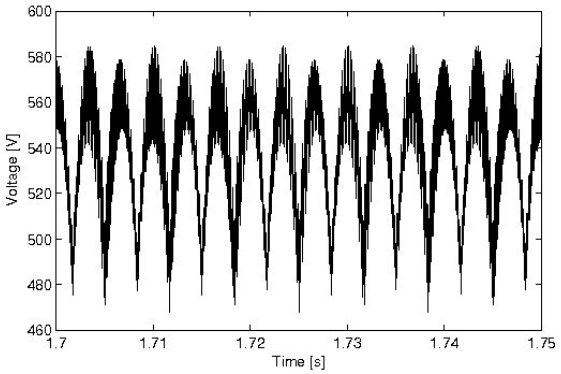

Figure 3.28: *DC link voltage after load step at n_n speed.*

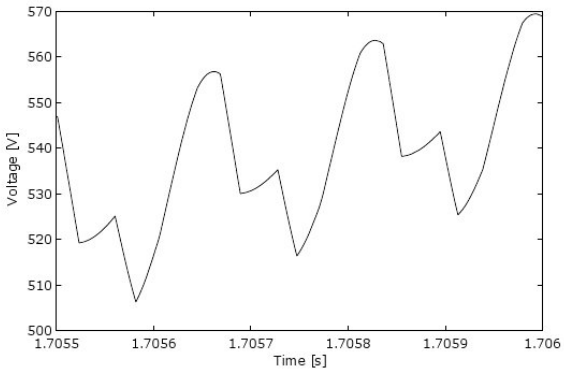

Figure 3.29: *Zoom on DC link voltage after load step at $n_n/2$ speed.*

Fig.s 3.30 and 3.31 show that the currents now have fixed amplitude after the load step has been applied. This is described as a stable condition for the SCIM in [23].

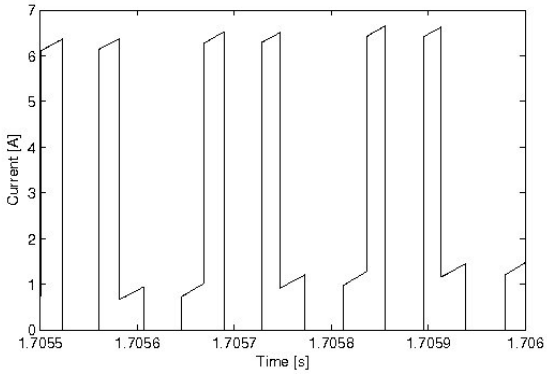

Figure 3.30: *DC link current for load step at $n_n/2$ speed.*

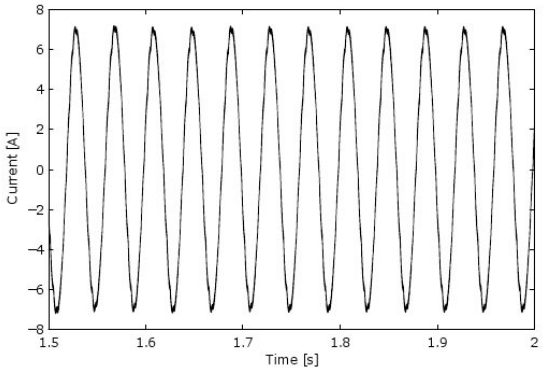

Figure 3.31: *Stator current for load step at $n_n/2$ speed.*

And from fig.s 3.32 and 3.33 it can be seen that the system stabilizes with the load step as the fluctuations in n_m and T_{em} decrease after the load step is applied.

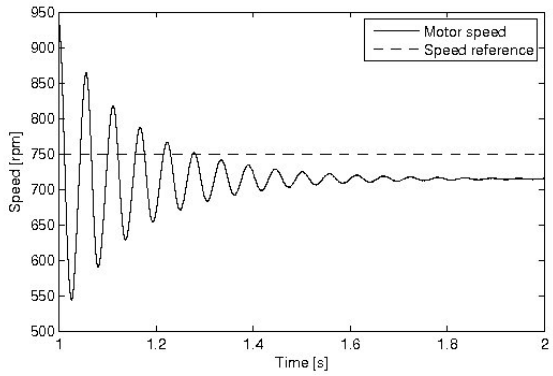

Figure 3.32: *Rotor speed for load step at $n_n/2$ speed.*

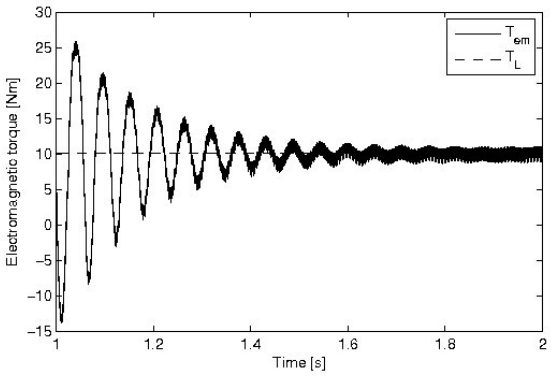

Figure 3.33: *Electromagnetic torque for load step at $n_n/2$ speed.*

Case 1b: Frequency converter from Danfoss - Impractical condition

Now using the same conditions for the Danfoss drive, v_{dc} is clamped by the extra capacitor bank. But as the charge increases over the extra capacitor bank, the voltage increases, fig. 3.34. i_{dc} also increases as the extra capacitor bank charges, fig. 3.35. The configuration can therefore not limit the sustained voltage fluctuations over a long time, it rather works as a safety which slowly breaks.

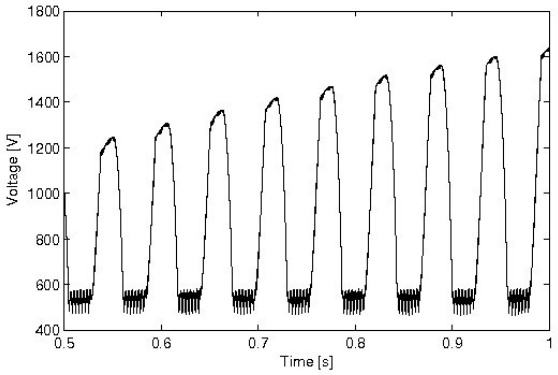

Figure 3.34: *Danfoss drive. DC link voltage at $n_n/2$ with no load.*

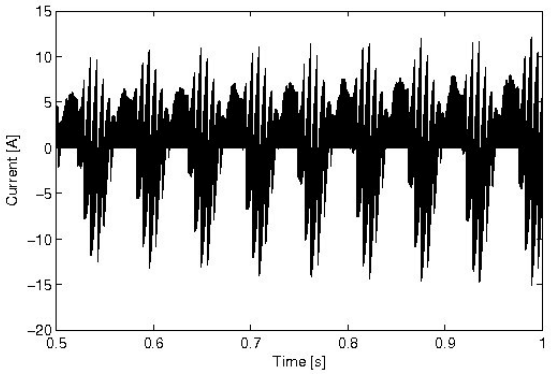

Figure 3.35: *Danfoss drive. DC link current at $n_n/2$ with no load.*

The exact same instability behavior in i_{sa} is experienced as in Case 1 and it can also be seen how the fluctuations in n_m and T_{em} are highly linked to v_{dc} where they increase as the fluctuations in v_{dc} increases, fig.s 3.36 and 3.37.

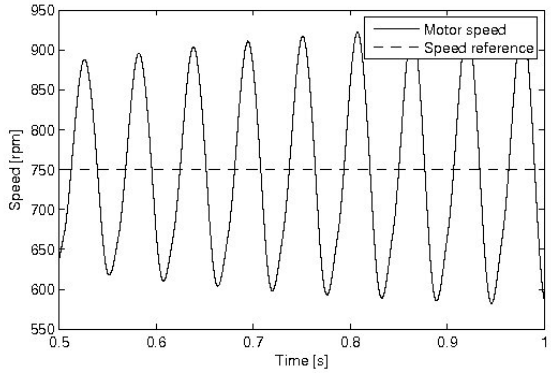

Figure 3.36: *Danfoss drive. Rotor speed at $n_n/2$ with no load.*

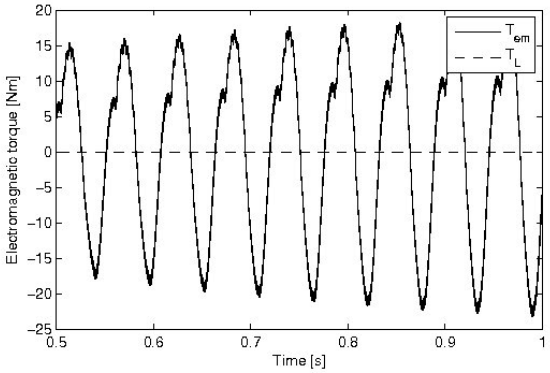

Figure 3.37: *Danfoss drive. Electromagnetic torque at $n_n/2$ with no load.*

But as a load step is applied the same situation as in Case 1a is experienced. The SCIM becomes stable and the oscillations decrease. But the ripples in v_{dc} are still considerable because of the small DC link capacitor, fig. 3.38. The DC link configuration of the Danfoss drive can only help if large oscillations in v_{dc} are experienced over a short period. Else the same situation is experienced as in Case 1a.

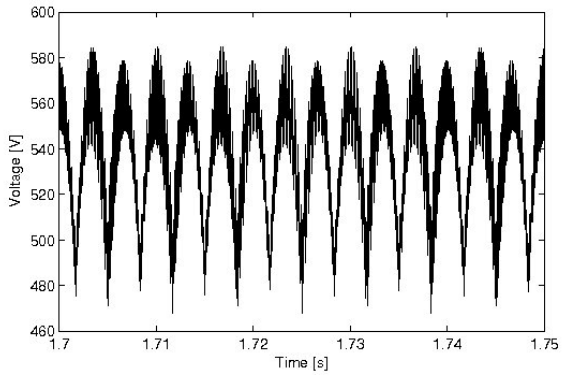

Figure 3.38: *Danfoss drive. DC link voltage at $n_n/2$ with $T_n/2$ load.*

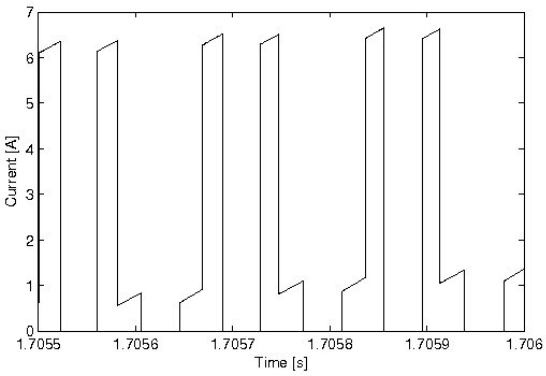

Figure 3.39: *Danfoss drive. DC link current at $n_n/2$ with $T_n/2$ load.*

Case 2a: Frequency converter in project - Practical condition

This case aimes at a more practical condition where simulations are performed for a stable SCIM. At the time of speed change a large overvoltage is observed in v_{dc}, fig. 3.40. This is due to the small DC link capacitor that does not provide enough damping of the voltage. For this kind of overvoltage the inverter would normally trip so care has to be taken in implementation to not apply quick speed changes. Closer look on v_{dc} shows that it contains both harmonics due to the diode rectifier and switching harmonics, fig. 3.41.

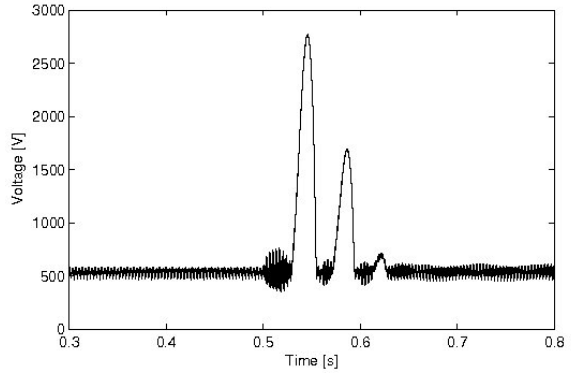

Figure 3.40: *DC link voltage for speed step at $T_n/2$ load.*

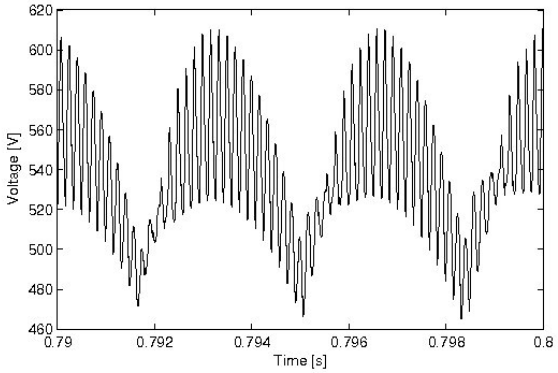

Figure 3.41: *Zoom on DC link voltage after speed step.*

The large overvoltage in v_{dc} is caused by large fluctuations in i_{dc}, fig. 3.42, and consequently in i_s, 3.43, which are affected by the large fluctuations in T_{em} due to the speed step, 3.45.

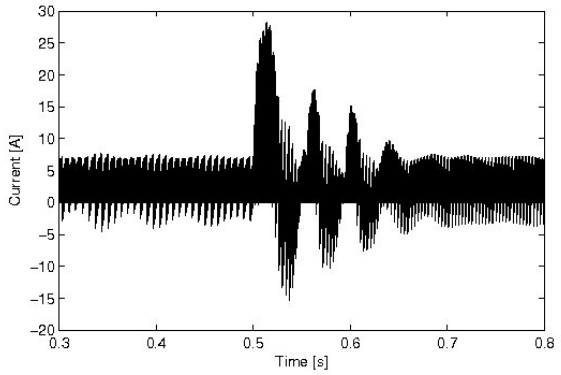

Figure 3.42: *DC link current for speed step at $T_n/2$ load.*

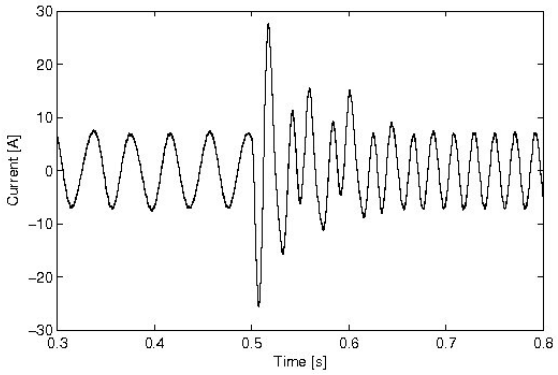

Figure 3.43: *Stator current for speed step at $T_n/2$ load.*

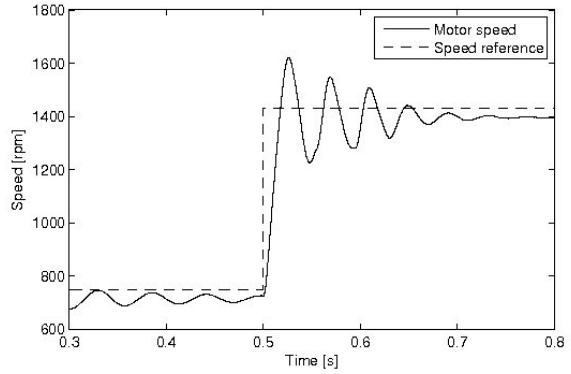

Figure 3.44: *Rotor speed for speed step at $T_n/2$ load.*

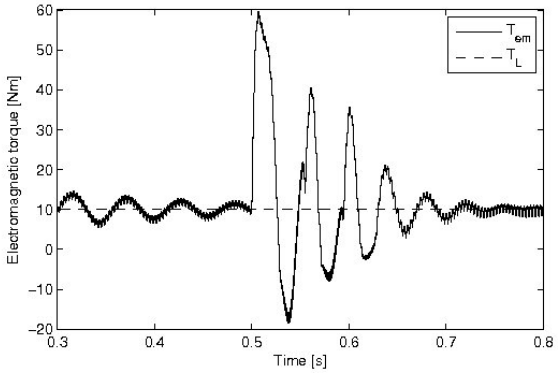

Figure 3.45: *Electromagnetic torque for speed step at $T_n/2$ load.*

Applying a load step does not affect v_{dc} and i_{dc} in the same way as a speed step. No large overvoltages or overcurrents are experienced in v_{dc} and i_{dc}, fig.s 3.46 and 3.48. Looking closer on v_{dc} shows that the amplitude of switching harmonics are increased because a larger current is being switched by the inverter, fig. 3.47.

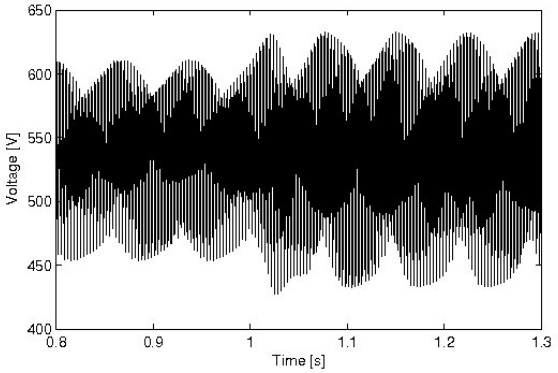

Figure 3.46: *DC link voltage for load step at n_n speed.*

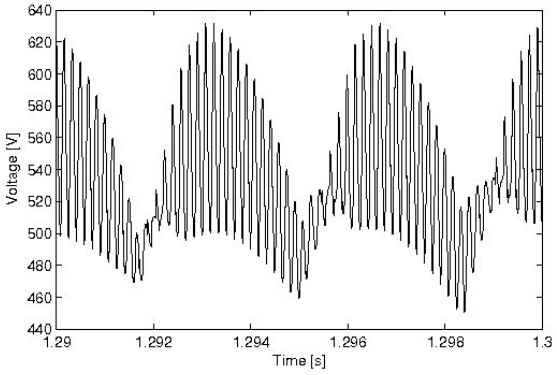

Figure 3.47: *Zoom on DC link voltage after load step.*

The transition to a higher load is rather smooth and does not cause large overshoot in T_{em} compared to the overshoot experienced for a speed step.

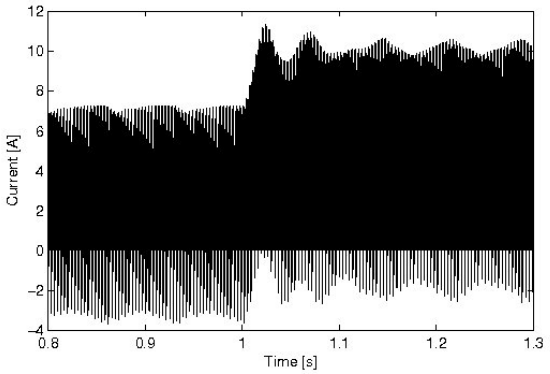

Figure 3.48: *DC link current for load step at n_n speed.*

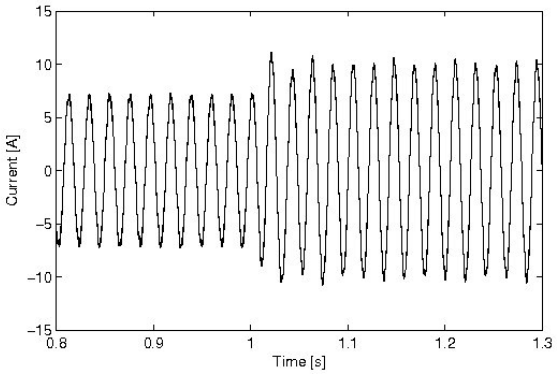

Figure 3.49: *Stator current for load step at n_n speed.*

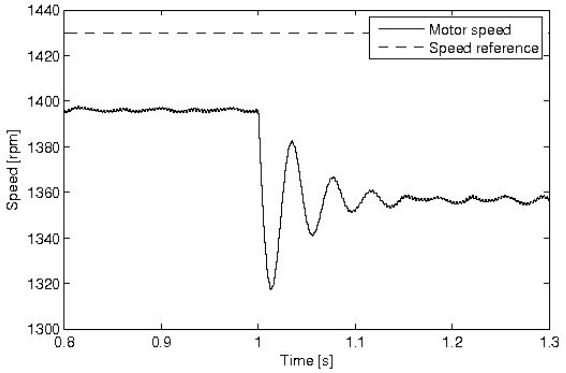

Figure 3.50: *Rotor speed for load step at n_n speed.*

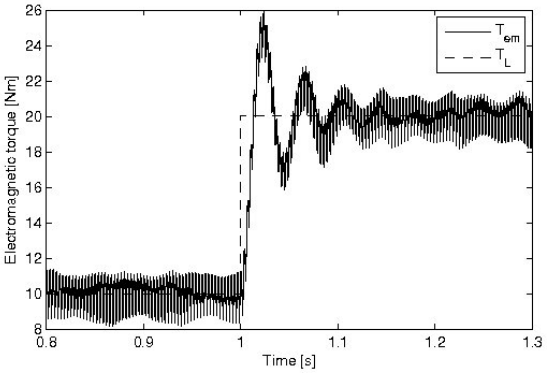

Figure 3.51: *Electromagnetic torque for load step at n_n speed.*

Case 2b: Frequency converter from Danfoss - Practical condition

For a stable SCIM the extra capacitor bank provides extra damping as seen from fig. 3.52, where the fluctuations in v_{dc} are not as dramatic as in Case 2a. This DC link configuration should therefore allow larger changes in speed compared to the configuration used in Case 2a. Looking closer at v_{dc} the DC link configuration does not seem to offer more filtering of switching harmonics than the configuration in Case 1, fig. 3.53.

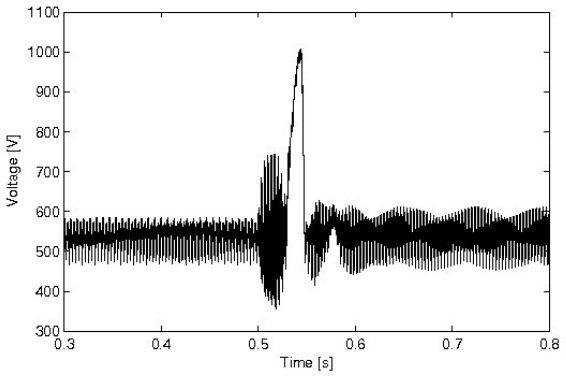

Figure 3.52: *Danfoss drive. DC link voltage for speed step at $T_n/2$ load.*

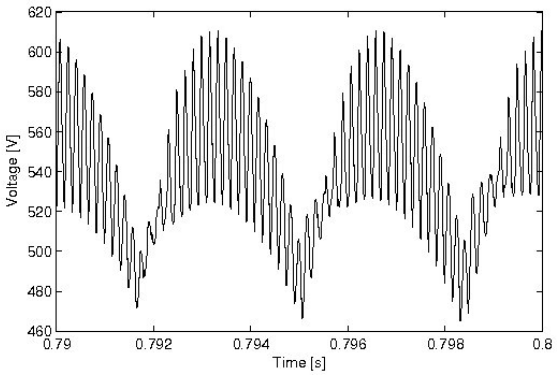

Figure 3.53: *Danfoss drive. Zoom on DC link voltage after speed step.*

But i_{dc} still jumps to a similar value as in Case 2a where the extra capacitor bank only affects v_{dc}, fig. 3.54. And the overshoot in T_{em} also occurs with the Danfoss drive, fig. 3.55.

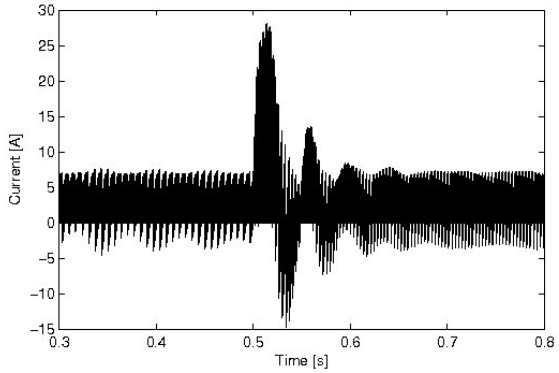

Figure 3.54: *Danfoss drive. DC link current for speed step at $T_n/2$ load.*

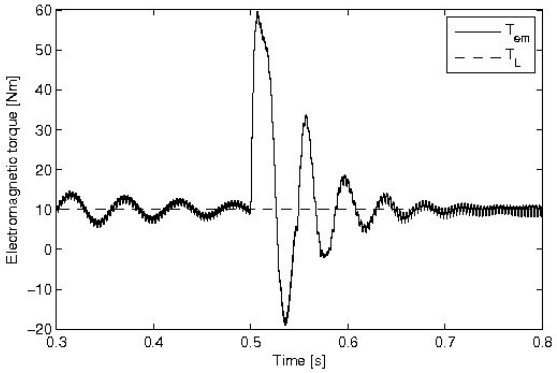

Figure 3.55: *Danfoss drive. Electromagnetic torque for speed step at $T_n/2$ load.*

The load step gives similar results as in Case 2a as the load step did not induce large fluctuations in v_{dc}.

Case 3: Attempt to create an unstable condition with load step

As was shown in fig. 3.7, the value of K_{vd} is directly proportional to the electromagnetic torque T_{em}. If the stability analysis holds, an unstable condition could be created by applying a load step large enough. This load step is outside the operating range of the system but can nevertheless be applied in simulation.

The load step applied is $T_L = 45\ Nm$ at rated speed n_n. This gives $K_{vd} = 0.067$ which should give an unstable condition according to stability analysis in section 3.2.

But after the load step is applied at $t = 0.5$ *sec.* the system is still stable as seen from v_{dc} in fig. 3.56. Due to the load step, i_{dc} increases, fig. 3.57. n_m decreases as the open loop V/f control does not compensate for the added load torque, fig.s 3.58 and 3.59.

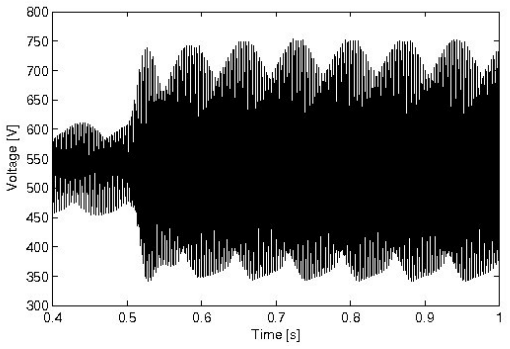

Figure 3.56: *DC link voltage for estimated unstable load step.*

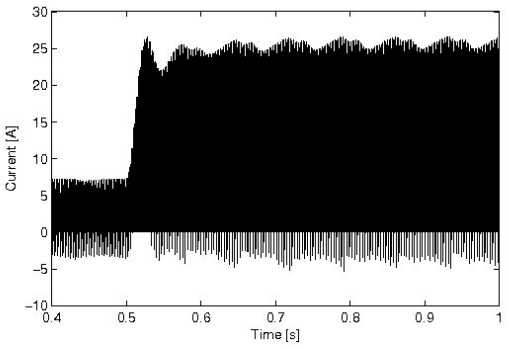

Figure 3.57: *DC link current for estimated unstable load step.*

The reason for this could be because of additional damping which is present in the nonlinear system and not included in the linearized model.

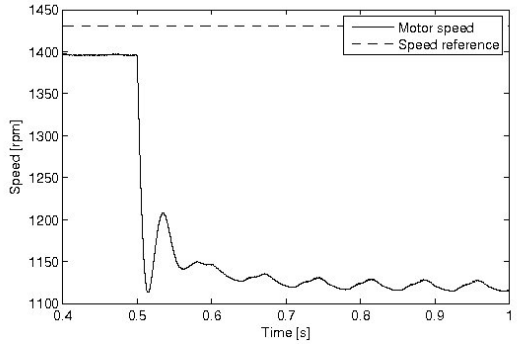

Figure 3.58: *Rotor speed for estimated unstable load step.*

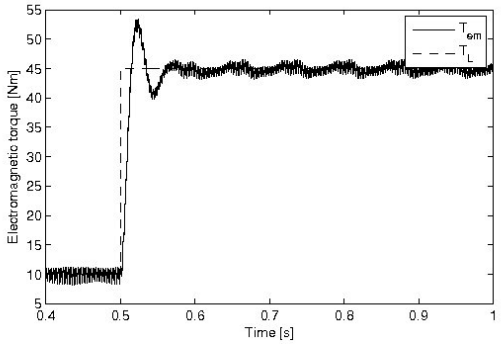

Figure 3.59: *Electromagnetic torque for estimated unstable load step.*

Case 4: Unstable condition for increased L_g

As was shown in section 3.2 the system is unstable if the grid side inductance is increased to $L_g = 1\ mH$. Running simulation with no load and rated speed results in increasing fluctuations in v_{dc} which is definately unstable for these condtions, fig. 3.60. This finally produces an error in the simulation when v_{dc} tries to go negative.

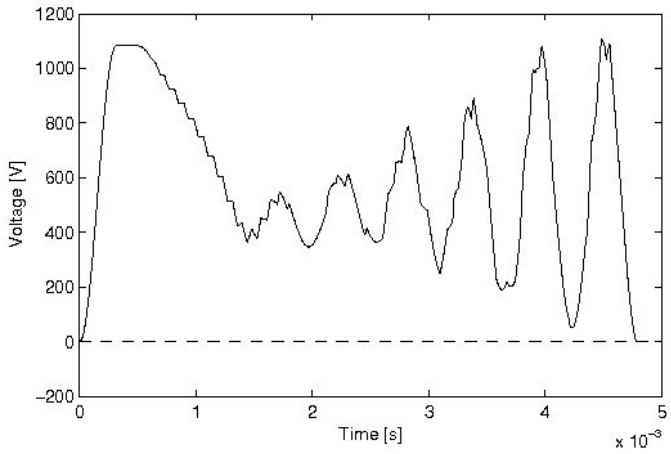

Figure 3.60: *Unstable DC link voltage for $L_g = 1\ mH$.*

As was mentioned in the section 3.2, only a little T_{em} is needed to make the system unstable and as T_{em} starts to increase, the grid side current i_{ga} starts fluctuating in an uncontrolled fashion, fig.s 3.61 and 3.62.

It can be concluded that the system is unstable for these operating conditions as was predicted by the stability analysis.

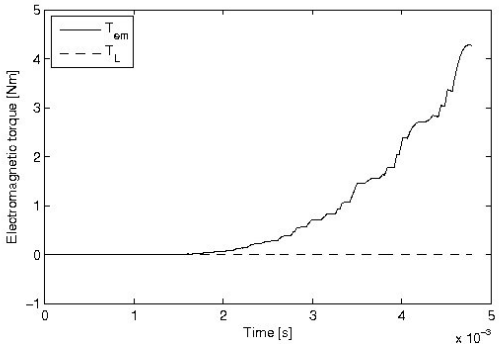

Figure 3.61: *Electromagnetic torque for unstable condition.*

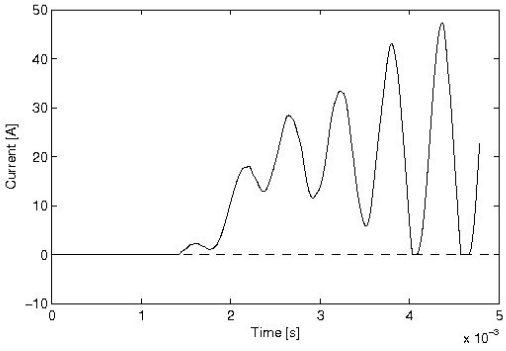

Figure 3.62: *Grid side current for unstable condition.*

3.5 Summary

Stability analysis of the system were performed in this chapter and stability margins obtained for different parameters. This involved linearization of the system and derivation of small signal models to obtain the system transfer functions. The stability of the SCIM was not the focus of this project and the corresponding term was therefore omitted.

It was shown that the system stability was affected by the DC link capacitor if a sampling delay was included in the linearized model. The system was stable within the operating range for the analysed capacitor sizes but a load step outside the operating range should give an unstable condition according to the stability analysis. This was disproven by simulation which could be because the nonlinear model contains some dampings that are not included in the linearized model.

It was also shown that the grid side parameters have large effect on system stability. The system was unstable for a DC link capacitor of 5 μF and a grid side inductance of 1 mH. This instability behavior was then tested and proven by simulation.

Chapter 4

Implementation

Description of test setup and technical information relevant for the implementation are provided in this chapter along with experimental results.

4.1 Test setup

To observe the problems arising because of the small DC link capacitor the system is implemented on a test bench. This requires a digital signal controller (DSC) to control the frequency converter using the DC link voltage as feedback. Speed reference and DC link voltage are the only variables needed to control the SCIM employing V/f control and space vector modulation. Following subsections give a small description of the components used in the test setup.

DSC

The DSC consist of a digital signal processor (DSP) and a great deal of microcontrollers that work together creating a low-cost and powerful solution for many embedded applications.

The DSC used in the project is the TMS320F2812 from Texas Instruments. It provides a high operating clock frequency of 150 MHz, 32-bit processing capabilities and a comfortable floating to fixed-point conversion through the IQ Math library which also includes dozens of arithmetic, trigonometric and numberical conversion functions, [26].

During the experimental testing, two important capabilities of the DSC are used, PWM generation and ADC conversion.

The PWM generation occurs through the use of general-purpose timers and full-compare units which are part of the event-manager modules on the DSC, [27]. There is also a possiblity for programming a deadband but it is not used where it is integrated into the Danfoss VLT. The switching frequency used is $f_{sw} = 6\ kHz$.

The analog-to-digital conversion occurs through a 12-bit pipelined analog-to-digital converter (ADC) module. The main analog ciruits in the ADC module are the front-end analog multiplexers, sample and hold circuits and the conversion core. The ADC module consists of two independent 8 channel modules which can be cascaded to form a 16 channel module. Each 8 channel module has its sperate analog multiplexer and sample and hold circuit but only one converter core is present

which serves both modules, [28].

An interface board is attached on top of the DSC to give analog input ports and LED PWM output ports. Picture of the DSC and the attached interface board is shown in fig. 4.1.

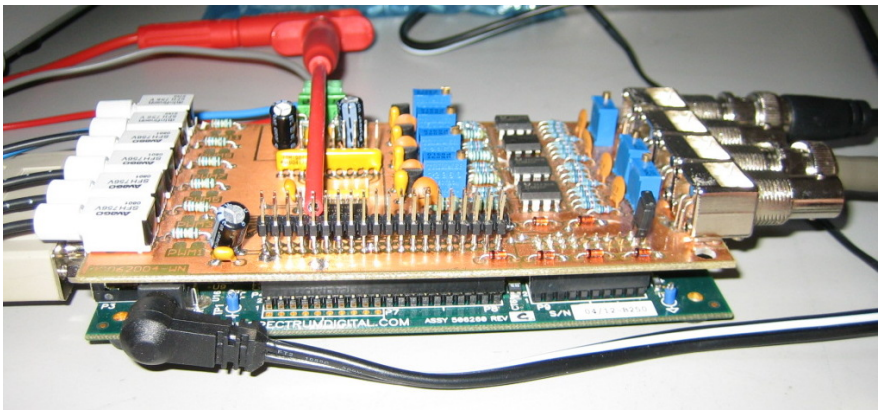

Figure 4.1: *DSC with interface board on top.*

To improve accuracy of the analog-to-digital conversion, the ADC modules are calibrated using the method described in [29]. The gain and offset errors can be described by:

$$y = x \cdot m_a + b \tag{4.1}$$

where x is the desired output count ($count = voltage \cdot 4095/3.0V$) and y is the actual output which is distorted by a gain and offset errors, m_a and b. These values can be found using:

$$m_a = \frac{y_H - y_L}{x_H - x_L} \tag{4.2}$$

$$b = y_L - x_L \cdot m_a \tag{4.3}$$

where x_H and x_L are known references for high and low inputs and y_H and y_L are the corresponding outputs from the ADC. The desired output can then be calculated by writing (4.1) in the form:

$$x = \frac{y}{m_a} - \frac{b}{m_a} \tag{4.4}$$

Code generation for DSP

Simulink models can be compiled straight to C code specially enhanced for TMS320F2812 by using Real-Time workshop and the Target for TI C2000 library in Matlab/Simulink. The Target for TI C2000 library provides a variety of blocks for Simulink which allow the user to exploit all features of the DSC. Real-Time workshop then builds a Code Composer Studio project where the code can be uploaded to the DSP and specfic variables of the model can be controlled.

Using this feature decreases considerably the time from simulation to implementation but has the drawback that the student will not be aware of all the technical details taking place inside the DSP.

Normally, before being able to build the C code, the Simulink model has to be discretized. But where no continuous states are present in the open loop V/f control and space vector modulation, this step can mostly be skipped. But one filter is needed to limit the change in reference speed.

A quick change in speed generates large overvoltages and overcurrents due to the small DC link capacitor, this can cause the frequency converter to trip. The filter is a 1st order with cutoff frequency $f_{cut} = 0.1\ Hz$. This filter is discretized using the trapezoidal method, [30]:

$$\left(\frac{1}{\frac{s}{0.2\pi}+1}\right)_{s=\frac{2}{T_s}\frac{z-1}{z+1}} = \frac{z+1}{19100z-19098} \tag{4.5}$$

where T_s is the sampling period, $T_s = (6 \cdot 10^3)^{-1}\ sec.$

A screenshot of the Simulink model to be compiled to the DSP is shown in fig. 4.2. A rate transition is needed because there is a difference in clock frequency between the "Vdc" signal and the SVM function. The "Vdc" signal is at clock frequency equal to the sampling frequency, $f_s = 6\ kHz$ while the SVM function is working at the DSP clock frequency, 150 MHz. Buffers are needed to view the signals graphically in Code Composer Studio. The variables "duty1" and "n_ref" are then the corresponding memory addresses to the data.

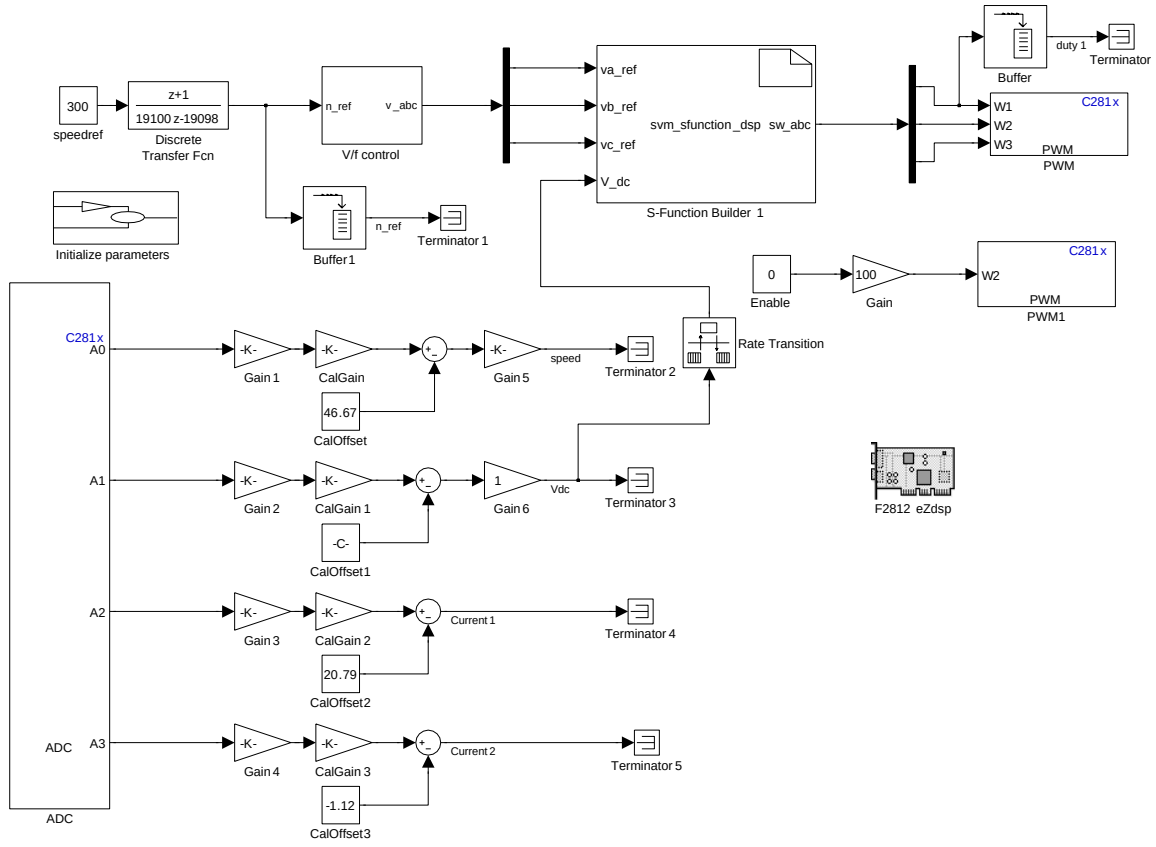

Figure 4.2: *Screenshot of Simulink model for DSP.*

SCIM

The motor in the test setup is a three phase squirrel cage induction motor from ABB motors. It has a rated input voltage of 380 V_{rms} and maximum voltage of 420 V_{rms} when Y-connected. Rated current is 6.9 A_{rms} and rated power 3 kW. Picture of the SCIM and the load machine is shown in fig. 4.3. Motor nameplate can be seen in appendix C.

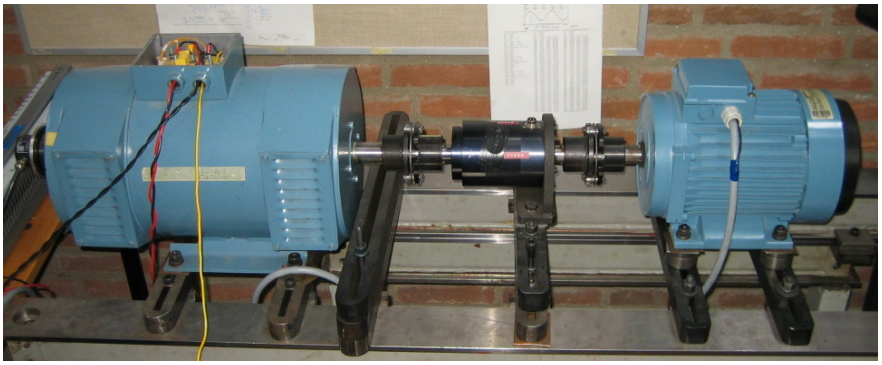

Figure 4.3: *Load machine (left) and SCIM (right) in the test setup.*

Load machine

The load machine is a 3.3 kW DC motor (DCM) from Thrige-Titan A/s. It has seperately excited field windings with nominal field current of $i_f = 0.7\ A$. Nameplate of motor can be viewed in appendix C.

In order to load the SCIM with the DCM the armature windings of the DCM have to be connected to a variable resistance while feeding the field windings with the nominal field current. Holding the field current constant ensures a constant direct axis field Φ_d and the electromechanical torque of the DCM T_{dc} is only controlled by the armature current i_{arm} as shown in (4.6), [31].

$$T_{dc} = K_a \Phi_d i_{arm} \tag{4.6}$$

where K_a is a constant determined by the design of the motor.

From the data given on the DCM, it should generate a load torque of $T_{dc} = 20\ Nm$ for $i_{arm} = 9.7\ A$ while holding $i_f = 0.7\ A$. As i_{arm} is directly proportional to T_{dc} the load torque can now be controlled with i_{arm} by varying the variable resistance. Fig. 4.4 explains the installation of the load machine.

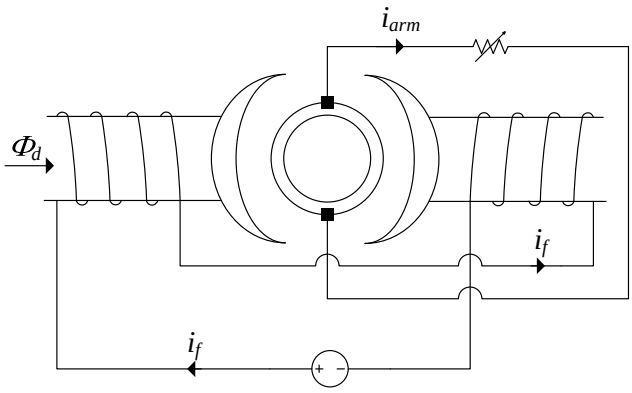

Figure 4.4: *Installation of load machine.*

Danfoss VLT

The Danfoss frequency converter used in the test setup is a modified version of the 2.2kW FC-302 VLT. The modification is associated with the DC link configuration which has been changed to

the one that was explained in fig. 3.22. The interface board attached to the VLT offers inputs for external PWM waveforms and configuration of deadband. Deadband is set to 2 μs. Picture of the VLT with attached interface board is shown in fig. 4.5.

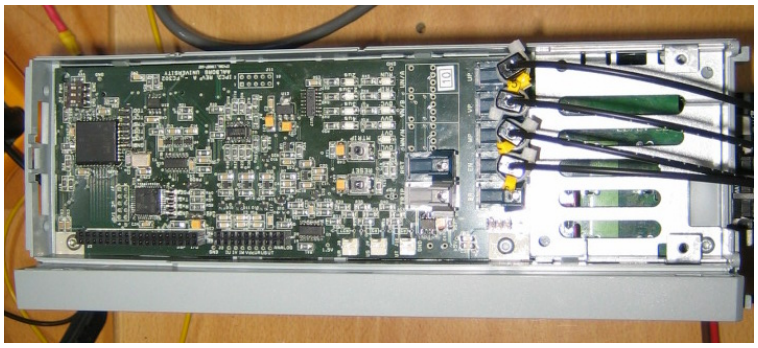

Figure 4.5: *Danfoss VLT with attached interface board.*

4.2 Experimental results

To show how a highly fluctuating feedback signal affects the systems steady state behavior, experimental tests were performed for three cases of scaling factor for the SVM, DC link voltage feedback, filtered DC link voltage feedback and no feedback where scaling factor was set as constant. In all cases, open loop V/f control was used as a speed control strategy and SVM for modulation. Fig. 4.6 explains the three different cases by block diagrams. Screenshots of plots from oscilloscopes are available in appendix B.

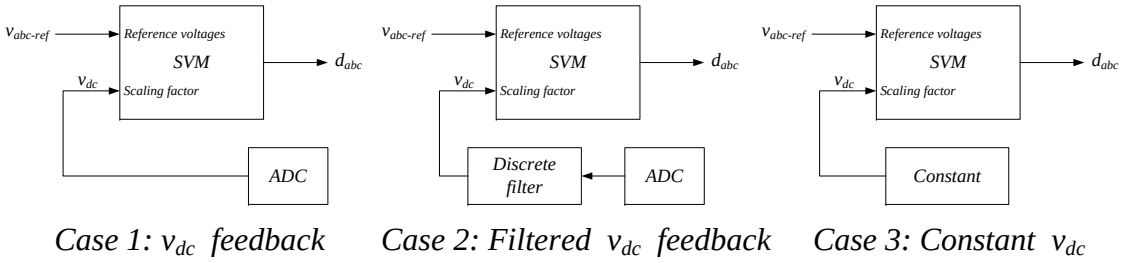

Figure 4.6: *Graphical explanation of different scaling factors for each case.*

Case 1a: v_{dc} feedback - No load

Driving the SCIM with no load at rated speed, $n_n = 1430\ rpm$ results in relatively low stator current as seen in fig. 4.8. The stator current has harmonics of 5th order that are caused by deadtime. The DC link voltage is fluctuating because of the low DC link capacitance, fig. 4.7. The instability behavior encountered in simulation in section 3.4 is not experienced in the implementation.

Looking closer on the DC link voltage, it can be seen that it contains both ripple caused by the diode rectifier and ripple caused by switching harmonics, fig.s 4.9 and 4.10.

The rotor speed contains some high frequency ripples of low amplitude but is rather constant.

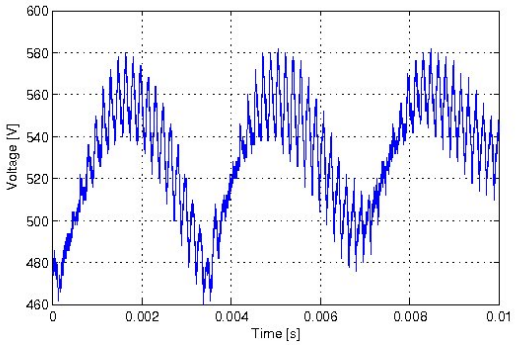

Figure 4.7: *v_{dc} feedback. DC link voltage at no load, rated speed.*

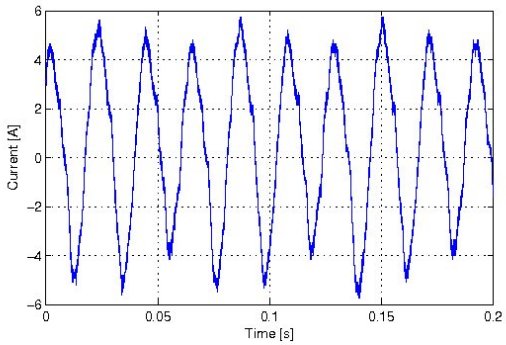

Figure 4.8: *v_{dc} feedback. Stator current at no load, rated speed.*

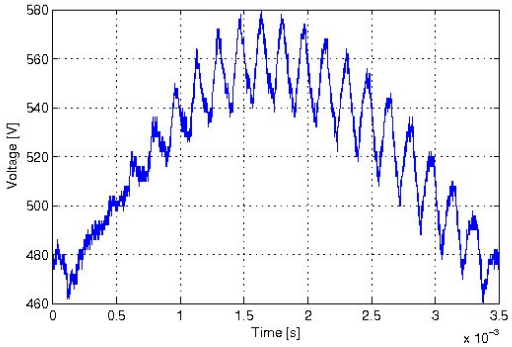

Figure 4.9: *v_{dc} feedback. Ripple caused by diode rectifier at no load, rated speed.*

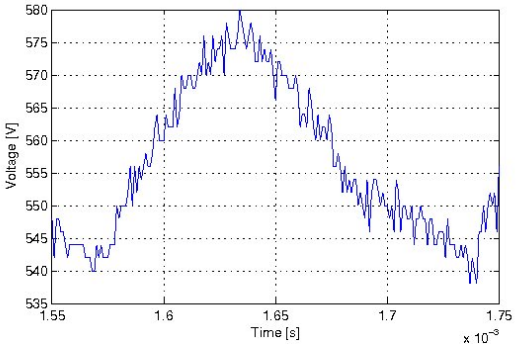

Figure 4.10: *v_{dc} feedback. Ripple caused by switching harmonics at no load, rated speed.*

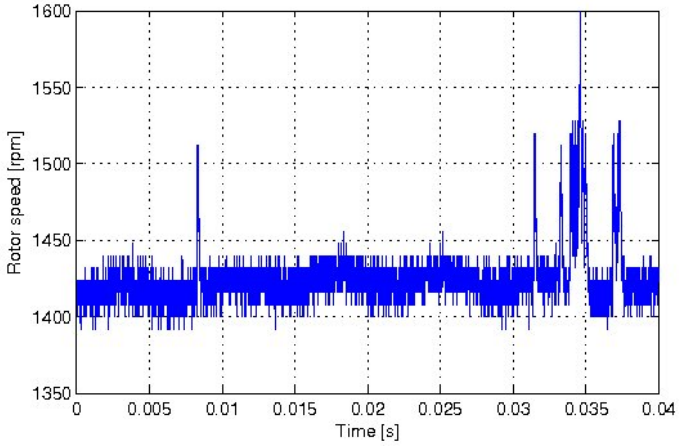

Figure 4.11: *v_{dc} feedback. Rotor speed at no load, rated speed.*

Case 1b: v_{dc} feedback - Full load

Loading the SCIM with rated load, $T_n = 20\ Nm$, increases the stator current as seen in fig. 4.13. The DC link voltage now has switching harmonics of higher amplitude as higher current is being switched by the inverter, fig. 4.12. This complies with simulations in section 3.4.

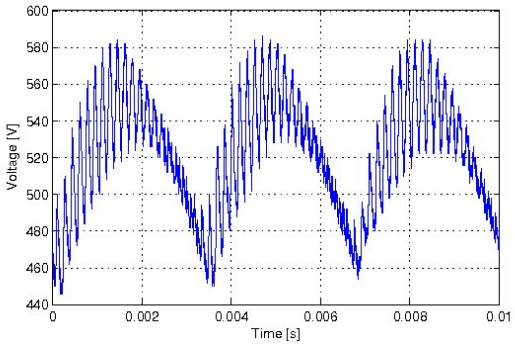

Figure 4.12: *v_{dc} feedback. DC link voltage at full load, rated speed.*

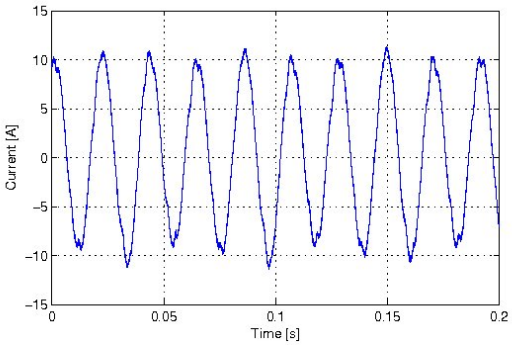

Figure 4.13: *v_{dc} feedback. Stator current at full load, rated speed.*

The rotor speed now contains very large ripples, fig. 4.14. Looking at a the rotor speed over a larger period it can be seen that these ripples occur rather periodically, fig. 4.15.

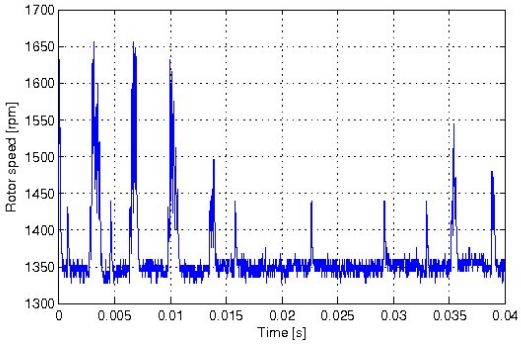

Figure 4.14: *v_{dc} feedback. Rotor speed at full load, rated speed.*

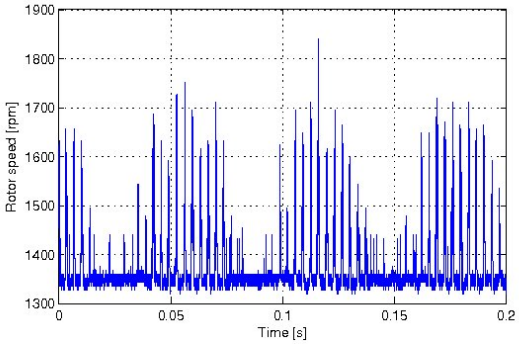

Figure 4.15: *v_{dc} feedback. Rotor speed from a larger time frame at full load, rated speed.*

Case 2: Filtered v_{dc} feedback

As mentioned in Case 1a the DC link voltage contains ripples caused by the switching frequency harmonics. In this case these harmonics are filtered with a 1st order filter with cut-off frequency $f_c = 500\ Hz$ before being used as a scaling factor for the SVM. The discretized form of the filter is:

$$\left(\frac{1}{\frac{s}{2\pi\cdot 500}+1}\right)_{s=\frac{2}{T_s}\frac{z-1}{z+1}} = \frac{3142z+3142}{15142z-8858} \tag{4.7}$$

with $T_s = (6\cdot 10^3)^{-1}\ sec.$

This gives results similar to Case 1 which implies that the ripples in rotor speed are not caused by the switching harmonics in the SVM scaling factor. The ripples are more likely caused by the delay between the scaling factor used in the SVM and the actual DC link voltage.

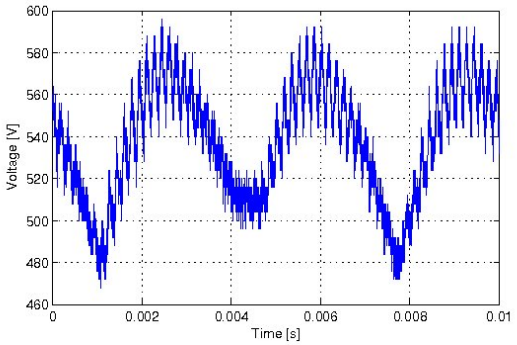

Figure 4.16: *Filtered v_{dc} feedback. DC link voltage at no load, rated speed.*

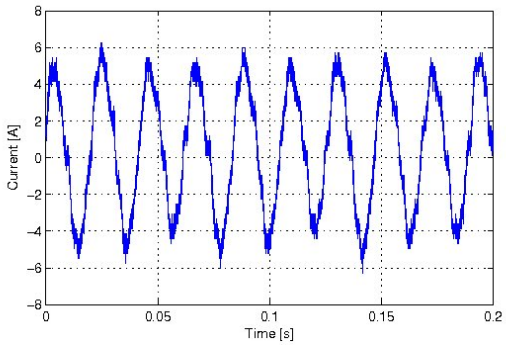

Figure 4.17: *Filtered v_{dc} feedback. Stator current at no load, rated speed.*

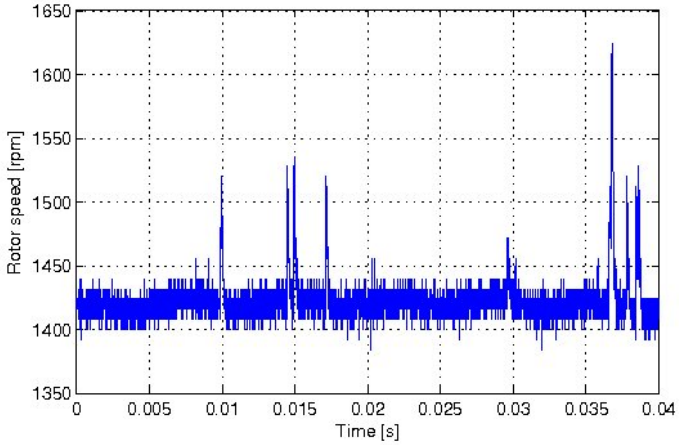

Figure 4.18: *Filtered v_{dc} feedback. Rotor speed at no load, rated speed.*

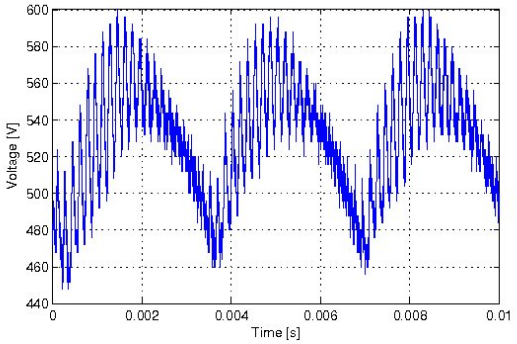

Figure 4.19: *Filtered v_{dc} feedback. DC link voltage at full load, rated speed.*

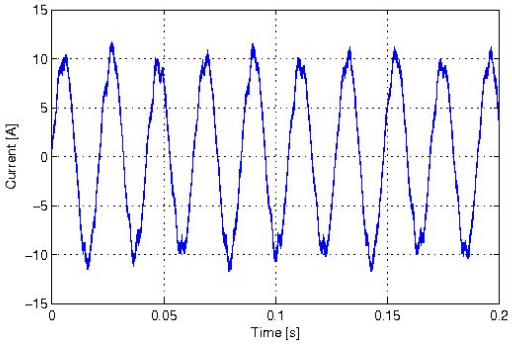

Figure 4.20: *Filtered v_{dc} feedback. Stator current at full load, rated speed.*

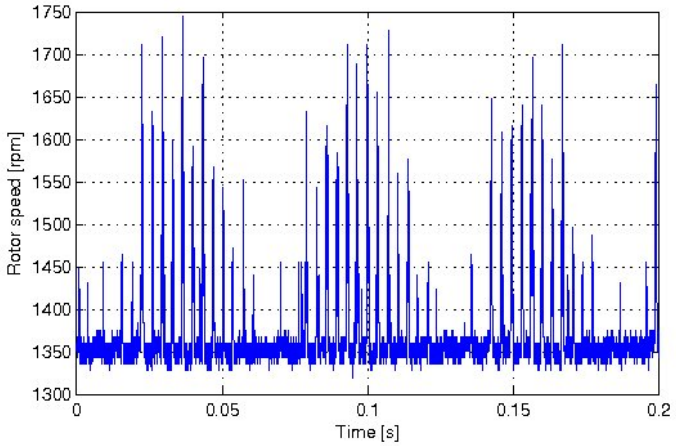

Figure 4.21: *Filtered v_{dc} feedback. Rotor speed at full load, rated speed.*

Case 3: Constant v_{dc} - Full load

The feedback is replaced by a constant which is the calculated average value of the DC link voltage, [5]:

$$v_{dc(AVG)} = 3\sqrt{3}V_{in}/\pi \tag{4.8}$$

where $V_{in} = 380\sqrt{2}/\sqrt{3}$ is the peak of the grid side voltage.

This is actually similar to Case 2 where the constant can be thought of as a filter with even lower passband than in Case 2 which rejects the harmonics caused by the diode rectifier. The results are very similar to Cases 1 and 2.

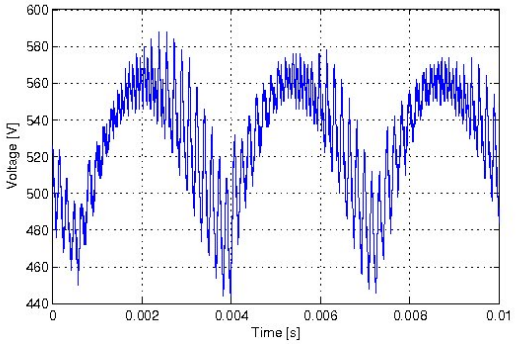

Figure 4.22: *Constant v_{dc}. DC link voltage at full load, rated speed.*

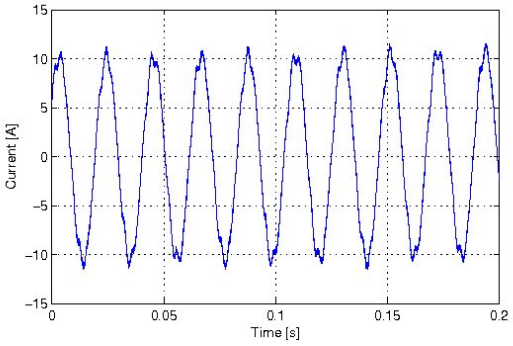

Figure 4.23: *Constant v_{dc}. Stator current at full load, rated speed.*

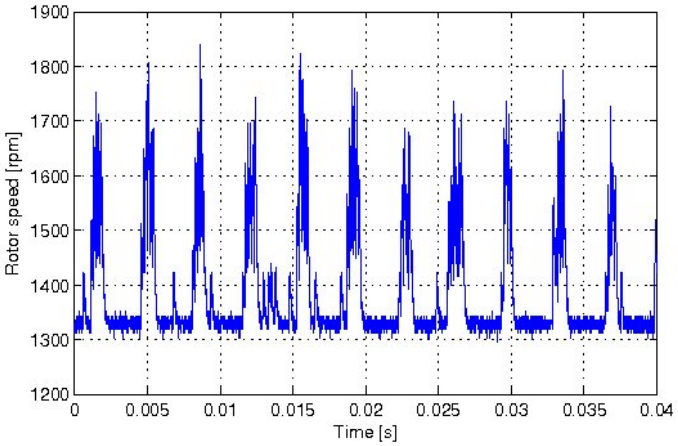

Figure 4.24: *Constant v_{dc}. Rotor speed at full load, rated speed.*

4.3 Summary

This chapter included a description of each component in the test setup and covered important technical details regarding the implementation followed by a section about experimental results.

Experiments were performed for different scaling factors for the SVM to see if that affected the performance of the drive for different load torques. All cases gave similar results. The DC link voltage contained larger harmonics for larger load due to switching of higher currents. The rotor speed had large spikes at full load which was not encountered in simulations. It was also observed that the stator currents suffered from 5th harmonic content which was caused by deadtime.

Chapter 5

Conclusion

This project has analysed stability margin of a frequency converter equipped with a diode rectifer and a small DC link capacitor. This topic is mainly of concern in low cost drives where a diode rectifier and smaller DC link capacitor can decrease the cost of the drive considerably. A DC link capacitor under certain size opens the possibilty for replacing the expensive, bulky and short living electrolytic capacitor for a MPPT capacitor which is cheaper and has longer lifetime and lower losses. But a small DC link capacitor does not provide a suitable filtering of the harmonics caused by the diode rectifier, which results in a highly fluctuating DC link voltage. This introduces large torque ripple and the drive becomes very sensitive for quick changes in speed where this creates large DC link overvoltage and can cause the frequency converter to trip. These types of converters can therefore only be used in low performance drives.

The first step in analysing the system was to build a model of all components of the system for simulations in Matlab/Simulink 7.4.0 (R2007a). Models of every component were explained in chapter 2 except for the diode rectifier and DC link models, which were obtained from supervisor. Many attempts were made to build a satisfying diode rectifier model but as the project time was limited the supervisor provided a model. With the complete model, a sensorless V/f control strategy was simulated. It was found that it gave improved speed accuracy over the open loop V/f control but introduced more ripples. Filters could be added to reduce the ripples which would in turn reduce the dynamic capabilities of the drive. But where the drive is considered as low performance this would not be of concern.

The frequency converter was then linearized in chapter 3 and three transfer functions were obtained. One of these transfer functions was omitted because it was dominated by the SCIM which was not of concern in this project. The linearized model of the frequency converter was then formed by two inputs, the operating frequency of the motor and grid side input voltage, which affected the output, the DC link voltage. This model was found to be always stable for the ideal case where no delay was present in the system. But when a sampling delay was included, unstable conditions were encountered but they were outside the operating range of the SCIM. Increasing the grid side inductance affected the stability margin considerably and the system could be made unstable for all operating conditions. An attempt was made to verify the stability margins of the system by simulation in Matlab/Simulink. Now, PLECS v2.0.2 was used to model the frequency converter and SCIM to speed up simulations and allow the DC link configuration of the Danfoss frequency converter used in implentation to be simulated. The system could not be made unstable by applying a load step outside the operating range which should create an unstable condition according to the stability analysis. This could have been caused by additional damping that is present in the nonlinear model but not included in the linearized model. The torque step could

not be increased much further where the SCIM could not maintain speed for much higher load torques in the simulation. But an unstable condition could be simulated by increasing the grid side inductance. This condition was preditcted by the stability analysis.

Chapter 4 of the report was devoted to implementation and experimental results. Components of the test setup were described and technical details required for the implementation were covered as well. The open loop V/f control and SVM were implemented on a DSP using Real-Time workshop and Target for TI C2000 library in Matlab/Simulink. The SCIM was driven by a modified Danfoss VLT with small DC link capacitor and an extra capacitor bank which worked as a short-term overvoltage protection. A DCM was used as a load machine. Testings were made for different scaling factors for the SVM and experimental results were obtained. The different scaling factors did not have any visible effect on the performance of the system. The sensorless V/f control strategy could not be implemented during the project period due to time constraints.

Chapter 6

Future work

- Further evaluation of the effect of grid side parameters R_g and L_g.
- Evaluation of the effect of the squirrel cage induction motor on stability by including the term that was omitted from the stability analysis.
- Implementation of sensorless V/f control.
- Design of controller to compensate for the voltage fluctuations.

Bibliography

[1] N. Mohan, T. M. Undeland, and W. P. Robbins, *Power electronics, Converters, Applications and Design.* John Wiley and sons, media enhanced 3rd ed., 2003.

[2] R. W. Erickson and D. Maksimovic, *Fundamentals of Power Electronics.* Springer Science+Buisness Media, 2nd ed., 2001.

[3] A. M. Hava, R. J. Kerkman, and T. A. Lipo, "Simple analytical and graphical methods for carrier-based PWM-VSI drives," *IEEE Transactions on power electronics*, vol. 14, January 2005.

[4] V. M. Cárdenas, S. Horta, and R. Echavarría, "Elimination of dead time effects in three phase inverters," *IEEE*, 1996.

[5] M. Hinkkanen and J. Luomi, "Induction motor drives equipped with diode rectifier and small DC-link capacitance," *IEEE Transactions on Industrial Electronics*, January 2008.

[6] H. Sarén, O. Pyrhönen, J. Luukko, O. Laakkonen, and K. Rauma, "Verification of frequency converter with small DC-link capacitor," *EPE 2005 Dresden*, 2005.

[7] K. Kretschmar and H.-P. Nee, "An AC converter with a small DC link capacitor for a 15kW permanent magnet synchronous integral motor," *Power Electronics and Variable Speed Drives, 21-23 September 1998, Conference Publication No. 456, IEEE*, 1998.

[8] H. Sarén, O. Pyrhönen, K. Rauma, and O. Laakonen, "Overmodulation in voltage source inverter with small DC-link capacitor," *IEEE*, 2005.

[9] H. Sarén, K. Rauma, and O. Pyrhönen, "DTC driven single phase fed voltage source inverter with small DC-link capacitor," *IEEE ISIE*, June 2005.

[10] H. Mosskull, "Stabilization of an induction motor drive with resonant input filter," *EPE 2005 Dresden*, 2005.

[11] H. W. Van Der Broeck, H.-C. Skudelny, and G. V. Stanke, "Analysis and realization of a pulsewidth modulator based on space vectors," *IEEE Transactions on Industry Applications*, vol. 24, January/February 1988.

[12] J. Holtz, "Pulsewidth modulation for electronic power conversion," *Proceedings of the IEEE*, vol. 82, August 1994.

[13] G. F. Franklin, J. D. Powell, and A. Emami-Naeini, *Feedback Control of Dynamic Systems.* Pearson Prenitce Hall, 5th ed., 2006.

[14] G. R. Slemon, "Modelling of induction machines for electric drives," *IEEE Transactions on Industry Applications*, vol. 25, November/December 1989.

[15] D. W. Novotny and T. A. Lipo, *Vector Control and Dynamics of AC Drives*. Oxford publications, 1st ed., 1996.

[16] P. C. Krause, O. Wasynczuk, and S. D. Sudhoff, *Analysis of Electric Machinery and Drive Systems*. Wiley-Interscience, 2nd ed., 2002.

[17] C.-C. Wang and C.-H. Fang, "Sensorless scalar-controlled induction motor drives with modified flux observer," *IEEE Transactions on Energy Conversion*, vol. 18, June 2003.

[18] H. Luo, Q. Wang, X. Deng, and S. Wan, "A novel V/f scalar controlled induction motor drives with compensation based on decoupled stator current," *IEEE*, 2006.

[19] J. Hu and B. Wu, "New integration algorithms for estimating motor flux over a wide speed range," *IEEE Transactions on Power Electronics*, vol. 13, September 1998.

[20] A. Munoz-García, T. A. Lipo, and D. W. Novotny, "A new induction motor V/f control method capable of high-performance regulation at low speed," *IEEE Transactions on Industry Applications*, vol. 34, July/August 1998.

[21] M. P. Kazmierkowski, R. Krishnan, and F. Blaabjerg, *Control in Power Electronics*. Academic Press, 1st ed., 2002.

[22] C. L. Phillips and R. D. Harbor, *Feedback Control Systems*. Prentice Hall, 4th ed., 2000.

[23] Z. Ma, T. Zheng, and F. Lin, "Stability improvement of V/Hz controlled PWM inverter-fed induction motors drives," *IEEE*, 2006.

[24] R. Ueda, T. Sonoda, K. Koga, and M. Ichikawa, "Stability analysis in induction motor driven by V/f controlled general-purpose inverter," *IEEE Transactions on Industry Applications*, vol. 28, March/April 1992.

[25] J.-H. Jung, G.-Y. Jeong, and B.-H. Kwon, "Stability improvement of V/f-controlled induction motor drive systems by a dynamic current compensator," *IEEE Transactions on Industrial Electronics*, vol. 51, August 2004.

[26] *TMS320C2000 Digital Signal Controllers Brochure (Rev. B)*, July 2007. Material from Texas Instruments website, http://www.ti.com/litv/pdf/sprb176b.

[27] *TMS320x281x Event Manager (EV) Reference Guide (Rev. E)*, June 2007. Material from Texas Instruments website, http://www.ti.com/litv/pdf/spru065e.

[28] *TMS320x281x Analog-to-Digital Converter (ADC) Reference Guide (Rev. D)*, July 2005. Material from Texas Instruments website, http://www.ti.com/litv/pdf/spru060d.

[29] *TMS320F2810, TMS320F2811, TMS320F2812 ADC Calibration (Rev. A)*, November 2004. Material from Texas Instruments website, http://www.ti.com/litv/pdf/spra989a.

[30] G. F. Franklin, J. D. Powell, and M. Workman, *Digital Control of Dynamic Systems*. Addison Wesley, 3rd ed., 1998.

[31] A. Fitzgerald, C. K. Jr., and S. D. Umans, *Electric Machinery*. McGraw-Hill, 6th ed., 2003.

Appendix A

SVM S-function code

```
double va,vb,vc,v0,va_n,vb_n,vc_n;
double d1,d2,d3;

//Normalize reference voltages
va_n = va_ref[0]/(0.5*V_dc[0]);
vb_n = vb_ref[0]/(0.5*V_dc[0]);
vc_n = vc_ref[0]/(0.5*V_dc[0]);

//Find the absolute values
va=fabs(va_n);
vb=fabs(vb_n);
vc=fabs(vc_n);


//Find the lowest of va,vb,vc
//Zero sequence signal: v0 = 0.5*min(va,vb,vc)
if(va<vb)
{
    if(va<vc)
    {
        v0=0.5*va_n;
    }
    else
    {
        v0=0.5*vc_n;
    }
}
else
{
    if(vb<vc)
    {
        v0=0.5*vb_n;
    }
```

```
    else
    {
        v0=0.5*vc_n;
    }
}

//Duty cycles
d1 = va_n+v0;
d2 = vb_n+v0;
d3 = vc_n+v0;

//Saturation
if(d1>1){d1=1;}
if(d2>1){d2=1;}
if(d3>1){d3=1;}
if(d1<-1){d1=-1;}
if(d2<-1){d2=-1;}
if(d3<-1){d3=-1;}

//Outputs
sw_abc[0] = d1/2+0.5;
sw_abc[1] = d2/2+0.5;
sw_abc[2] = d3/2+0.5;
```

Appendix B

Screenshots from oscilloscope

Following appendix shows screenshots taken from the oscillioscope when experimental data was captured. Conversion ratios to convert voltage unit on the oscilloscopes y-axis to meaningful units are shown in table B.1.

Unit description	Conversion ratio
DC link voltage	$500V^2/V$
Stator current	$2000/150A/V$
Rotor speed	$800rpm/V$

Table B.1: *Acquisition ratios.*

Case 1a: v_{dc} feedback - No load

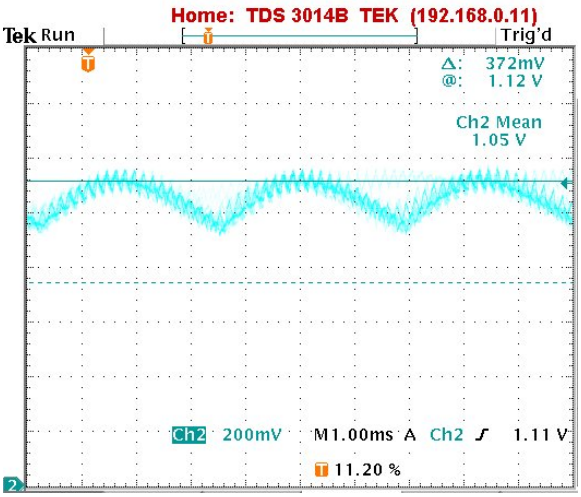

Figure B.1: *v_{dc} feedback. DC link voltage at no load, rated speed.*

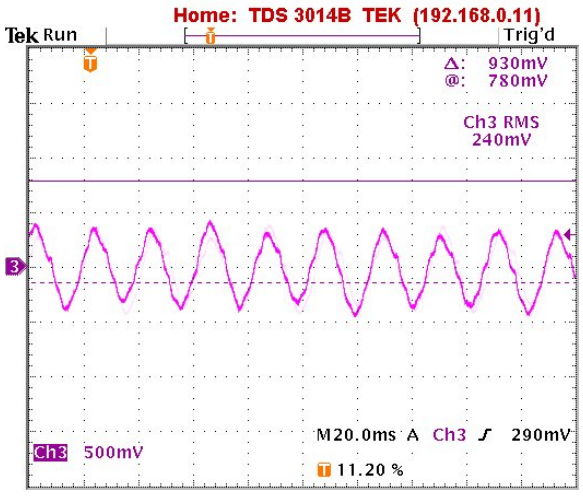

Figure B.2: *v_{dc} feedback. Stator current at no load, rated speed.*

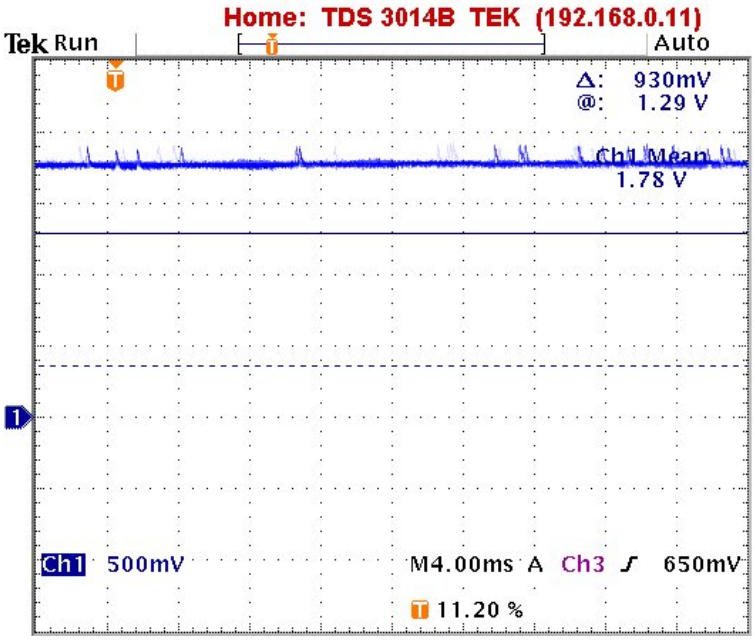

Figure B.3: v_{dc} *feedback. Rotor speed at full load, rated speed.*

Case 1b: v_{dc} feedback - Full load

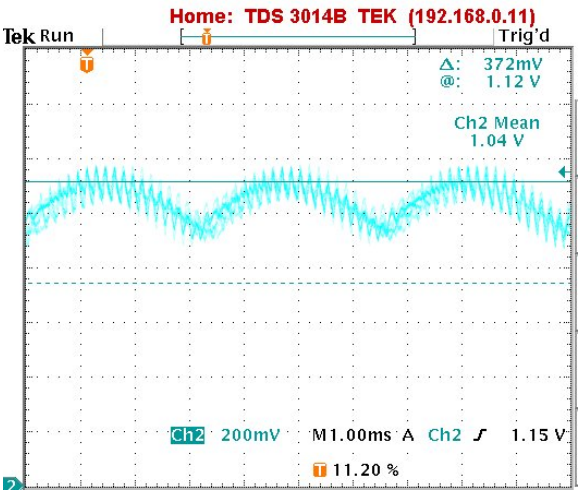

Figure B.4: v_{dc} *feedback. DC link voltage at full load, rated speed.*

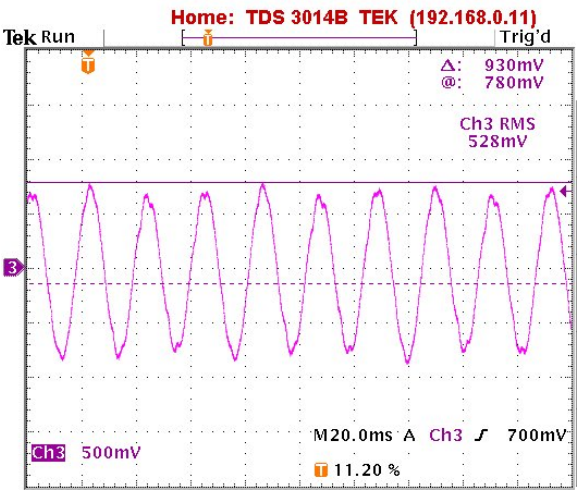

Figure B.5: v_{dc} *feedback. Stator current at full load, rated speed.*

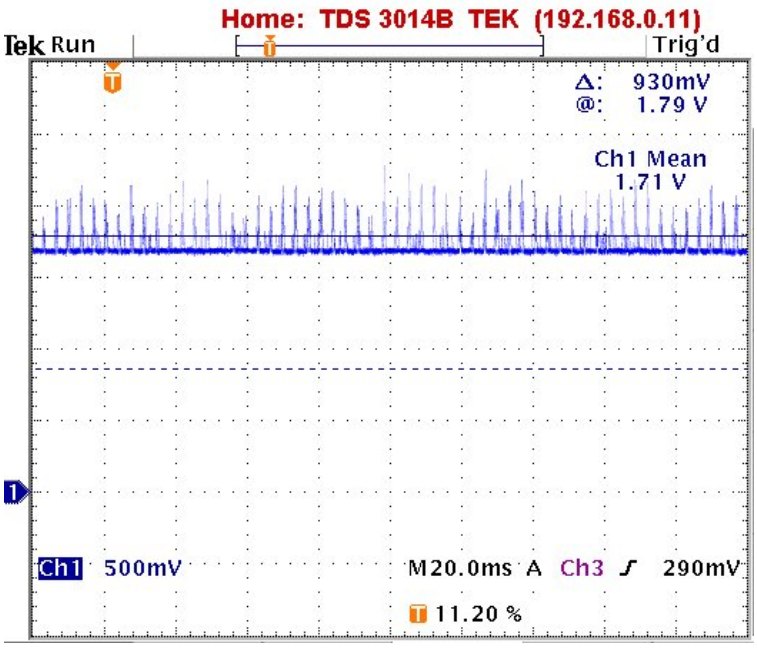

Figure B.6: v_{dc} *feedback. Rotor speed at full load, rated speed.*

Case 2: Filtered v_{dc} feedback

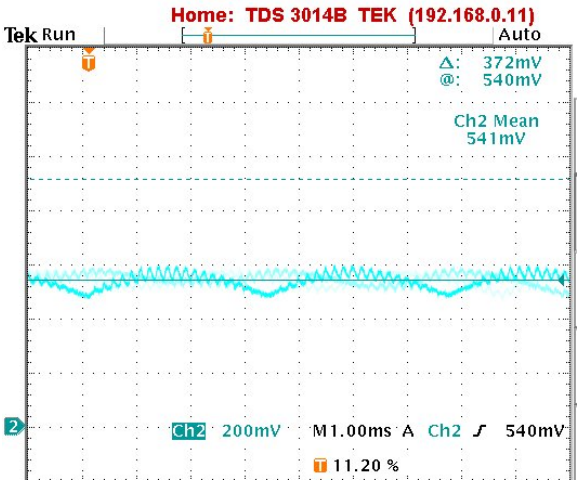

Figure B.7: *Filtered* v_{dc} *feedback. DC link voltage at no load, rated speed.*

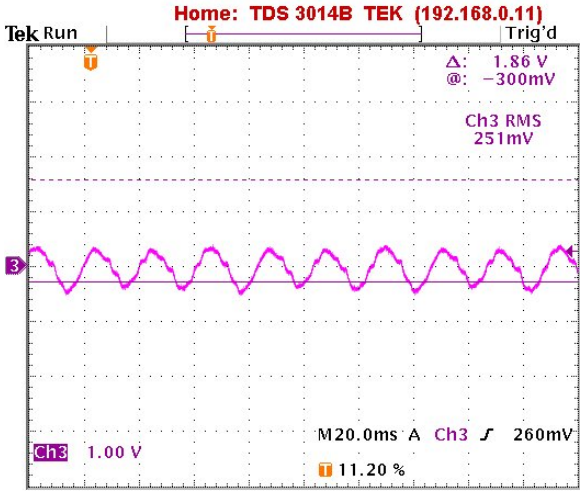

Figure B.8: *Filtered* v_{dc} *feedback. Stator current at no load, rated speed.*

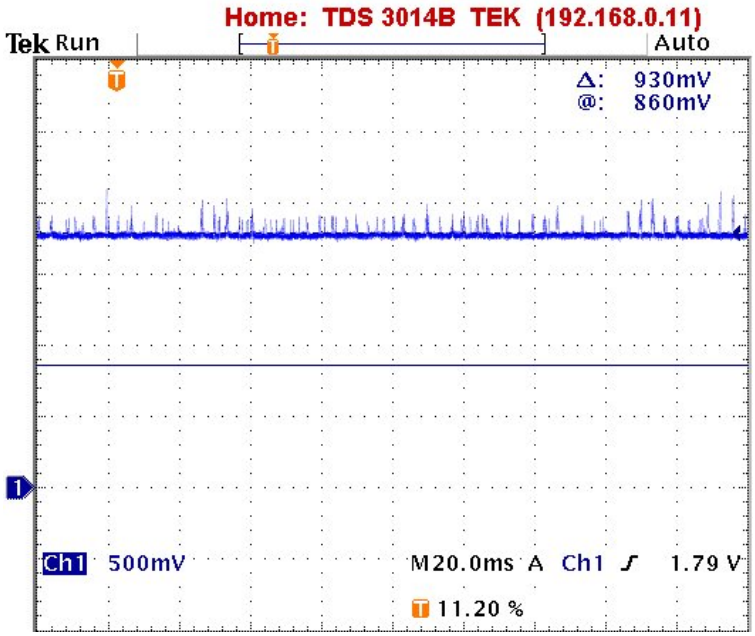

Figure B.9: *Filtered v_{dc} feedback. Rotor speed at no load, rated speed.*

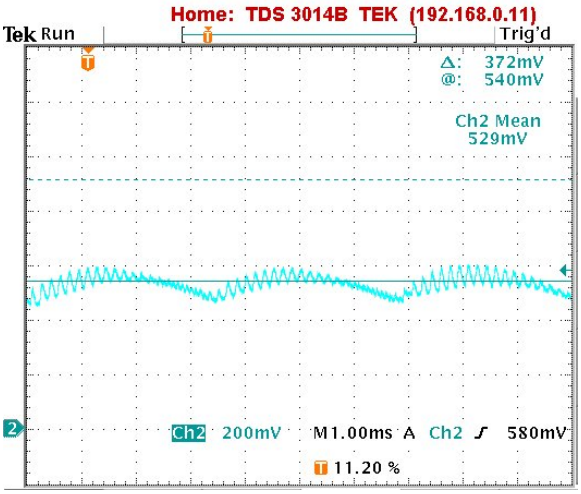

Figure B.10: *Filtered v_{dc} feedback. DC link voltage at full load, rated speed.*

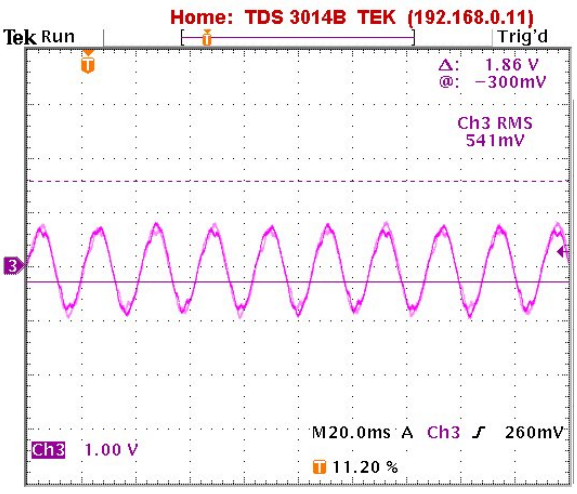

Figure B.11: *Filtered v_{dc} feedback. Stator current at full load, rated speed.*

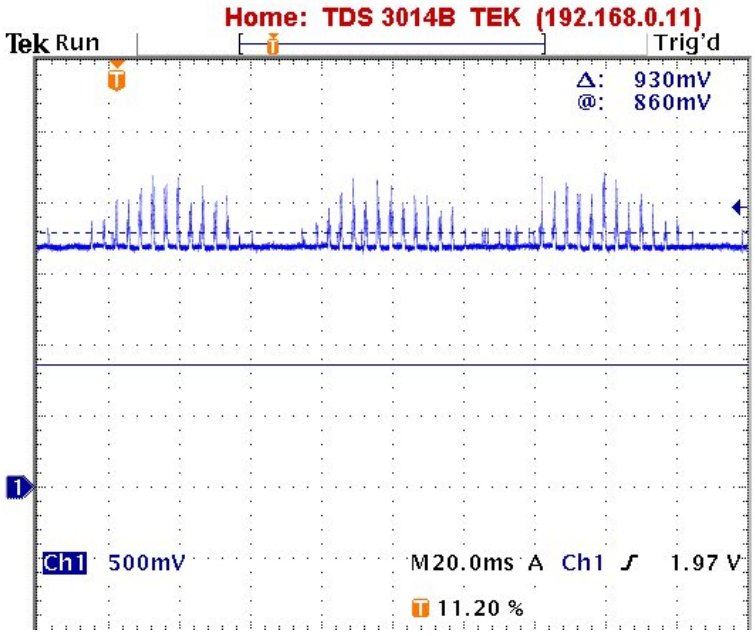

Figure B.12: *Filtered v_{dc} feedback. Rotor speed at full load, rated speed.*

Case 3: Constant v_{dc} - Full load

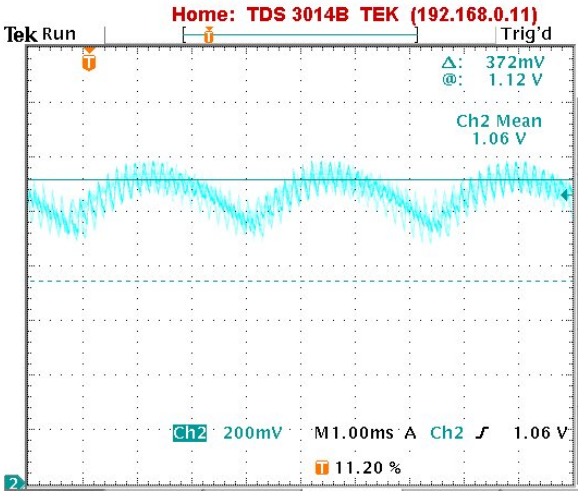

Figure B.13: *Constant v_{dc}. DC link voltage at full load, rated speed.*

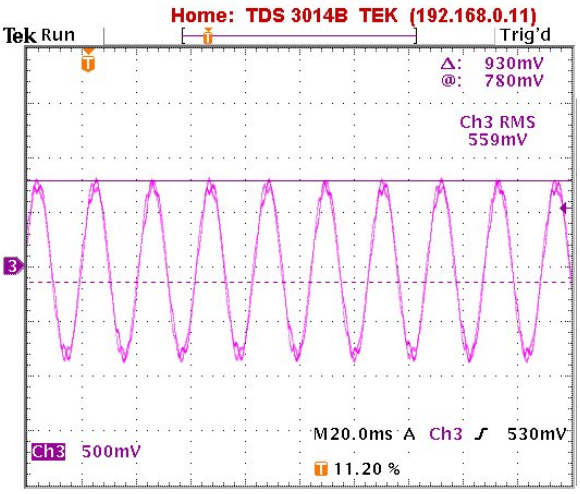

Figure B.14: *Constant v_{dc}. Stator current at full load, rated speed.*

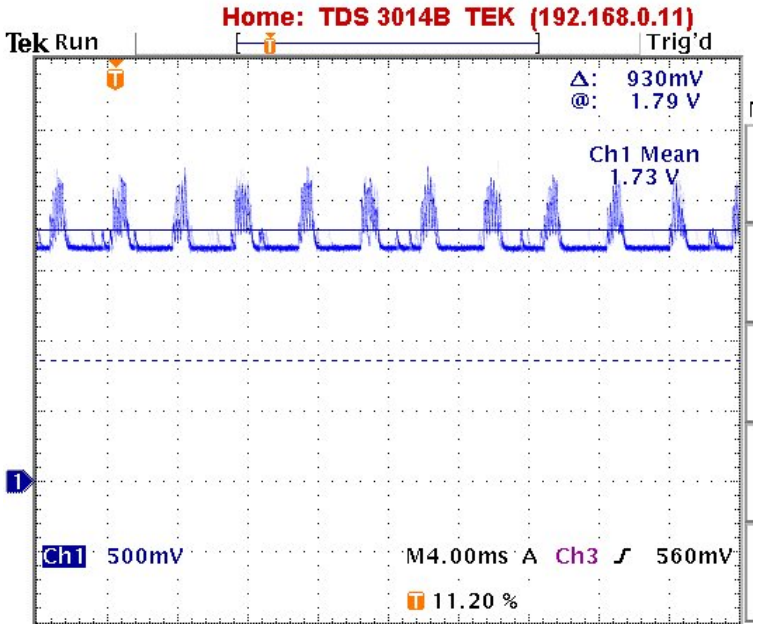

Figure B.15: *Constant v_{dc}. Rotor speed at full load, rated speed.*

Appendix C

Motor nameplates

Tables C.1 and C.2 nameplates of the SCIM and DCM used in the project.

Motor nameplate ABB Motors - MT100LB28-4 MK110023-5		
Nominal power	P_n	3.0 kW
Nominal phase voltage	V_n	$380/\sqrt{3}$ V_{rms}
Maximum phase voltage	$V_{n(max)}$	$420/\sqrt{3}$ V_{rms}
Nominal current	I_n	6.9 A_{rms}
Nominal frequency	f_n	50 Hz
Nominal power factor	PF	0.77
Nominal speed	n_n	1430 rpm
Nominal torque	T_n	20 Nm

Table C.1: *SCIM nameplate.*

Motor nameplate Thrige-Titan A/s - Motor shunt - CLASS F		
LAK132 - No. 2247266-8249		
Nominal power	P_n	3.3 kW
Nominal armature voltage	V_{arm}	400 V
Nominal armature current	I_{arm}	9.7 A
Nominal field voltage	V_f	220 V
Nominal field current	I_f	0.7 A
Nominal speed	n_n	1560 rpm
Nominal torque ($I_f = 0.7$ A, $I_{arm} = 9.7$ A)	T_n	20 Nm

Table C.2: *DCM nameplate.*

Appendix D

Contents of CD-ROM

The enclosed CD-ROM contains the following:

- Root of CD-ROM
  - This folder contains the report in pdf format.
- References
  - This folder contains the papers in the Bibliography.
- Report
  - This folder contains the latex source files of the report and pictures.
- Simulations
  - This folder contains the Simulink models used in simulations.
- Implementation
  - This folder contains the Simulink models used in implementation, documents related to the DSP and pictures of the setup.
- Other stuff
  - This folder contains other stuff that was used during the project period, datasheets, m-files, models etc.